Synthesis and application of oxidised carbon nanotubes in supercapacitors

Author:
Tian, Yuheng

Publication Date:
2016

DOI:
https://doi.org/10.26190/unsworks/2916

License:
https://creativecommons.org/licenses/by-nc-nd/3.0/au/
Link to license to see what you are allowed to do with this resource.

THE UNIVERSITY OF NEW SOUTH WALES

School of Chemical Engineering

SYNTHESIS AND APPLICATION OF OXIDISED CARBON NANOTUBES IN SUPERCAPACITORS

YUHENG TIAN

Supervisors: Dr. Da-Wei Wang and Prof. Rose Amal

7 Jan 2016

PLEASE TYPE

THE UNIVERSITY OF NEW SOUTH WALES
Thesis/Dissertation Sheet

Surname or Family name: **Tian**

First name: **Yuheng**   Other name/s:

Abbreviation for degree as given in the University calendar: **MRes**

School: **Chemical Engineering**   Faculty: **Engineering**

Title:
**Synthesis and Application of Oxidised Carbon nanotubes in
Supercapacitors**

Abstract 350 words maximum: (PLEASE TYPE)

In this thesis, two types of supercapacitors based on the functionalised carbon nanotube (CNT) electrodes that were decorated wi
different amounts of oxygen-containing groups were assembled. The as-purchased CNTs were functionalised by using improve
Hummer's method, which was adjusted to introduce different amounts of oxygen functional groups. These oxygen functional group
changed the surface structures of the CNTs and hence their electrochemical performances, because the oxygen groups are red
active. On the other side, the quantity of the oxygen groups also reduces the electrical conductivity of CNTs, thereby impairing th
electrode performance. Therefore, as the first part of this thesis we studied the correlation of structures with electrochemic
performances of those functionalised CNTs with different oxygen contents.

In the second part, an asymmetric zinc ion capacitor (ZIC) was constructed, which was composed of a zinc anode, a low-level oxidise
CNT cathode and a zinc sulphate-based liquid or gel electrolyte. The low-level oxidised CNTs were characterised by the abunda
surface oxygen-containing groups and the intact graphitic inner tubes that maintained the electrical conductivity. These oxyge
functional groups provided a large pseudo-capacitance, due to the electrochemical adsorption/desorption of Zn^{2+} ions as well a
improved the electrode wettability, giving rise to a higher capacitance than that of the ZIC with an as-purchased CNT cathode.

In the last part of this work, a symmetric solid-state supercapacitor was fabricated, which used the mildly oxidised CNT electrodes an
sulfuric acid/poly(vinyl alcohol) gel electrolyte. The CNTs oxidised in a mild condition showed a hybrid geometrical structure with bot
closed tubes and unzipped tubes. The unzipped tubes enriched with oxygen-containing groups could provide electrochemical activ
sites for improving the capacitance while the closed tubes that preserved mostly the sp2 bonding network could endow the electrod
with a good electrical conductivity. This hybrid structure rendered a good electrochemical performance in the solid-state device.

....   11/01/2016
Signature   Witness   Date

FOR OFFICE USE ONLY   Date of completion of requirements for Award:

THIS SHEET IS TO BE GLUED TO THE INSIDE FRONT COVER OF THE THESIS

ORIGINALITY STATEMENT

'I hereby declare that this submission is my own work and to the best of my knowledge it contains no materials previously published or written by another person, or substantial proportions of material which have been accepted for the award of any other degree or diploma at UNSW or any other educational institution, except where due acknowledgement is made in the thesis. Any contribution made to the research by others, with whom I have worked at UNSW or elsewhere, is explicitly acknowledged in the thesis. I also declare that the intellectual content of this thesis is the product of my own work, except to the extent that assistance from others in the project's design and conception or in style, presentation and linguistic expression is acknowledged.'

Signed ....

Date ....11./..01./..2018.................................

Abstract

In this thesis, two types of supercapacitors based on the functionalised carbon nanotube (CNT) electrodes that were decorated with different amounts of oxygen-containing groups were assembled. The as-purchased CNTs were functionalised by using improved Hummer's method, which was adjusted to introduce different amounts of oxygen functional groups. These oxygen functional groups changed the surface structures of the CNTs and hence their electrochemical performances, because the oxygen groups are redox active. On the other side, the quantity of the oxygen groups also reduces the electrical conductivity of CNTs, thereby impairing the electrode performance. Therefore, as the first part of this thesis we studied the correlation of structures with electrochemical performances of those functionalised CNTs with different oxygen contents.

In the second part, an asymmetric zinc ion capacitor (ZIC) was constructed, which was composed of a zinc anode, a low-level oxidised CNT cathode and a zinc sulphate-based liquid or gel electrolyte. The low-level oxidised CNTs were characterised by the abundant surface oxygen-containing groups and the intact graphitic inner tubes that maintained the electrical conductivity. These oxygen functional groups provided a large pseudo-capacitance, due to the electrochemical adsorption/desorption of Zn^{2+} ions as well as improved the electrode wettability, giving rise to a higher capacitance than that of the ZIC with an as-purchased CNT cathode.

In the last part of this work, a symmetric solid-state supercapacitor was fabricated, which used the mildly oxidised CNT electrodes and sulfuric acid/poly(vinyl alcohol) gel electrolyte. The CNTs oxidised in a mild condition showed a hybrid geometrical structure with both closed tubes and unzipped tubes. The unzipped tubes enriched with oxygen-containing groups could provide electrochemical active sites for improving the capacitance while the closed tubes that preserved mostly the sp^2 bonding network could endow the electrode with a good electrical conductivity. This hybrid structure rendered a good electrochemical performance in the solid-state device.

Acknowledgements

Completing a Master by Research degree is a challenging task and it took two years of my life, but I must admit that it is a worthwhile and unforgettable experience. I could made it this far, not only because of my unremitting endeavor, but also the supports I have received from my family, colleagues and friends in their academic, professional and personal roles.

Firstly, I would like to give my sincere thanks to my supervisors Dr. Da-Wei Wang and Prof. Rose Amal for taking me on over the past two years. Together they have provided comprehensive supervision during the studying so that I could go through it without much hustle. Rose, thank you for all the time you have encouraged me a lot and devoted to my education and development. Da-Wei, thank you for all your time you have spent at guiding my work. Your suggestions on my research has always been explicit and inspiring, and very importantly, you are always approachable. I did enjoy the times when we were having discussions on the research ideas. Also, thank you for reading and revising my manuscripts earnestly and teaching me with patience how to make a good presentation. You gave me the inexpressible guides and help in my research road. Here, I have to thank you once more for being considerate for my future in academia and provide specific assistance for the prospect. I am grateful for all the opportunities and experiences that you and Rose have offered me.

For voluntary advices and experiments, I have to acknowledge the staff in the UNSW Mark Wainwright Analytical Centre for various instrumental analyses. In particular, I appreciate Dr. Anne Rich on the help of Raman and Fourier Transform Infrared spectroscopy, Dr. Yu Wang on the help of X-ray diffraction analysis, Mr. Yin Yao on the help of SEM characterisations, Ms Katie Levick on the help of TEM characterisations, and Dr. Bill Gong on the help of XPS sample measurements and analyses. Furthermore, I would like to thank to an Honour student of UNSW, Huabo Liu, who made a great contribution to our joint project - An Integrated Nanocarbon-Cellulose Membrane for Solid-State Supercapacitors.

To the members in the Particles and Catalysis Research group, it has been a great pleasure to work with all of you. I appreciate the help from our research group manager, Dr. Mandalena Hermawan and the laboratory's help from our analytical support coordinator, Dr. Victor Wong, and the help from the fellow PhD students.

Finally, my family is always the fundamental support throughout my life. They have been an endless source of care and concern throughout these years. My parents have always been my shelter, with all the necessities I may possibly need in any occasion. I can feel the care and love from you, thank you very much.

Yuheng Tian

Sydney, November 2015

List of Publications

- Tian, Y. H.; Amal, R.; Wang, D. W., "A Surface-enabled Aqueous Metal-ion Capacitor with Oxidised Carbon Nanotubes and Metallic Zinc Electrodes", submitted to *Carbon* (under revision), **2015**.

- Liu, H. B.; Tian, Y. H.; Amal, R.; Wang, D. W., "An Integrated Nanocarbon-Cellulose Membrane for Solid-State Supercapacitors", submitted to *Science Bulletin* (invited contribution), **2015**.

Table of Contents

Chapter 1 Introduction

1.1 Background and Aims

Climate change and decreasing reserve of non-regenerative fossil fuels have forced human beings to pay more attention to sustainable and regenerative energies and their conversion and storage.[1] Moreover, the escalating power demand in worldwide nowadays, has placed a lot of emphasis on the development of devices with high power, high energy as well as robustness in withstanding hundreds of thousands of charge/discharge cycles without degrading.[2] Therefore, supercapacitors (SCs), often referred to as ultracapacitors or electrochemical capacitors, are considered as an innovative technology due to its outstanding power performance, excellent reversibility, very long cycle life (>1 000 000 cycles), simple mode of operation, and ease of integration into electronics.[3] Charge storage in SCs is principally based on either the pure electrostatic charge accumulation at the electrode-electrolyte interface as electrical double layer capacitance or the fast and reversible Faradaic processes at the electrode surface as pseudo-capacitance.[4]

Batteries exhibit high energy density as a result of Faradaic reactions in the bulk of active particles. But they have a limited power density, resulting in the slow charge-discharge rate. In contrast, SCs can deliver high power at the cost of low energy storage.[5] Since SCs store electrical charge only at the electrode surface, rather than within the entire electrode, they tend to have lower energy densities compared to batteries.[6] However, since the charge-discharge reaction is not limited by ionic diffusion into the electrode bulk, SCs can be run at high rates and provide high specific power. Thus, a major challenge in the field of electrical energy storage is to bridge the performance gap between batteries and SCs by developing materials that can combine the advantages of both devices.[5] It is urgent to develop advanced materials with ultrahigh specific surface areas and/or large pseudo-capacitances to meet the requirement of high performance SCs.

With respect to electrode materials of the SCs, there are mainly three types: carbon based, metal oxides and polymeric materials.[7] Carbon in various modifications, such as activated carbon, activated carbon fibers, carbon aerogels, carbon nanotubes,

template carbon and carbide derived carbon, *etc.*, are the electrode materials used most frequently for the electrodes of electrochemical capacitors. Reasons for using carbon are low cost, high surface area, availability, and established electrode production technologies. Recently, graphene oxide (GO) has received growing attention in SCs as it can be regarded as a functionalised graphene, bearing oxygen functional groups on its basal planes and edges.[8] GO is a water-soluble material with atomic thickness, which is obtained through strong acid attack of graphite crystals to introduce oxygen-containing groups in the graphite stacks followed by a complete exfoliation of the oxidized solid into nanosheets.[9] GO is the precursor to chemically derived graphene. Regarding its structure, GO is composed of planar, graphene-like aromatic patches of random size separated by sp^3-hybridised carbons which are decorated by hydroxyl, epoxy and carboxyl groups. The unique structural features endow GO with many intriguing chemical properties, such as amphiphilicity, negatively charged surface and multi oxygen-containing groups on its sheets. Therefore, GO can be viewed as a 2D soft material and is a building block of diverse GO-based materials with abundant microstructures. It is demonstrated that surface oxygen-containing functional groups on the GO sheets can considerably enhance the total capacitance of the SCs through introducing pseudo-capacitive faradaic reactions, and improve the wettability of electrodes.[10]

However, due to the oxidation of graphite, resulting in the formation of sp^3 hybridised carbon atoms, GO possesses less $\pi - \pi$ bonding that gives rise to lower electrical conductivity. In order to compensate for the lower conductivity, various carbonaceous materials, e.g. carbon nanotubes (CNTs), have been widely incorporated into the GO as SC electrode materials due to their stable physicochemical properties, excellent conductivity, low cost and long cycle life.[11,12] The combination of GO and carbon materials can not only increase the effective active area of the electrodes for electrochemical reaction but also enhance the wettability of the electrodes in the aqueous electrolytes.

In this project we aim to construct new type supercapacitors based on the functionalised CNT electrodes with different amounts of oxygen-containing groups being introduced. The oxygen groups will be obtained from the oxidation of CNTs using

the improved Hummers method and the various degrees of oxidation will be employed to produce the oxidised CNTs with different structures. Then, the oxidised samples will be used as the electrodes to fabricate a metal ion capacitor and a symmetric all-solid-state supercapacitor. To this end, the aims of this research will be outlined in three aspects:

i.   Study of different oxidised CNTs

Through characterising and comparing the structures and electrochemical performances of the oxidised CNTs with different degrees of oxidation, the most promising samples will be determined and used to construct the supercapacitors.

ii.   Construction of a zinc ion capacitor

Zinc as a safe, cost-effective and eco-friendly metal is widely used in zinc-air and zinc-alkaline batteries. A new type of zinc-ion batteries that are based on the shuttling of Zn^{2+} ions between the zinc anode and MnO_2 cathode was reported recently.[13] Herein a zinc ion capacitor will be constructed by using a CNT-based pseudo-capacitive cathode, a zinc anode and a non-toxic $ZnSO_4$ electrolyte.

iii.   Fabrication of a symmetric all-solid-state capacitor

A flexible all-solid-state supercapacitor will be developed from oxidised CNT-based electrodes with paper-supported H_2SO_4/polyvinyl alcohol gel electrolytes.

1.2 Overview of Thesis

This thesis includes six chapters, which are:

Chapter 1 Introduction: the background and aims of this project are introduced.

Chapter 2 Literature Review: the fundamental structure, properties and synthesis methods of GO are discussed in relation to their promising applications in electrochemical energy storage. Because of the potential of GO in the energy storage, GO will be used as the main material in this project to construct different types of supercapacitors.

Chapter 3 Study of Oxidised CNTs with Different Degrees of Oxidation: this chapter provides the structural information and electrochemical performances of different oxidised CNTs.

Chapter 4 A Metal-ion Capacitor with Oxidised Carbon Nanotubes and Metallic Zinc Electrodes: a zinc ion capacitor using a CNT-based pseudo-capacitive cathode and a zinc anode are reported and the oxidised CNTs can increase the pseudo-capacitance due to the interaction between the oxygen-containing functional groups and the Zn^{2+}, thereby enhancing the capacitance.

Chapter 5 A Symmetric Solid-State Supercapacitors based on Oxidised CNT Electrodes: mildly oxidised CNTs with both tubular (unopened CNTs) and exfoliated (unzipped or scissored) structures are used as the electrodes to construct an all-solid-state capacitor.

Chapter 6 Conclusion and Recommendations

1.3 References

[1]   Simon P, Gogotsi Y. Materials for electrochemical capacitors. Nat Mater 2008;7:845–54.

[2]   Chang S-K, Zainal Z, Tan K-B, Yusof NA, Wan Yusoff WMD, Prabaharan SRS. Recent development in spinel cobaltites for supercapacitor application. Ceram Int 2015;41:1–14.

[3]   Zhang S, Pan N. Supercapacitors Performance Evaluation 2014:1–19.

[4]   Zhang LL, Zhou R, Zhao XS. Graphene-based materials as supercapacitor electrodes. J Mater Chem 2010;20:5983.

[5]   Lee SW, Yabuuchi N, Gallant BM, Chen S, Kim B-S, Hammond PT, et al. High-power lithium batteries from functionalized carbon-nanotube electrodes. Nat Nanotechnol 2010;5:531–7.

[6]   Zhang Y, Feng H, Wu X, Wang L, Zhang A, Xia T, et al. Progress of electrochemical capacitor electrode materials: A review. Int J Hydrogen Energy 2009;34:4889–99.

[7]   Lokhande CD, Dubal DP, Joo OS. Metal oxide thin film based supercapacitors. Curr Appl Phys 2011;11:255–70.

[8]   Dreyer DR, Park S, Bielawski CW, Ruoff RS. The chemistry of graphene oxide. Chem Soc Rev 2010;39:228–40.

[9]   Shao J-J, Lv W, Yang Q-H. Self-Assembly of Graphene Oxide at Interfaces. Adv Mater 2014.

[10]   Xu B, Yue S, Sui Z, Zhang X, Hou S, Cao G, et al. What is the choice for supercapacitors: graphene or graphene oxide? Energy Environ Sci 2011;4:2826–30.

[11]   Guo SR, Wang W, Ozkan CS, Ozkan M. Assembled graphene oxide and single-walled carbon nanotube ink for stable supercapacitors. J Mater Res 2013;28:918–26.

[12]   Lin L-Y, Yeh M-H, Tsai J-T, Huang Y-H, Sun C-L, Ho K-C. A novel core–shell multi-walled carbon nanotube@graphene oxide nanoribbon heterostructure as a potential supercapacitor material. J Mater Chem A 2013;1:11237.

[13]   Xu C, Li B, Du H, Kang F. Energetic zinc ion chemistry: the rechargeable zinc ion battery. Angew Chem Int Ed Engl 2012;51:933–5.

Chapter 2 Literature Review

2.1 Introduction

Graphene oxide (GO), as an oxidised derivative of graphene, is a type of water-soluble material with atomic thickness, which is obtained through strong acid attack of graphite crystals to introduce oxygen-containing groups in the graphite stacks followed by a complete exfoliation of the oxidised solid into nanosheets.[1] The oxygen functional groups have been identified as mostly in the form of hydroxyl and epoxy groups on the basal plane of the GO sheet, with smaller amounts of carboxyl, carbonyl, phenol, lactone, and quinone at the sheet edges.[2,3] The unique structural features endow GO with many intriguing surface chemical properties, such as amphiphilicity, negatively charged nature and multi oxygen-containing groups on its sheets.[1] Therefore, GO can be viewed as a 2D soft material and is a building block of diverse GO-based materials with abundant microstructures.

The study of GO-based materials in recent years has attracted great attention, particularly with respect to electrochemical applications.[3] These are ascribed to the advantages of GO, including its facile synthesis, high dispersibility in a variety of solvents, capability of coupling electroactive species onto the surface, and unique optical properties. Another important issue is consideration of the costs when manufacturing an electrode for use in any real system. In terms of the manufacture of GO-based devices, costs can be reduced compared with the costs for conventional electrodes.

In this literature review, the fundamental structure, properties and synthesis methods of GO are discussed in relation to their promising applications in electrochemical energy storage.

2.2 Structure and Properties of Graphene Oxide

GO is a nonstoichiometric compound with various compositions in accordance to the synthesis conditions as well as it is highly hygroscopic and can decompose slowly above 60-80 °C.[4] Therefore its exact chemical structure still remains ambiguous. But

it is generally acknowledged that, GO, a single sheet of graphite oxide, is a functionalised graphene, carrying many oxygen-containing groups, such as hydroxyl ($-OH$) and epoxy ($-O-$) groups on the basal plane and carboxylic acid groups ($-COOH$) at the edge sites[5–9], as shown in Figure 1a. GO is a strongly oxygenated, highly hydrophilic monolayered material that can readily disperse well in water and in some organic solvents (Figure 1b).[10] The maximum dispersibility of GO in solution depends both on the solvent and the extent of surface functionalisation imparted during oxidation.[2,10] The greater the polarity of the solvent molecules, the greater the dispersability of GO, which is ascribed to polar oxygen-containing functionalities decorated on the GO sheets. The ionisable edge -COOH groups mainly enable GO to be hydrophilic.[11–13] However, its basal plane is essentially a network of hydrophobic polyaromatic islands of unoxidised sp^2-hybridised carbon rings.[14–19] Thus, GO should be amphiphilic, since it consists of a largely hydrophobic basal plane with hydrophilic edges.[8,9,20,21] The pH affects the degree of ionisation of the edge $-COOH$ groups and therefore its amphiphilicity can be tuned by pH.

The unique structural features endow GO with various intriguing surface chemical properties and functionalisation capability.[2,1,22] For example, the hydroxyl groups can be functionalised using carbodiimide coupling chemistry[23,24] or form hydrogen bonds with other hydroxyl-rich molecules[1,25]; The ionisation of the –COOH groups at the edges allows GO to have negatively charged nature[1,26–28] as well as activation and amidation/esterification of these carboxylic groups facilitate the formation of different functionalised GO-based materials for various applications in optoelectronics, bio-devices, drug-delivery vehicles and polymer composites[2]; The chemically reactive epoxy groups on the basal planes are capable of functionalising GO through ring-opening reactions, e.g. using octadecylamine to produce high-quality highly processable surface-functionalised GO nanosheets[29], or through cross-linking reactions, e.g. using polyallylamine to produce chemically cross-linked GO sheets with excellent mechanical stiffness and strength[30]. The sp^2-hybridised carbon atom domains enable GO to exhibit non-covalent interactions with other π-conjugated materials, such as DNA and polymers, *via* π–π stacking, cation-π or van der Waals binding.[2,1,31]
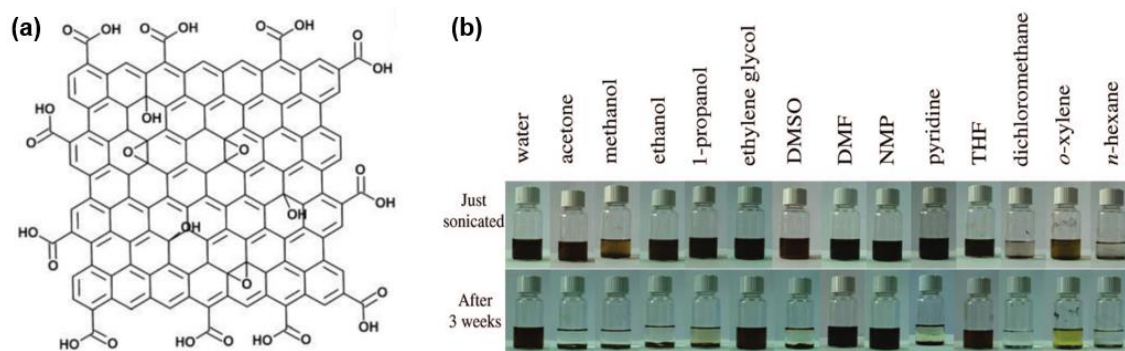
Figure 1. (a) Chemical structural models of GO [9]; (b) Digital pictures of GO dispersions in water and 13 organic solvents through ultrasonication (1 h) [10]

GO is a thermally unstable material, which experiences the removal of epoxide and hydroxyl groups to yield H_2O, H_2, O_2 (oxygen elimination) and also CO_2 and CO (carbon elimination) under a heating treatment, causing the formation of holes on the graphene basal plane.[32–36] Specifically, the loss of H_2O molecules occurs in the GO sheet layers at the temperature of 50-100°C and when the temperature increases to 120-225℃, the thermal decomposition of instable oxygen-containing functional groups can be observed. The combustion of the carbon skeleton finally happens at 620°C.[37–40] The thermal instability enables GO to undergo exothermic disproportionation reactions under mild heating conditions, in which some partially oxidised sp^3 carbon atoms are further oxidised to carbonaceous gases, such as CO_2, and the rest reduced to sp^2 graphene product.[41] The process is called as thermal reduction of GO for the production of chemically modified graphene. Furthermore, the thermal conductivity of GO is affected by the coverage of oxygen functionalities on the sheet layers.[42] As the oxygen coverage increases, the thermal conductivity is significantly reduced. This is because the oxygen defects, causing dramatic structural deformations, significantly enhance the photon scattering.

The electrical conductivity of GO depends on the degree of structural disorder caused by the introduction of oxygen-containing groups.[2,43] Typically, GO is an electrically insulating material due to its disrupted sp^2 bonding networks and its sheet resistance values can reach approximately $10^{12}\,\Omega$ sq^{-1} or higher.[44,45] Interestingly, when GO is controllably oxidised with a low oxidation level, the as-prepared GO with an optical

band gap of 1.7 eV shows a semiconducting behaviour at room temperature in air.[45,46] More significantly, the electrical conductivity of GO can be recovered by restoring the π-network, that is, the removal of oxygen functional groups through various chemical[47,48] and thermal[18,49,50] reduction methods. The decrease in sheet resistance by several orders of magnitude can be achieved *via* the reduction of GO[51] and the reduced GO materials show the conductivity of 2420 ± 200 S m^{-1}[52]. Additionally, the interesting steady state photoluminescence behaviour of GO makes them attractive in novel optoelectronic applications[53] and the optical properties of GO are tuneable through tailoring the oxygen functional groups using controlled infrared irradiation[54].

The mechanical properties of GO is dependent on the water content, thickness and coverage of the functional groups of the samples.[55,56] Water content controls the extent and collective strength of the interlayer hydrogen bond networks of GO platelets, thereby affecting their elastic modulus and tensile strength.[57] The GO sheets with low hydration level are structurally more compact and stiffer than those with higher water content. When the number of layers is decreased, the Young's modulus of the GO sheet increases dramatically.[55,58] The monolayer GO has a mean Young's modulus value of 250 ± 150 GPa, which is however lower than that of graphene (~1.0 TPa). Moreover, the increase of oxygen coverage on the GO sheets causes the decrease of the Young's modulus and intrinsic strength, which is ascribed to the disruption of the sp^2 carbon network and reduction of the energetic stability. [55] A free-standing GO paper synthesised through flow-directed assembly of individual GO sheets exhibits a mean elastic modulus and the highest fracture strength of 32 GPa and 120 MPa, respectively, whose performance is significantly better than bucky paper, vermiculite-based paper and flexible graphite foil.[59] Importantly, the mechanical properties of the GO paper can be improved by introducing divalent metal ions *via* chemical cross-linking[60] and polymer compositing[61,62]. The properties of graphite, graphene and GO are compared in the Table 1. Although graphene possesses excellent mechanical, optical, thermal and electrochemical properties, the cost-effective GO, due to its unique structure and compatibility with various substrates, have also attracted great interest in electrochemical applications such as batteries and supercapacitors, which are discussed in this review.

Table 1. The properties of graphite, graphene and GO.

	Graphite [63,64]	Graphene [63,64]	Graphene oxide (GO)
Hybridisation	sp^2	sp^2	sp^2, sp^3
Crystal system	Hexagonal	Hexagonal	Hexagonal
Dimensions	3	2	2
Density (g cm^{-3})	2.09 – 2.23	>1	1.8 [59]
Hardness	High	Highest (for single layer)	High [55]
Tenacity	Flexible, non-elastic	Flexible, elastic	Flexible, elastic [59]
Optical properties	Uniaxial	97.7% of optical transmittance	steady-state photoluminescence properties [54]
Thermal conductivity (W m-^{1} K^{-1})	Anisotropic: 1500-2000 (a-direction); 5–10 (c-direction)	4840 – 5300	Oxygen coverage-dependent properties, (e.g. 8.8, at a coverage of 20%) [42]
Electronic properties	Electrical conductor	Semimetal, zero-gap semiconductor	Insulator [2]
Electrical conductivity (S cm^{-1})	Anisotropic: 2–3×10^4 (a-direction); 6 (c-direction)	2000	2.06-2.1 × 10^{-4} [52]

2.3 Synthesis and Macroscopic Assembly of Graphene Oxide

2.3.1 Synthesis of Graphene oxide

Graphite oxide, as the precursor for GO, can be synthesised by placing graphite in the concentrated acids in the presence of an oxidizing agent. The formation mechanism of graphite oxide can be divided into three stages: Stage 1, where graphite intercalation compound is formed between the carbon layers due to the addition of concentrated acid; Stage 2, where the formed graphite intercalation compound is oxidised by further adding the strong oxidising agent; Stage 3, where hydrolysis of the formed graphite intercalation compound exists as the resultant material is required to be washed by water.[17] Graphite oxide has a history that dates back to the 1850s when British chemist B. C. Brodie was investigating the atomic weight of graphite *via* the oxidation of flake graphite.[65] He treated graphite repeatedly with potassium chlorate and nitric acid. This method was modified by several investigators including Staudenmaier[66], Hofmann[67], and Hummers and Offeman[68,69], as described in Table 2. The Hummers method outperforms the previous techniques, because its reaction can be completed within a few hours and can avoid the evolution of explosive ClO_2 by using $KMnO_4$ instead of $KClO_3$, improving the reaction safety.[70] However, the Hummers method still has its drawbacks, including the release of toxic gases during the oxidation procedure such as NO_2 and N_2O_4, as well as the environmental risk caused by the residual Na^+ and NO_3^- ions in the waste water.[71] Therefore, Tour and co-workers improved the Hummers method by excluding $NaNO_3$, increasing the amount of $KMnO_4$, and performing the reaction in a 9:1 (by volume) mixture of H_2SO_4/H_3PO_4.[71,72] The resultant graphite oxide produced by this improved Hummers method is comparable to that prepared by the conventional Hummers method. Also, in terms of post-treatment of the waste water, the Mn^{2+} ions can be easily removed by converting them into a precipitate through the pH adjustment.[71] In addition, an electrochemical oxidation and intercalation of graphite has been reported by using twin graphite electrodes in an ionic liquid electrolyte, which is based on a complex interplay of anodic oxidation of water and anionic intercalation from the ionic liquid.[73]

Table 2. Summary of synthesis methods to prepare graphite oxide

Method	Oxidant	Reaction media	Carbon-to-oxygen ratio

Brodie	$KClO_3$	fuming HNO_3	2.19
Staudenmaier	$KClO_3$	fuming HNO_3 + Conc. H_2SO_4	2.52
Hofmann	$KClO_3$	Non-fuming Conc. HNO_3 + Conc. H_2SO_4	1.77
Hummers and Offeman	$NaNO_3$ + $KMnO_4$	Conc. H_2SO_4	1.12
Tour	$KMnO_4$	H_2SO_4 + H_3PO_4	0.74

Graphite oxide possesses a stacked structure analogous to graphite, but the basal planes of its graphene sheets are interspersed mostly with epoxide and hydroxyl groups and its edges are largely decorated with carbonyl and carboxyl functional groups.[13,52] These functional groups render graphite oxide hydrophilic and weaken the van der Waals interactions between the layers, thus facilitating their hydration and delamination to generate mono- or few-layered GO in aqueous media. A mild ultrasonic treatment of graphite oxide in water is the most common to form a stable GO dispersion that consists almost entirely of 1-nm-thick sheets.[74] Some polar organic solvents, e.g., N-methylpyrrolidone (NMP), N,N-dimethylformamide (DMF),etc., can also provide the appropriate environment to exfoliate graphite oxide to the GO sheets through a ultrasonic treatment.[10,11,21,50,75,76] Furthermore, GO can be formed by a thermal treatment. Rapid heating facilitates the expansion and exfoliation of graphite oxide, which are due to rapid evaporation of the intercalated water and evolution of gases generated by thermal pyrolysis of the oxygen functionalities.[18] However, the thermal method accompanies the disadvantages including the consumption of oxygen-containing groups, the increased C/O ratio, and vacancies and wrinkling occurring on the GO sheets.

The overall scheme for synthesis of GO is illustrated in Figure 2a. It is worth noting that the average size of GO sheets can be controlled by the reaction time of oxidation and the amount of the oxidants.[77] A longer oxidation and exfoliation process introduces more topographic defects and oxygen functionalities, thus reducing the size of GO

sheets. More significantly, the improved Hummers method has been developed for the oxidation of carbon nanotubes (CNTs).[78] It is proposed that depending on the quantity of oxidants used in the system, a nanotube is unzipped from the central part and then is longitudinally scissored to form a nanoribbon (Figure 2b). As the oxidation process introduces carboxyl and hydroxyl functional groups, the as-prepared carbon nanoribbons show high solubility in water, ethanol and other polar organic media. [78]
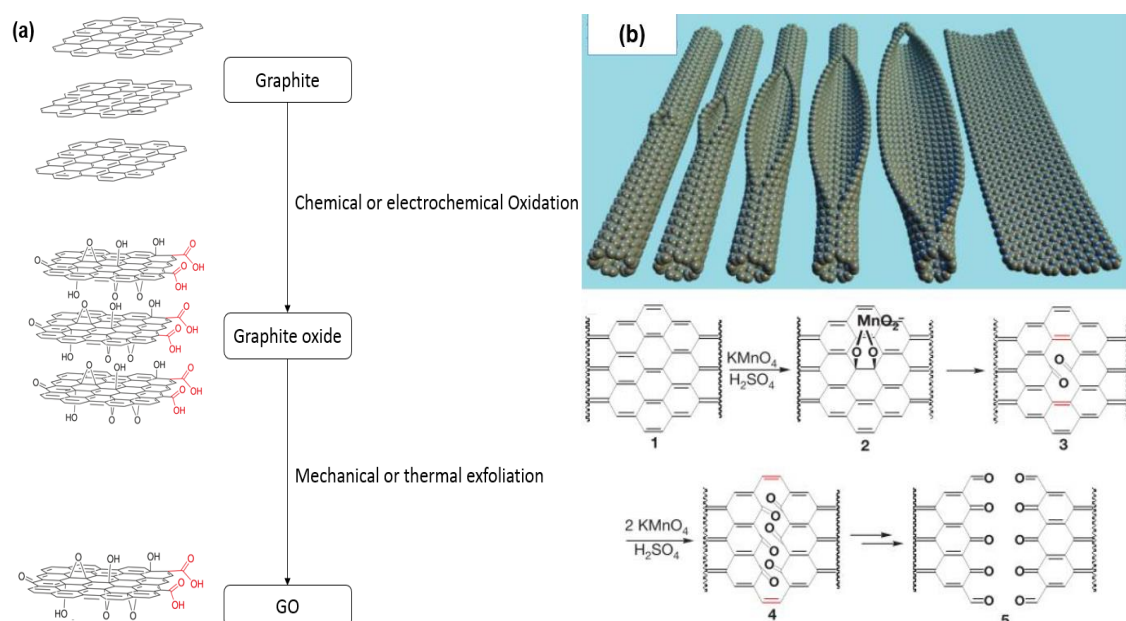
Figure 2. (a) Process scheme for synthesising GO.[79] (b) Longitudinal opening of a carbon nanotube to form a nanoribbon.[78]

2.3.2 Macroscopic Assembly of Graphene Oxide

There are several conventional techniques for preparing GO-based thin films. For example, spin coating, which utilises the centrifuge force generated by rotating a flat substrate, can allow the coating samples to spread on the substrate to form a thin film.[80] Dip coating is a continuous process in which a flat substrate or a cylinder is firstly immersed in a liquid or slurry of the coating samples, and subsequently the substrate is pulled up vertically at a stable speed to allow the coating samples to deposit on the substrate surface, and finally a thin film is formed *via* the gravitational draining and solvent evaporation.[81] Drop casting is a simple and cost-effective method to prepare a thin film, which is achieved by dropping a well-dispersed material on a substrate and then drying it through controlling the pressure and/or

temperature.[82] Spraying coating can also be used for preparation of a thin film through applying an aerosolised material that is generated by a nebuliser on a substrate.[83] However, in these techniques, the uncontrolled capillary flow and de-wetting during solvent evaporation can result in multilayer aggregation and crumpled sheet formation, which make GO films heavily wrinkled and folded.[1,20]

As GO is a negatively charged material, a Layer-by-Layer (LBL) Assembly, which exploits an electrostatic interaction between the oppositely charged materials, can generally be applied for the fabrication of a GO-based hybrid thin film.[1] Interestingly, a diffusion driven LBL assembly process was reported recently for the construction of GO sheets into a three-dimensional (3D) structure.[84] This method (see Figure 3a) is based on the complexation between GO and branched polyethyleneimine (b-PEI) occurring at the interface due to electrostatic interactions. Then the diffusion of b-PEI through the GO/b-PEI complex allows continuous formation of the GO shells into the layered and porous 3D architectures with thickness reaching millimetre ranges, as shown in Figure 3b, c. Furthermore, the abundant surface oxygen functional groups and the amphiphilic nature of GO enable it to self-aggregate at liquid-solid, liquid-liquid and liquid-air interfaces, which are discussed respectively below. The interfacial self-assembly of GO is intrinsically a self-concentrating of GO sheets at interfaces with the assistance of non-covalent interlayer interactions to form well-controlled macrostructures.[1]
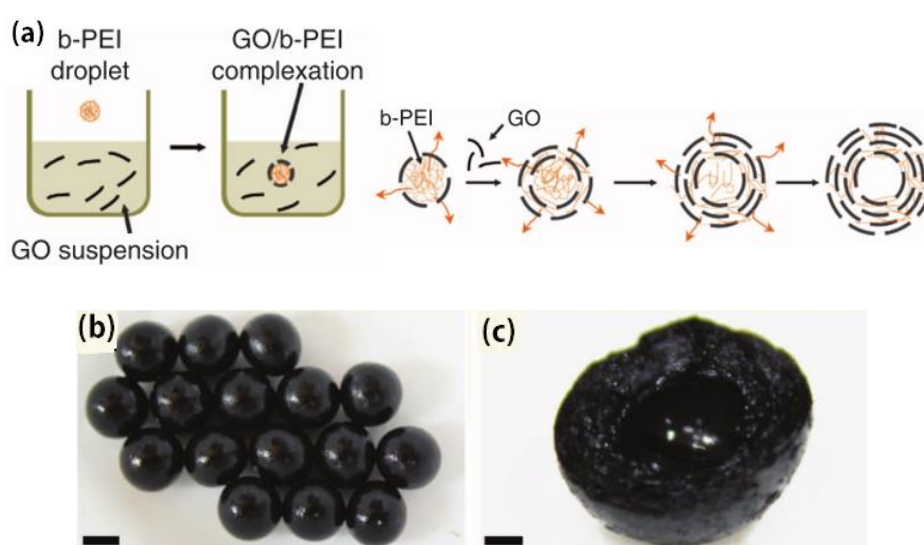
Figure 3. (a) Illustration showing the diffusion driven LBL assembly of GO; (b) The as-prepared GO/b-PEI beads with a 5 mm scale bar; (c) Cross-section of a bead with a 1 mm scale bar .[84]

2.3.2.1 Enrichment of GO at liquid-solid interfaces

A flow-directed assembly is a representative technique to yield a free-standing GO paper at a liquid-solid interface. GO sheets are assembled into a paper-like material *via* the vacuum filtration of the GO colloidal dispersions and the acquired GO paper with thicknesses ranging from 1 to 30 µm shows well-packed layers through almost the entire cross-section.[59] Three mechanisms comprising highly ordered layering, semi-ordered accumulation and disordered concentration were proposed for this vacuum-assisted self-assembly of the GO dispersion (Figure 4a).[85] A series of experiments identify the semi-ordered accumulation as the dominant mechanism during paper fabrication, wherein the loosely assembled, semi-ordered GO nanoplatelets are compressed into a homogeneous thin film with a layer-to-layer structure through the removal of solvent.

Additionally, a GO hydrogel can be formed at the liquid-solid interface through a chemical interaction between an aqueous GO dispersion and a porous anodic aluminium oxide (AAO) film.[86] Figure 4b gives an illustration of this self-assembly process, and the interaction between hydroxyl groups of AAO and carboxyl groups attached on GO sheets is believed to facilitate the fast enrichment of GO sheets at the interface, which thus results in the generation of a concentrated GO hydrogel at the porous surface of the AAO film. An electrophoresis process is also reported for the formation of a GO hydrogel, during which the negatively charged GO sheets move towards the positively charged anode and accumulate there (see Figure 4c).[1,87] Freeze casting occurring at frozen solvent crystals-water interface is another widely used method to prepare porous GO-based materials.[1,88] During this process, a phase separation, that is achieved by freezing a liquid suspension containing nanoparticles, results in the rejection of solid nanoparticles from the formed ice crystals, and subsequently these nanoparticles are accumulated between the growing ice crystals. A porous structure can be obtained by the final sublimation process with the removal of the frozen ice crystals.
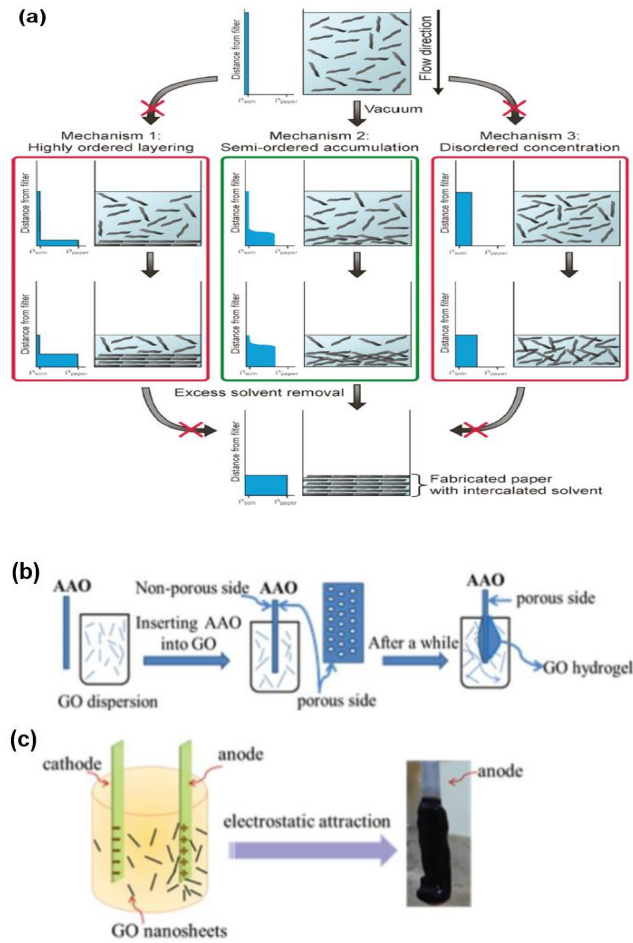
Figure 4. (a) A scheme presenting the three proposed mechanisms for the formation of GO film[85]; (b) Formation process of a GO hydrogel formed on the porous AAO surface[86]; (c) Illustration of electrophoresis accumulation process of a GO hydrogel formed on the anode surface[1].

2.3.2.2 Enrichment of GO at liquid-liquid interfaces

Self-assembly of the particles at the liquid–liquid interface is thermodynamically favourable, as the interfacial energy of the system is reduced, caused by the creation of a new interface between the particle and liquid phases instead of the liquid-liquid interface.[89] In virtue of the GO's amphiphilicity, a volatile organic solvent such as toluene and chloroform can be used to collect GO from its aqueous dispersion.[20] Specifically, chloroform/toluene on the GO dispersion form a thin oil layer, which then attracts GO sheets to the vicinity of the oil-water interface with the evaporation of the organic solvent, as shown in Figure 5a. However, organic solvent evaporation provides little driving force, resulting in slow GO migration in aqueous phase. Thus, a quick

formation method of GO-based thin films was reported using an ethanol-assisted self-assembly at pentane-water interface (Figure 5b).[90] Ethanol, on one hand, serving as a non-solvent can compromise the stability of GO and provide driving force for GO transfer. On the other hand, both the evaporation of pentane and the mixing between ethanol and water provide sufficient driving forces for the aggregation of GO sheets at the pentane-water interface.

A facile assembly method utilising a water-in-oil emulsion technique without surfactant was proposed for producing hollow GO spheres.[91] Figure 5c shows an illustration of this method. GO sheets were dispersed into aqueous ammonia and then the dispersion was mixed with hot olive oil by mechanical agitation. The hollow GO spheres were finally collected by removing water and oil. The aqueous ammonia plays an important role on the formation of the soft template and the self-assembly of GO sheets around the template. When aqueous ammonia containing GO was mixed with olive oil, a water-in-oil system was formed. GO sheets were supported by the water-in-oil interface, and self-aggregated around water droplets under the assistance of ammonia. Moreover, the Breath Figure (BF) technique is a bottom-up self-assembly method occurring at a volatile solvent-water interface to prepare honeycomb structures. For example, a macroporous film of polymer-grafted GO can be achieved by dispersing the polymer-grafted GO platelets in an organic solvent and then casting the dispersion onto a suitable substrate under the exposure of humid air (see Figure 5d).[92] The concentration of precursor solution and the chain length of grafted polymers at the GO sheet surface determine the pore size and the number of pore layers.
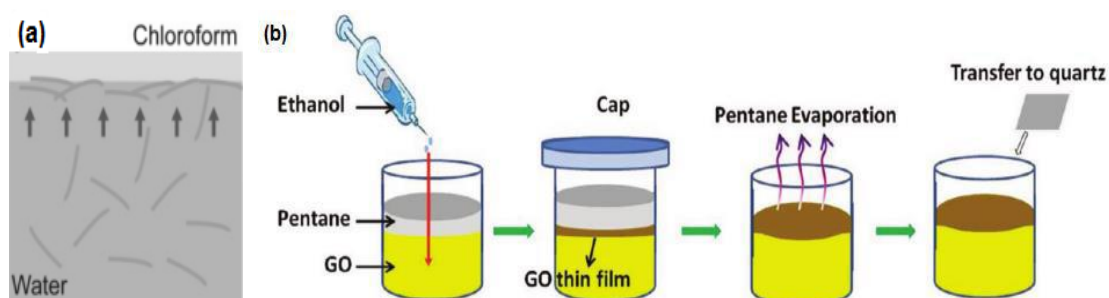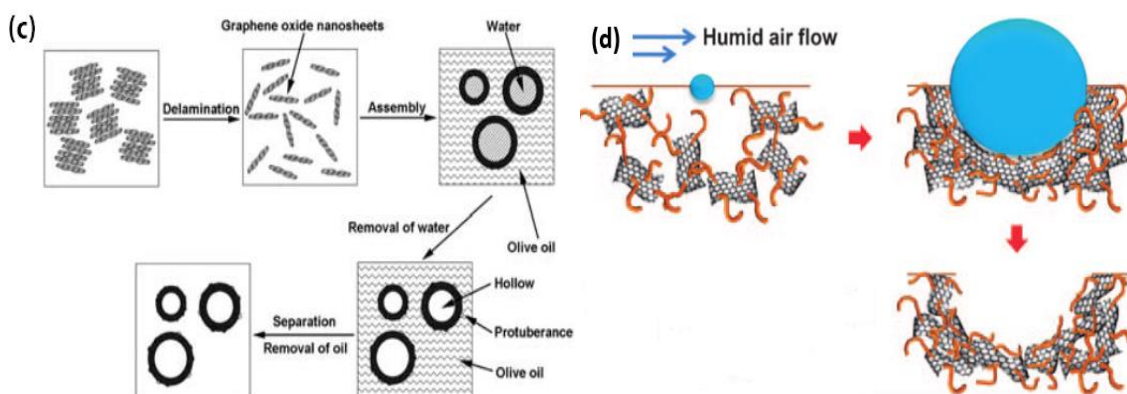
Figure 5. (a) Enrichment of GO at the oil-water interface[20]; (b) Schematic illustration of GO thin film synthesis using an ethanol-assisted self-assembly[90]; (c) Illustration of hollow GO sphere preparation[91]; (d) Procedure for the BF self-assembly of the macroporous film[92].

2.3.2.3 Enrichment of GO at liquid-air interfaces

A liquid-air interface is considered as a favourable platform for the self-assembly of GO sheets, as such interface can be readily constructed by the ambient atmosphere as a gas phase and the GO dispersion as a liquid phase. For instance, an evaporation-induced assembly can form macroscopic GO membranes at the liquid-air interface by evaporating the GO hydrosol, as illustrated in Figure 6a.[93] This method utilises the kinetic energy from the heat treatment to facilitate the GO transfer and promote the membrane formation at such interface. Interestingly, the evaporation-induced method can be applied to hybridise bi- and multi-components in a thin GO-based membrane. Figure 6b presents the formation process of the CNT-GO membrane using the heating-driven liquid-air interfacial self-assembly.[94] GO, in this case, serves as a surfactant to disperse CNTs to form a homogeneous suspension containing CNT-attached GO layers. Furthermore, efficiency of the evaporation-induced assembly can be enhanced by a flotation process using gas bubbles (e.g. nitrogen, air, CO_2, etc.). When gas bubbles are blown through a GO suspension, the rising bubbles are capable of capturing the GO sheets and transporting them to the suspension surface, thereby accelerating the formation of the GO membrane at the liquid-air interface (Figure 6c).[8,20]

The free-standing GO hydrosol droplets can provide spherical 3D liquid-air interfaces and therefore, the evaporation-induced assembly occurring around these GO droplets can generate near-spherical 3D crumpled particles.[1] For example, as presented in Figure 6d, GO aerosol droplets produced by an ultrasonic atomizer are carried by nitrogen gas to fly through a horizontal tube furnace preheated at a desired temperature and then the crumpled particles are formed from the rapid evaporation process and collected at the exhaust.[95] The acquired crumpled particles can pack tightly without apparent reduction in the area of accessible surface, as well as exhibit excellent solution processability, superior compressive strength, and large surface area.

Importantly, Langmuir-Blodgett (LB) assembly is a classic liquid-air interfacial self-assembly technique to prepare ultrathin GO film, especially for single-layer GO film [1,20,96], and also to synthesise hybrid GO-based films[97]. In a typical LB process, amphiphilic GO sheets are first dissolved in a volatile organic solvent, which is dropped onto water, and then a mono- or few-layered GO film is formed at the water-air interface after the evaporation of the volatile solvent. It is note-worthy that the LB assembly can produce the GO film without multilayer aggregation, and wrinkle and fold formation. This is ascribed to the strong edge-to-edge electrostatic repulsion between adjacent GO sheets.
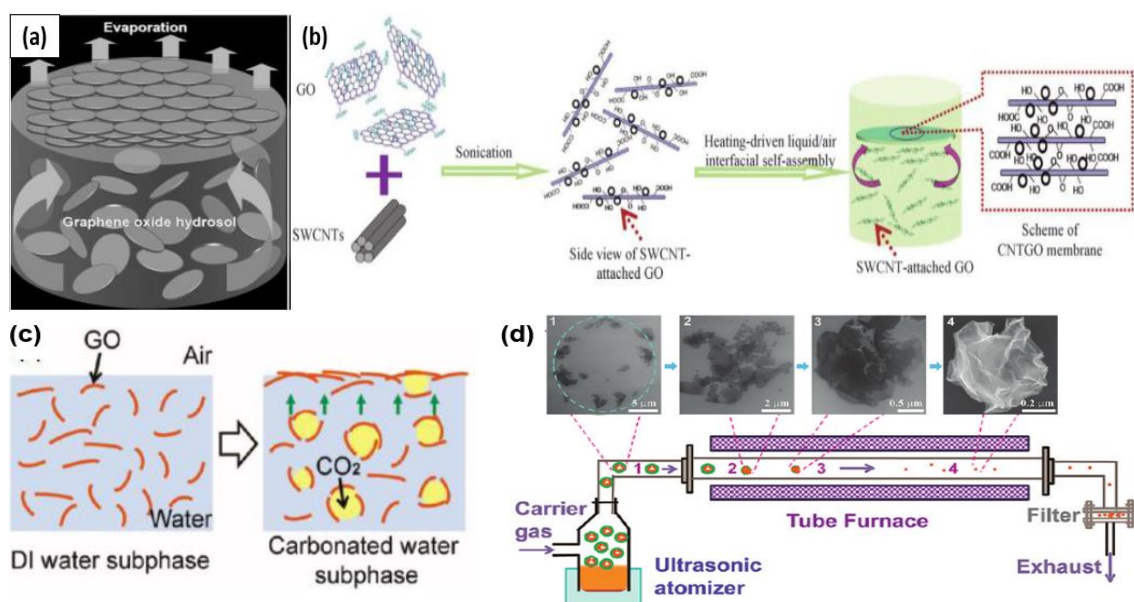

Figure 6. (a) Schematic representation of a liquid-air interfacial self-assembly process of the GO membrane[93]; (b) Scheme of the self-assembly of a CNT/GO hybrid

membrane[94]; (c) Illustration for the flotation of GO in carbonated water[8]; (d) Schematic showing the evaporation-induced crumpling process[95].

2.4. Application of Graphene Oxide in Electrochemical Energy Storage

2.4.1 Batteries

2.4.1.1 Lithium metal/ion batteries

Rechargeable lithium batteries should be the most impressive success story of modern electrochemistry in the last two decades, which power today's portable, entertainment, computing and telecommunication equipment. Normally, the Li batteries possess a gravimetric energy of ~150 W h kg^{-1}_{cell}.[98] The first generation of Li batteries, termed Li metal batteries, used Li metal as anode, which included Li–TiS_2, Li–MoS_2 and Li–Li_XMnO_2 systems.[99,100] However, they encountered safety problems, as uneven Li dendrite growth led to explosion hazards. Nevertheless, Li metal presents the highest theoretical capacity of 3680 mA h g^{-1} and it can match with many high capacity cathodes, therefore the investigation of Li metal anode has never stopped.[101] Substituting metallic Li for an alloy with Al solved the dendrite problem, but the alloy electrodes exhibited a limited cycling performance due to extreme changes in volume during operation.[101] In the meanwhile, significant advances had occurred with lithium ion batteries (LIB) that utilised carbon anode and lithiated transition metal oxide cathode. In this LIB system, Li ions are extracted from the cathode host during charging, move through the electrolyte, and intercalate into the anode host.[102] Such process is reversed when the battery is discharging. However, the LIBs deliver a very low power density (100–1000 W kg^{-1}_{cell}), owing to the particularly low solid-state diffusion rates. Graphite–$LiCoO_2$ is a representative LIB system (**Error! Reference source not found.**a) according to the following reactions:

$C_6 + Li^+ + e^- \leftrightarrow LiC_6$;

$LiCoO_2 \leftrightarrow 0.5 Li^+ + 0.5e^- + Li_{0.5}CoO_2$.
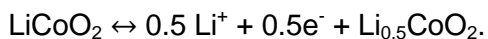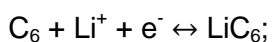
The formation of LiC_6 has a maximum theoretical capacity of 372 mA h g^{-1} and $LiCoO_2$ presents an average capacity of 140 mA h g^{-1}.[103] The capacity for various anode and cathode materials used in Li-based cells is outlined in **Error! Reference source not found.**b.
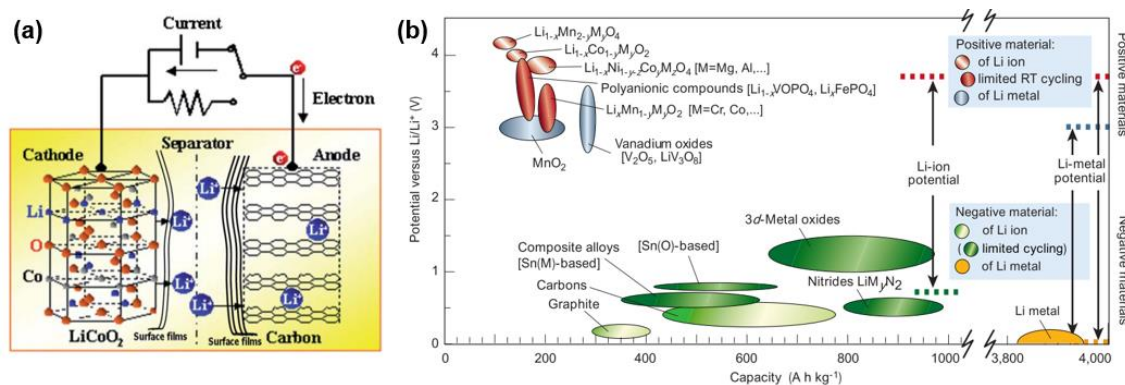
Figure 7. (a) A schematic presentation of a Li-ion battery based on graphite anode and LiCoO$_2$ cathode[100]; (b) Voltage versus capacity for anode and cathode materials used in rechargeable Li batteries[99].

In terms of the improvement of electrochemical performance, nanostructure provides a large surface area and a short diffusion distance. Nano-sized cathode materials have been successfully obtained through a GO assisted facile hydrothermal synthesis method. GO significantly affects the morphology and particle size of the materials. LiMnPO$_4$ nanoparticles were synthesised according to the illustration in Figure 8a, during which Mn^{2+} ions bonded by the oxygen functional groups on GO sheets *via* coordination interactions and the LiMnPO$_4$ was finally formed by a solvothermal process.[104] Adding GO additive in a solvothermal system is effective to reduce size of LiMnPO$_4$ and the particle size decreases with the increased content of GO. The nano-LiMnPO$_4$ with a particle size of 30-70 nm displayed a specific capacity of 140 mA h g^{-1} at 8.5 mA g^{-1} in the LIB and 72.3% of its initial capacity after 100 cycles. Similarly, assisted by GO, LiMn$_{0.6}$Fe$_{0.4}$PO$_4$ nanoparticles with an average diameter of ~80 nm were prepared by a hydrothermal route as cathode material for LIB, which showed an initial discharge capacity of 140.3 mA h g^{-1} at a 0.05 C rate.[106] The V$_3$O$_7$·H$_2$O nanobelts were also self-assembled by a hydrothermal method with GO assistance and they, used as the cathode in the Li metal battery, exhibited a high initial discharge capacity of 352 mA h g^{-1} at the current density of 100 mA g^{-1}.[107] Especially noteworthy is that although the GO, in this case, plays a role on restricting the particle size of the materials, the reduction of GO happen in the subsequent solvo-/hydrothermal process.

21

Furthermore, GO can play an indirect function on the cathode performance of lithium batteries. GO-coated vanadium oxide nanomaterials, prepared from a $VOSO_4$ sol using a hydrothermal method, was reported to use as the cathode for Li metal batteries.[108] The GO-coated cathode exhibited a discharge capacity of 185 mA h g^{-1} at 100 mA g^{-1}, which was higher than that of the carbon-coated vanadium oxide electrode (135 mA h g^{-1}), probably due to the larger surface area of GO. Also, the GO-coated cathode retained 86.5% discharge capacity after 20 cycles, outperforming the pure vanadium oxide cathode. The aggregation of active materials occurs in the vanadium oxide nanostructures during the charge-discharge process, resulting in the capacity loss. However, the GO suppresses the agglomeration and deformation of the $VO_2(B)$ nanostructures and accommodate the large volume variation and maintain good electronic contact during the cycling process and improve the rate performance. The porous in-site microwave exfoliated GO-coated $LiFePO_4$ cathode in the LIB presented a specific capacity of 158.1 mA h g^{-1} at the rate of 0.1 C and a good specific energy of 518.1 W h kg^{-1} and energy efficiency of 89.8%.[109] GO, in this case, reduced the polarisation of $LiFePO_4$ at high rate, facilitating its overwhelming performance.

Significantly, GO can be used as an active cathode material in the Li batteries. A theoretical calculation shows that Li ions can attach to GO either by forming bonds with oxygen-containing groups that is prevalent at high and medium oxygen coverages or by forming LiC_6 rings that is dominant at low coverage.[110] This suggests a new approach for use of GO as a cathode material in lithium storage. The epoxide-enriched GO, without being reduced, was found as a sustainable carbonaceous cathode material for rechargeable lithium storage, which delivered a high capacity of 360.5 mA h g^{-1} at 50 mA g^{-1} and a good cycling stability.[111] Its performance significantly surpassed those of many polymer cathodes and conventional Li-intercalated transition metal oxide cathodes. The reaction energy of -1.21 eV made the epoxide lithiation energetically favourable and the restoration of the original epoxide structure after delithiation overcoming a small barrier of 0.23 eV assured reversible lithium storage. It was also reported that in the lithium batteries, GO cathodes on stainless-steel mesh and copper mesh exhibited high initial capacities of 897.7 and 824 mA h g^{-1} respectively at 50 mA g^{-1}.[112] However, initial sharp capacity drop and large hysteresis were observed during the charge-discharge cycles of this GO electrode. Additionally, the n-Butyllithium-promoted carbonylated/hydroxylated GO was studied as

a cathode material for lithium storage, whose lithiation/delithiation process between Li^+ and oxygen groups is illustrated in Figure 8b.[105] Because this chemically functionalised GO cathode can easily contact with the electrolyte, promoting fast Faradaic reaction of the electroactive functional groups with Li-ions and rapid charge transfer reaction, it showed an enhanced Li storage properties in comparison to conventional $LiCoO_2$ and $LiFePO_4$ cathodes. It possessed an average discharge capacity of 175 mA h g^{-1} at 100 mA g^{-1} and an improved cycling stability over 600 cycles. The charge–discharge curves of the functionalised GO electrode at various current densities are presented in Figure 8c.
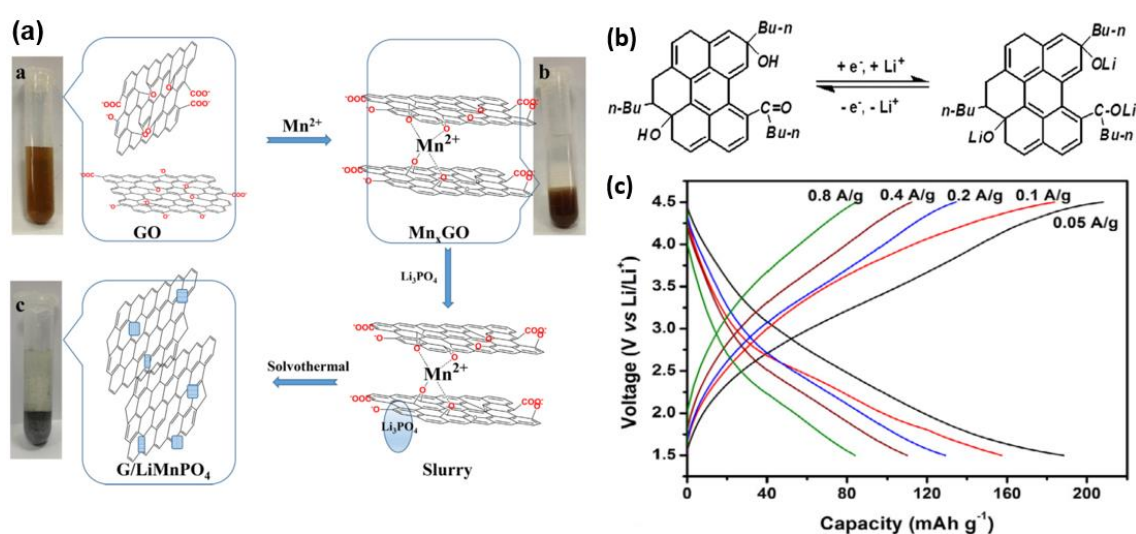
Figure 8. (a) Schematic presenting the preparative steps in the formation of $LiMnPO_4$[104]; (b) Schematic illustration of the Faradaic reactions on the n-Butyllithium-promoted carbonylated/hydroxylated GO cathode[105]; (c) Charge–discharge curves of the n-Butyllithium-promoted carbonylated/hydroxylated GO electrode at various current densities[105].

GO has also been used in the production of anode materials for lithium batteries. Although the GO is reduced eventually in the most cases, the functions of the pristine GO still cannot be negligible, which include acting as the substrate to grow the nanoparticles, prohibiting the agglomeration of materials, acting as coating layers for the formation of effective 3D networks and etc.[113,114] Various anodes supported by GO in Li batteries with the corresponding performances and the GO's specific roles are listed in Table 3, wherein GO is reduced eventually during the synthesis process. More importantly, GO can be directly used in the anodes without reduction, which mainly

contributes to the high Li$^+$ storage due to the surface oxygen functional groups.[115] **Error! Reference source not found.** presents the overview of various GO-containing anodes for use as Li batteries in which no reduction of GO is processed.

Table 3. Overview of various GO-supported anodes for use as rechargeable lithium batteries.

Anode materials	Function of GO	Electrochemical performance	Ref.
SnO$_2$/GO nanoparticles	• To provide interfacial interactions between oxygen groups and metal ions.	• A discharge specific capacity of 1148 mA h g^{-1} at 50 mA g^{-1}; • 75% of the initial capacity after 50 cycles.	[116]
GO-supported SnO$_2$ quantum dots	• To provide the interactions between fully negatively charged hydrophilic radicals and Sn^{4+}; • To facilitate the formation of the quantum dots.	• A reversible capacity of nearly 800 mA h g^{-1} at 100 mA g^{-1}; • More than 90% retention after 200 cycles.	[117]
Poly(3,4-ethylenedioxythiophene)/GO/SnO$_2$ Hollow Spheres	• To act as a scaffold for entrapping SnO$_2$ hollow spheres; • To inhibit the aggregation during the cyclic process.	• A reversible capacity of 608.4 mA h g^{-1} at 100 mA g^{-1}; • 85% of the initial capacity after 150 cycles.	[118]
GO-coated Li$_4$Ti$_5$O$_{12}$ microspheres	• To play a confined effect on the surface of TiO$_2$ spheres for the formation of nano-sized anode material.	• A specific discharge capacity of 160.1 mA h g^{-1} at 0.5 C (1 C = 175 mA h g^{-1}); • 97% retention after	[119]

		500 cycles.	
Oxygen-deficient Li$_4$Ti$_5$O$_{12-x}$ powder	• To act as a reducing agent for the conversion of Ti^{4+} into Ti^{3+} during the calcination process; • To provide oxygen vacancies for the lithium-ion diffusion.	• An initial specific discharge capacity of 172.4 mA h g^{-1} at 0.5 C; • 96.7% retention after 100 cycles.	[120]
GO/FeO composite	• To act as a reducing agent for the conversion of Fe^{3+} into Fe^{3+} during the carbothermal process.	• A reversible capacity of 857 mA h g^{-1} at 50 mA g^{-1}; • 85% retention after 60 cycles.	[113]
GO-induced nanostructured Fe$_3$O$_4$	• To provide chemically active sites for fast nucleation of nanoparticles and the growth of Fe$_3$O$_4$ nanoparticles; • To provide space to alleviate the volume change.	• An initial discharge specific capacity of 1621 mA h g^{-1} at 50 mA g^{-1}; • A reversible capacity of 1002 mA h g^{-1} at 500 mA g^{-1} after 175 cycles.	[121]
GO-encapsulated Cu$_2$O microspheres	• To act as coating layers for the formation of effective 3D networks; • To hinder the large volume change of Cu$_2$O microspheres during the charge–discharge process.	• A discharge specific capacity of 440 mA h g^{-1} at 100 mA g^{-1}; • A reversible capacity of 458 mA h g^{-1} at 100 mA g^{-1} after 50 cycles.	[122]
GO-wrapped CuO microspheres	• To act as coating layers for the formation of 3D networks in terms of the	• A discharge specific capacity of 592 mA h g^{-1} at 100 mA g^{-1};	[123]

	storage of Li$^+$; • To reduce the paths for both Li$^+$ ions and electron diffusion in the electrode.	• A reversible capacity of 313 mA h g^{-1} at 1000 mA g^{-1} after 200 cycles.	
GO-guided ultrafine Co$_3$O$_4$ nanocrystallites	• To work as an effective template to guide the deposition of Co$_3$O$_4$ nanocrystallites due to the strong covalent interaction.	• An initial discharge specific capacity of 1865 mA h g^{-1} at 100 mA g^{-1}; • 81.4% of the initial capacity after 200 cycles.	[124]
Functionalised GO-induced hydrated cupric-cobaltous oxalates	• To prevent the possibly trapping of occluded water (i.e., free water) from hydrated oxalate sample; • To play a jointly positive effect on the high-rate electrochemical performance.	• A reversible capacity of 1134.9 mA h g^{-1} at 1000 mA g^{-1}; • 91.6% retention after 60 cycles.	[114]

Table 4. Overview of various GO-containing anodes for use as rechargeable lithium batteries.

Anode materials	Function of GO	Electrochemical performance	Ref.
GO/Li$_4$Ti$_5$O$_{12}$ composite	• To provide the additional capacity via oxygen-containing functional group and nano-cavity; • To play the role of polymer binder.	• A specific discharge capacity of 201 mA h g^{-1} at 0.5 C (1 C = 175 mA h g^{-1}); • An initial charge capacity of 162 mA h g^{-1} at 30 C and less	[115]

		than 3% loss after 300 cycles.	
A sandwich composite (polyaniline/ amorphous TiO$_2$-GO/ polyaniline)	• To act as a substrate to capture the active amorphous TiO$_2$ nanoparticles; • To prevent the aggregation of the active TiO$_2$ nanoparticles for the cycling stability; • To provide an elastic butter space to accommodate the volume change of the TiO$_2$ during the cycling process.	• An initial discharge specific capacity of 1335 mA h g^{-1} at 50 mA g^{-1}; • A reversible capacity of 435 mA h g^{-1} at 100 mA g^{-1} after 250 cycles.	[125]
GO/polydopamine (PDA)-coated Si nanocomposite	• To serve as a cushion to buffer the volume change of Si nanoparticles during the cycling process; • To prevent the particle aggregations by the chemical bonding interactions.	• A discharge specific capacity of 1887 mA h g^{-1} at 210 mA g^{-1}; • A reversible capacity of 1074 mA h g^{-1} at 2100 mA g^{-1} after 300 cycles.	[126]
GO/graphite/CNTs composites	• To contribute to high capacity Li$^+$ storage through the graphite layer structure, nano-cavity and surface oxygen functional groups.	• A reversible specific capacity of 1172.5 mA h g^{-1} at 0.5 C (187.5 mA g^{-1}); • 89.6% retention after 60 cycles.	[127]
GO/graphite composites	• To facilitate the lithium storage; • To act as a binder.	• A reversible specific capacity of 690 mA h g^{-1} at 0.5 C (187.5 mA g^{-1});	[128]

		• 80% retention after 60 cycles.	

In addition to the employment in the electrodes, the GO can be used as a protective coating to prevent the corrosion of an aluminium current collector used in LIBs, which was achieved by a spin-coating approach.[129] As illustrated in Figure 9, the GO coating can (1) serve as a charge transport barrier to pitting-causing PF_6^- due to the electrostatic repulsion for suppressing Al oxidation; (2) protect the native Al_2O_3 passive layer from rapid degradation under high voltage conditions, and (3) establish direct contact with the Al surface through the defect sites of native Al_2O_3. GO also can promote the ion conductivity of solid polymer electrolyte membranes in rechargeable Li batteries, as it provides sufficient free volume voids to accelerate the transfer pathways of Li^+ ions.[130] Besides, all-solid-state lithium batteries can present an improved performance by incorporating GO into solid/gel polymer electrolytes, wherein GO has the functions of increasing ionic conductivity as well as providing additional ion-conducting paths.[131,132]
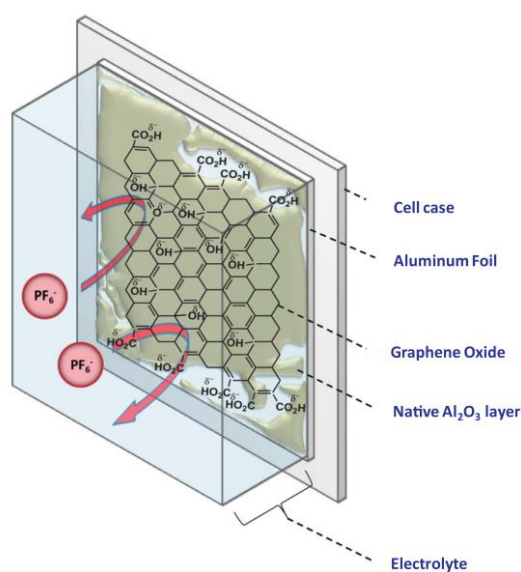
Figure 9. Schematic representation of the corrosion inhibition properties of GO when used on an Al current collector. [129]

2.4.1.2 Lithium sulphur batteries

Commercial Lithium batteries based on Li-intercalated metal oxide cathodes have reached an average cathode capacity of $\sim$250 mA h g^{-1} and an energy density of $\sim$800 W h kg^{-1}, which, however, are insufficient to meet the ever-increasing requirements of the rapidly emerging advanced technologies, e.g., electric vehicles.[133] In order to increase energy density, inexpensive, abundant, and nontoxic elemental sulphur (S) is a very promising cathode material to construct a lithium-sulphur battery, which yields a theoretical specific capacity of 1675 mA h g^{-1} with a theoretical specific energy of 2600 W h kg^{-1}. Conventional Li-S cells are composed of a Li metal anode, an organic liquid electrolyte and a sulphur composite cathode, as illustrated in **Error! Reference source not found.**a. However, the poor electrical conductivity of S or Li_2S and the formation of soluble lithium polysulphides (Li_2S_X, $3 \leqslant x \leqslant 8$) as intermediary products and irreversible solid sulphides (Li_2S_2/Li_2S) in liquid electrolyte (**Error! Reference source not found.**b) during the discharge-charge processes result in low utilisation of active materials, low Coulombic efficiency, and rapid capacity decay of the sulphur cathode.[133,134]
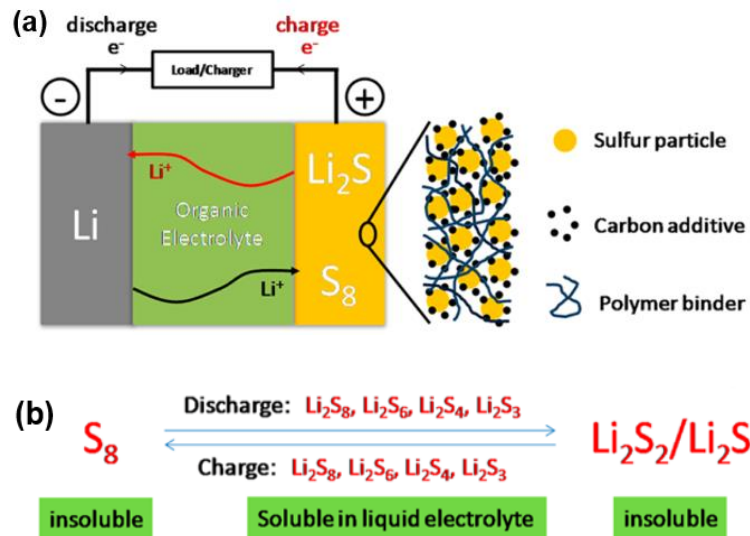
Figure 10. (a) Illustration of the charge–discharge process in a rechargeable Li-S battery[133]; (b) Charge–discharge process involving the formation of soluble lithium polysulphides and insoluble sulphides[133].

Importantly, GO has been used to accommodate and immobilise S to improve the insulating property and moderate Li polysulphide dissolution, enhancing the

electrochemical performance of Li-S batteries. GO-S nanocomposite can be prepared by an electrostatic self-assembly approach (see Figure 11a), in which the negatively charged GO sheets are coated on the surface of positively charged S microparticles [135–137], and the GO-S cathode for the Li-S cell exhibited a high reversible capacity of 950−1400 mA h g^{-1} at 167.5 mA g^{-1} and stable cycling performance[138]. This is because (1) the incorporation of sulphur can partially reduce the GO, thereby increasing the conductivity of the cathode; (2) the carbon rings and oxygen function groups of GO form chemical bonds with sulphur and thus stabilise S atoms on the GO surface and prevent the diffusion of Li polysulphides.[139] The electrochemical performances of S and GO-S electrodes are compared in Figure 11b. However, although GO can enhance the initial cycling performance of Li-S batteries, the unexpected strong chemical reactions between Li^+ and the oxygen groups of GO and immobilised S (that is, the formation and accumulation of Li_2CO_3, Li_2SO_3, Li_2SO_4 and $COSO_2Li$ insulating layers) occur on the GO–S cathode surface during the cycling process (see Figure 11c), which lower the utilisation of recyclable active S materials and hinder the in-depth ion diffusion.[140] Hence, the content of oxygen-containing groups on GO should be optimised to both increase the interaction of S with GO and minimise the unexpected chemical reactions.

Figure 11. (a) Scheme representation of the electrostatic self-assembly of GO-S composites[135]; (b) Specific capacity at different current rates of S and GO-S

electrodes[136]; (c) Schematic illustration of the discharge–charge process for the Li/GO–S battery[140].
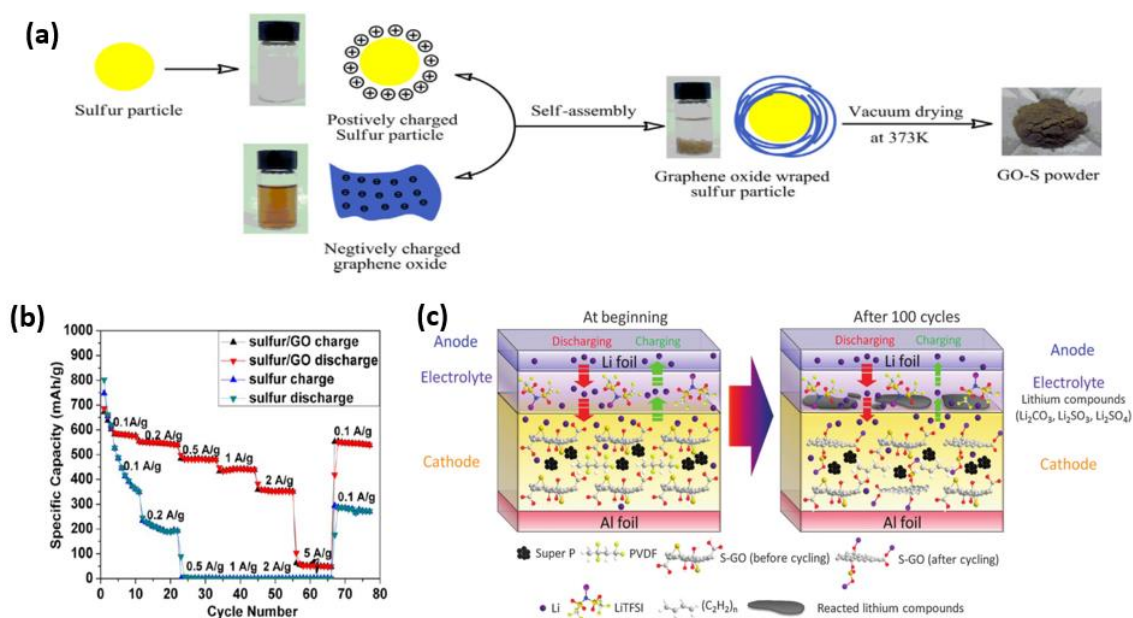
Various GO-based S or Li_2S electrodes have been developed for Li-S batteries. For example, S-encapsulated GO and mesoporous carbon hybrid nanocomposites, synthesised *via* one-step pyrolysis, presented an initial and 100th cycle discharge capacity of 1122 mA h g^{-1} and 820 mA h g^{-1} at 335 mA g^{-1}.[141] GO-wrapped hierarchical porous carbon–sulphur composite cathode in which the sulphur was melt-infused into the porous carbon and GO sheets were then coated on the surface *via* electrostatic interaction delivered an initial discharge capacity of 986 mA h g^{-1} at 1672 mA g^{-1} with capacity fading rate of 0.12% per cycle up to 400 cycles.[142] A 3D cross-linked amylopectin-wrapped GO-S composite was constructed for stabilising Li-S batteries, as the cross-linked structure confined the sulphur particles effectively among the GO layers.[143] It was afterward found that GO–S composite with a thin cross-linked polyaniline (PANI) layer exhibited a capacity retention of 80.6% after 100 cycles and an excellent Coulombic efficiency of 98.7% at 837 mA g^{-1}, where the cross-linked PANI layer functioned as an electrolyte-blocking layer to prevent the polysulfide dissolution.[144] A GO coated hollow sulphur sphere structure with the assistance of polyvinylpyrrolidone, serving as the cathode, produced a high capacity of 745 mA g^{-1} at 0.2 C after 20 cycles and 73% retention and 96% Coulombic efficiency at 1 C after 150 cycles.[145] GO-wrapped bowl-like sulphur composite with void space inside was reported as the cathode material of Li–S cells with a capacity retention of 75.2% after 300 cycles at 200 mA g^{-1} and the bowl-like S particles, synthesised by controlling the amount of surfactant, provided the void space to accommodate volume expansion generated during the cycling process.[146]

Furthermore, Li_2S-GO composite cathode for the Li-S batteries possessed a high initial capacity of 782 mA h g^{-1} and a capacity retention of 88% after 150 cycles at 233 mA g^{-1}, where GO sheets were wrapped onto the surface of Li_2S through favourable Li–O interactions.[147] A core−shell nanostructure comprising Li_2S nanospheres with an embedded GO sheet as a core material and a conformal carbon layer as a shell was proposed for a high-rate and long-life Li-S cell, which delivered an initial discharge capacity of 650 mA h g^{-1} and very low capacity decay rate of only 0.046% per cycle

with a high Coulombic efficiency of up to 99.7% for 1500 cycles at 2326 mA g^{-1}.[148] The conformal carbon coating prohibits the polysulfide dissolution, improves the electrical conductivity and provides void space to accommodate the volume expansion, and the GO acts as a second inhibitor for polysulfide dissolution, and the spherical shape of the particles shortens the solid-state Li diffusion pathway.

Significantly, GO can be applied as an electroactive interlayer between cathode and separator in a Li-S cell (as illustrated in Figure 12a), which is found to be able to improve both cathode capacity owing to a higher utilisation efficiency of polysulphides and the extra lithium storage.[149] The Li-S battery with the mildly oxidised GO interlayer exhibited an excellent initial discharge capacity of 2650 mA h g^{-1}, which was even higher than the theoretical capacity of elemental sulphur. The abnormal initial capacity included sulphur capacity and the extra capacity contributed by the reversible lithium uptake by the oxygen functional groups in the GO interlayers and the irreversible formation of lithium hydroxide. Additionally, the electrochemical performance of Li-S batteries can be enhanced by simply coating a thin GO-based barrier layer on the separator.[150] A 0.3 mg cm^{-2} GO/oxidised CNT barrier coating placed on the cathode side of the separator was capable of reducing the polysulphide shuttle that could cause the capacity fading, and of providing enough space for the migration of the lithium cations, whose Li-S cell delivered a discharge capacity of 750 mA h g^{-1} at 1 C even after 100 cycles. A unique Li-S battery configuration with an ultrathin permselective GO membrane (Figure 12b) was also reported, which afforded an improved Coulombic efficiency of 95−98% at 0.1 C and a reduced cyclic capacity decay of 0.23%/cycle.[151] When a cationic permselective GO was added in the battery, the anions of polysulphides were confined on the cathode side, thereby significantly suppressing the polysulphide shuttle. In the meantime, the lithium cations were still able to transport through the GO membrane readily, which ensured the superior performance of the Li-S cell.
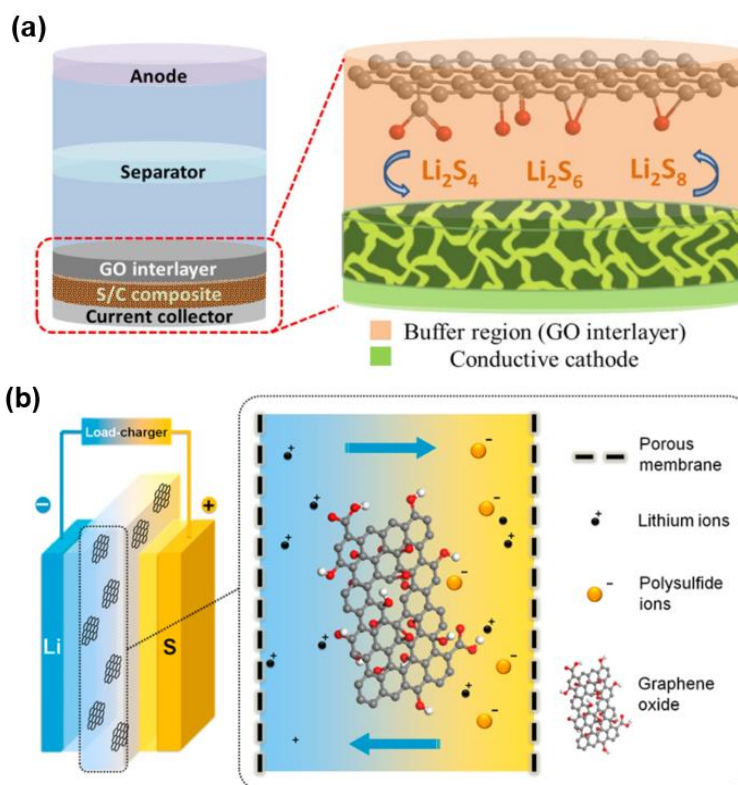
Figure 12. (a) Schematic illustrating a cell configuration with GO interlayer-cathode structure[149]; (b) Schematic of a GO membrane-incorporated a Li-S battery[151].

2.4.1.3 Lithium air batteries

Among batteries, rechargeable lithium air batteries have also attracted worldwide attention, because of the ultrahigh theoretical energy density of $\sim$11,000 W h kg^{-1}.[152,153] A typical Li-air battery is composed of a metallic Li anode, an organic electrolyte and a porous air-breathing cathode. Upon discharge, oxygen is reduced with lithium ions to form Li_2O and/or Li_2O_2 and these oxides are electrochemically decomposed to form lithium ions and oxygen during charge. However, the cathode materials of Li-air cells have met a huge challenge, which includes transport of oxygen through the pores and the deposition of insulating products on active sites for oxygen reduction and evolution.[153] Thus, highly effective carbon cathodes with hierarchal porous structure are urgently required for the higher performance of Li-air batteries. Interestingly, GO also shows its promising potential in the Li-air batteries. A free-standing and flexible GO paper (see Figure 13a), prepared by a vacuum filtration technique, was used as a lithium O_2-breathing cathode material without adding any binder or additives.[154] The Li-air battery using the GO cathode was assembled

according to Figure 13b and its electrochemical performances are shown in Figure 13c, d. It exhibited a 612 mA h g^{-1} discharge capacity and a 585 mA h g^{-1} charge capacity after 10 cycles. The unique structure of the GO paper provided various porosity for O$_2$ diffusion, thus improving the efficiency of the formation and decomposition of Li$_2$O or Li$_2$O$_2$. And the study also demonstrated that the GO paper transformed into graphene during the electrochemical cycling test. Moreover, GO can contribute to maximise the utilisation of cathodic porous carbon. A free-standing, hierarchically porous carbon derived from GO gel in nickel foam without any additional binder was produced by a facile and effective in situ sol-gel method, wherein the GO not only served as a special carbon source, but also provided the framework of a 3D gel.[155] The specific capacity of the Li-air cell using the GO-induced porous carbon cathode reached as high as 11,060 mA h g^{-1} at a current density of 280 mA g^{-1}, as the hierarchically porous structure promoted a continuous oxygen flow in the O$_2$-breathing electrode as well as provided sufficient void space for Li$_2$O$_2$ deposition.
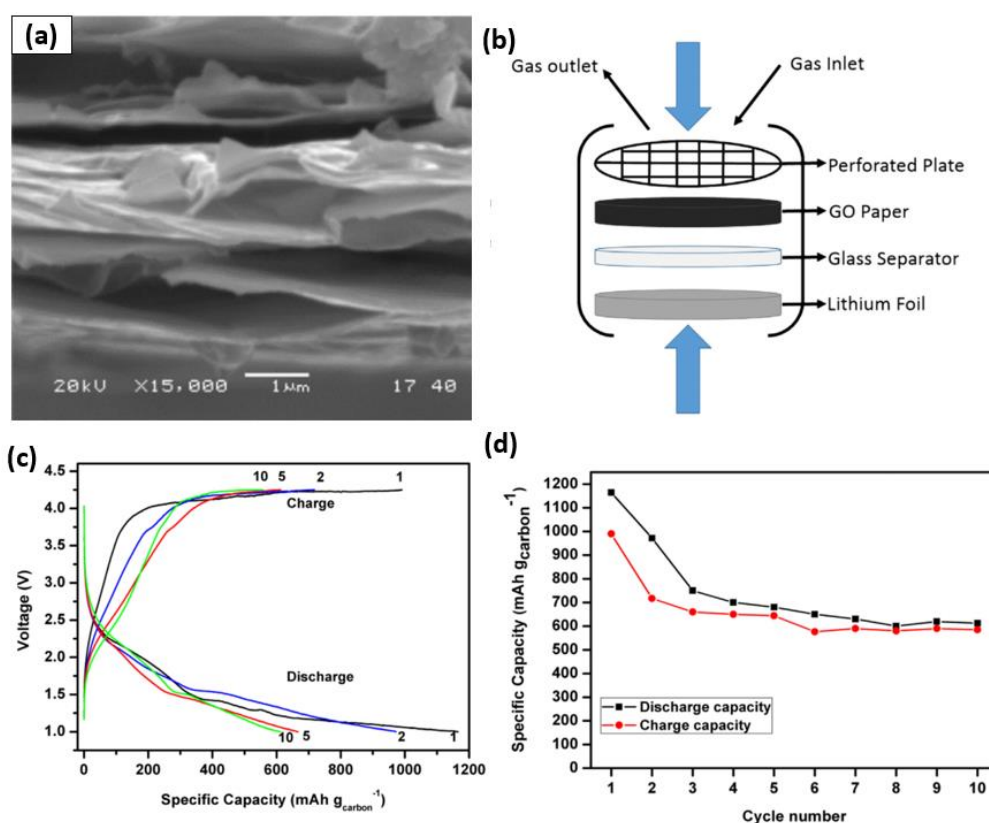
Figure 13. (a) SEM images of GO paper; (b) schematic illustration of the Li-air battery assembles with the GO cathode; (c) Charge-discharge curves of GO paper in the Li-air cell; (d) Cyclic performance of the GO paper until tenth cycle in the Li-air cell. [154]

2.4.1.4 Redox flow batteries

Redox flow batteries (RFBs) is an efficient energy storage technique that provides an alternative feasible technology of balancing power generation and consumption as well as promotes renewable energy deployment.[156] RFBs can convert and store electrical energy into chemical energy and release it in a controlled manner. As shown in Figure 14a, a typical individual RFB system consists of positive and negative electrodes immersing in soluble electroactive electrolytes, which are separated by an ion exchange membrane.[156–158] During discharge, an anolyte solution flows through a porous electrode and reacts to generate electrons, which flow through the external circuit.[158] The charge-carrying species are then transported to the ion-exchange membrane, which serves to separate the anolyte and catholyte solutions. The power density of RFBs depends on the numbers of unit cells stacked in electrical series and on the number and size of the electrodes.[156] Their energy storage capacity is determined by the concentration of electroactive species and the volume of the electrolytes. Among the RFBs, the all-vanadium, zinc/bromine, iron/chromium and polysulphide/bromide systems have been demonstrated at a few hundreds of kW and even at multi-MW levels.[159] However, only the all-vanadium and zinc/bromine RFBs have been commercialised in many countries.

The vanadium RFB system (Figure 14b) applies VO^{2+}/VO_2^+ and V^{2+}/V^{3+} redox couples in sulphuric acid as the positive and the negative half-cell electrolytes, respectively, and possesses an open circuit voltage of approximately 1.26 V at 100% state of charge.[160] It is found that the oxygen-containing functional groups on the surfaces and edges of mildly reduced GO sheets can act as active sites to improve both the reversibility and the current density of vanadium RFBs.[161–166] The oxygen functionalities facilitate the electrocatalytic activity towards VO^{2+}/VO_2^+ and V^{2+}/V^{3+} redox couples, as displayed in Figure 14c.[165] For the negative electrolyte, the V^{3+} ions are adsorbed on the hydrophilic functional groups by removing the protons, while the V^{3+} ions are reduced to the V^{2+} ions that are then diffused from the graphene sheet.

Regarding the positive electrolyte, the VO^{2+} ions are oxidised at the active sites and simultaneously produce protons and H_2O molecules. Subsequently, the diffusion process in the form of VO_2^+ ions occurs in the electrolyte.
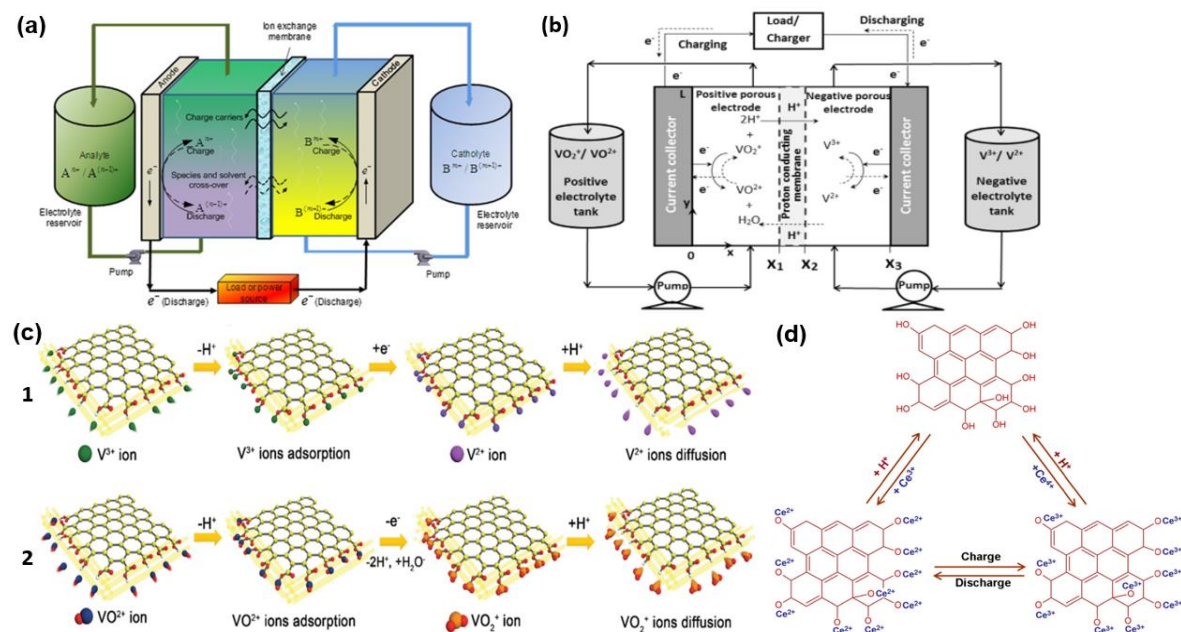
Figure 14. (a) A schematic diagram of a typical redox flow battery[158]; (b) A schematic representation of an all-vanadium redox flow battery system[159]; (c) The proposed catalytic mechanism of vanadium redox reaction with the oxygen functional groups: 1. V^{2+}/V^{3+} and 2. VO^{2+}/VO_2^+ redox reactions[165]; (d) The catalytic mechanism of GO toward Ce^{3+}/Ce^{4+} redox reaction[167].

Therefore, given the contribution of the oxygen functional groups in the vanadium RFBs, GO nanoplatelets without reduction, which present a quasi-2D layered structure and a large quantity of active groups at the basal planes and edges, were directly used as electrochemical active materials for VO^{2+}/VO_2^+ and V^{2+}/V^{3+} redox couples.[160] The experimental results showed that although the reversibility towards the positive VO^{2+}/VO_2^+ was not improved, the addition of GO was able to significantly enhance the reversibility between V^{2+} and V^{3+} and increase the peak current for both VO^{2+}/VO_2^+ and V^{2+}/V^{3+} redox reactions, compared with the pristine graphite. This was because the relatively large active surface area and abundant oxygen groups allowed the GO to play an electrocatalytic function during the redox reaction of vanadium species, that is, to facilitate the adsorption of the reactive ions onto the electrode surface. However, electrodes using the pure GO exhibited a low rate capability due to the inferior

electrical conductivity, thus delivering a limited energy efficiency and power capability.[168] Consequently, the GO sheets were assembled onto the multiwalled CNT surfaces to form an electrocatalytic hybrid with an effective mixed conducting network. The hybrid not only provided a rapid electron and ion transport capability but also delivered a much better electrocatalytic redox reversibility of VO^{2+}/VO_2^+ couple, especially for the reduction from VO_2^+ to VO^{2+}.[168]

In addition to the all-vanadium RFBs, application of GO as the electrocatalytic electrode material in other RFBs was also reported. For example, the GO-based electrodes mixing with polymer binder in a vanadium bromide RFB presented a better electrochemical performance than the pristine graphite, including lower overvoltage for both Br^-/Br^{3-} and V^{3+}/V^{2+} redox couple reactions and higher peak currents for the V^{3+}/V^{2+} redox couple.[169] The study also demonstrated that the oxygen-containing groups on the GO sheets generated ample active sites to electrochemically catalyse the redox reactions. Moreover, a nano-porous GO electrode was investigated as an active anode material in cerium vanadium RFB and the nano-pores containing oxygen functional groups was found to provide a remarkable electrocatalytic activity towards Ce^{4+}/Ce^{3+} redox couples.[170] A zinc cerium RFB using a graphite/GO composite positive electrode also exhibited a significantly improved electrochemical performance when 2.5 wt% GO was added into graphite electrode.[167] Because of the presence of oxygen groups and large surface area introduced by the GO, the composite electrode possessed a much larger redox peak current of Ce^{3+}/Ce^{4+} and a reduced charge transfer resistance. Figure 14d illustrates the catalytic mechanism of GO toward Ce^{3+}/Ce^{4+} redox reaction.

One of the key components of the RFBs is the ion exchange membrane, which is responsible for ion transport and preventing the cross-mixing of the positive and negative electrolytes that are stored in separate tanks.[156] A desirable ion exchange membrane should have a high proton conductivity, low vanadium ion permeability, excellent stability, mechanical strength, and cost-effectiveness.[171] Importantly, the incorporation of GO in a polymer membrane is determined to increase the proton conductivity and mechanical strength.[172] Besides, when GO is added in the Nafion membrane that is used in the vanadium RFBs, the GO can act as effective barriers to

inhibit the transport of vanadium ion, thus significantly decreasing the vanadium ion permeability.[173,174] Likewise, the sulfonated poly(ether ether ketone) (SPEEK) membrane with GO loading, investigated in a vanadium RFB, exhibited a stable cycling performance (up to 1200 cycles) with a high coulombic efficiency of ∼99% and a relatively low capacity decline in comparison to the pure SPEEK membrane.[171] The embedding of GO is capable of improving the performance of the ion exchange membranes due to the following reasons[171]: (1) GO sheets can prevent the transport of vanadium ions because of the increase in tortuosity; (2) the oxygen functional groups of GO can form hydrogen bonds with polymer chains, which is beneficial for the formation of the hydrophobic/hydrophilic separation structure in the acquired composite membranes, and hence the enhancement of ion selectivity; (3) the strong interaction between GO and the polymer can improve the mechanical stability of the membrane; (4) GO itself possesses a high proton conductivity.

2.4.1.5 Other batteries

Because of the cost effectiveness, high abundance and adequate redox potential of elemental sodium ($E^o_{(Na+/Na)}$ = −2.71 V versus SHE) that is merely 0.3 V above that of lithium, sodium-ion batteries have emerged as an attractive alternative for electrochemical energy storage applications.[175–177] The principle of cell operation of sodium-ion batteries is quite similar to that occurring in the LIBs: upon discharge and charge, sodium ions are transported between cathode and anode through a non-aqueous or aqueous sodium ion-based electrolyte. The metallic sodium is not employed as the anode owing to dendrite formation and interface aging problems. Instead, anode materials normally include hard carbons or metal oxide intercalation compounds. The best candidates to be cathode materials in a Na-ion battery to date are layered sodium transition-metal oxides.

Noteworthy is that GO makes a particular contribution to developing the Na-ion batteries, although it does not function as an active material. Carbonyl group-based croconic acid disodium salt as an anode material in the sodium ion battery presented a high capacity of 246.7 mA h g^{-1} but with a fast capacity decay, which was ascribed to the particle pulverisation, triggered by a serial phase transformation during charge/discharge process.[178] The GO-wrapped croconic acid disodium salt particles

with smaller size provided a higher capacity of 293 mA h g^{-1} and improved cycling stability, as the pulverisation was effectively suppressed by minimising the particle size. Furthermore, although hard carbon is an attractive anode candidate material in Na-ion batteries, it suffers a low first-cycle Coulombic efficiency and fast capacity fading.[179] As the first-cycle Coulombic efficiency for carbon anodes of LIBs can be increased by lowering the surface area, an effective approach to reduce the surface area of sucrose-derived hard carbon by introducing GO dispersion into the sucrose solution was reported.[179] The as-prepared hard carbon possessed a lower specific surface area of 5.4 m^2 g^{-1} and an improved first-cycle Coulombic efficiency from 74% to 83%. GO, as a dehydration agent, prevented foaming of sucrose during caramelisation or dehydration as well as helped spread the burnoff over a wider range of temperatures during pyrolysis, both of which facilitated the smaller surface area of the final product.

A GO-MnO$_2$ air cathode was prepared by depositing GO on the surface of a MnO$_2$ air cathode using thermal evaporation at 50°C from a GO colloidal suspension, and was used in an alkaline tin-air cell.[180] Such cell delivered a maximum power density of 13 mW cm^{-2}, higher than that using the pure MnO$_2$ cathode (9.2 mW cm^{-2}). This is because GO accelerates the process of electron donation to the MnO$_2$ and to adsorbed oxygen atoms. As shown in Figure 15a, electrons are transferred efficiently from the GO and electrochemically reduced GO (ERGO) to the conduction band of the MnO$_2$, which can increase the rate of electron excitation process. Moreover, as GO has a high proton conductivity and sulphuric acid affinity, the GO paper was used an electrolyte substitute for sulphuric acid to fabricate a solid-state lead acid battery, which exhibited the stable charge/discharge cycles.[181] Figure 15b illustrates the models of the overall electrochemical reactions occurring in the small-sized PbO$_2$/PbSO$_4$//GO//PbSO$_4$/Pb cell with a total thickness of 1.5$-$2.0 mm.
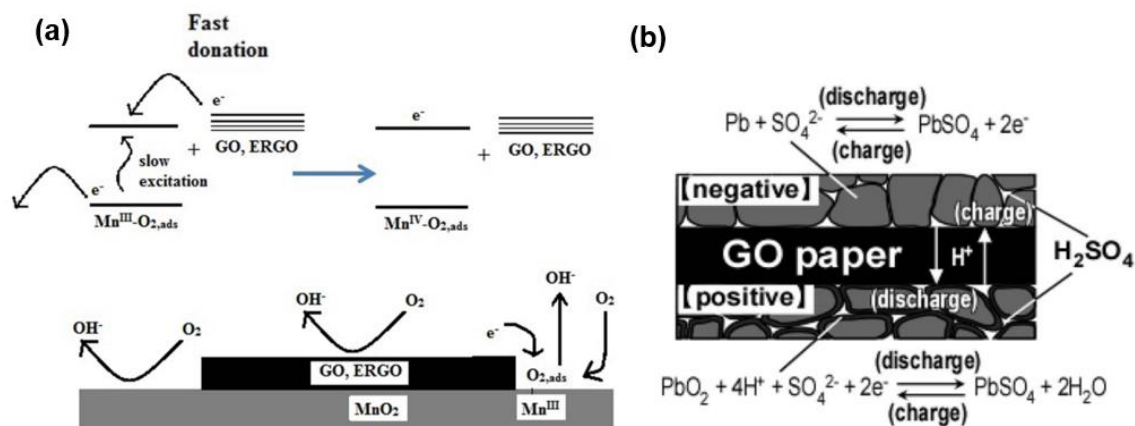
Figure 15. (a) Diagram of the electron donating effect of GO and ERGO on MnO_2[180]; (b) Illustration of the models of the total reactions in the GO lead battery[181].

2.4.2 Dielectric capacitors

Dielectric capacitors are the traditional electrical capacitors that store energy through potential field-induced polarity of dielectric medium.[182] A dielectric capacitor is composed of two conducting electrodes separated by an insulating dielectric spacer.[183] Such dielectric medium is required to have a high dielectric constant and low dielectric loss for the maximum capacitance. It was presented that a GO-encapsulated CNT hybrid, synthesised by $\pi - \pi$ interactions between negatively charged GO and positively charged CNTs, possessed not only a high dielectric constant and low dielectric loss, but also a highly enhanced breakdown strength and maximum energy storage density.[184] The GO shells (1) effectively enhanced the dispersion of CNTs; (2) served as insulation barriers to decrease dielectric loss; and (3) increased the charge scattering due to their ultrathin structure and insulating property, resulting in an increase of breakdown strength.

More significantly, a hydrated GO film was used as a dielectric spacer between two stainless steel electrodes to construct a prototype water-dielectric capacitor, as shown in Figure 16.[183] Actually, high-purity water is prone to become conductive due to leaching of ions from the environment, although it has a sufficiently high dielectric constant for dielectric capacitors. However, when water is confined between GO sheets by hydrogen bonding, it can retain its insulating nature and behave as a dielectric. It was demonstrated that the hydrated GO film showed a high dielectric capacitance of

100−800 μF cm^{-2} depending on the water content and when a breakdown voltage was applied, this hydrated GO was able to restore its capacitance by a self-recovery mechanism as a consequence of the reversible reduction–oxidation process.
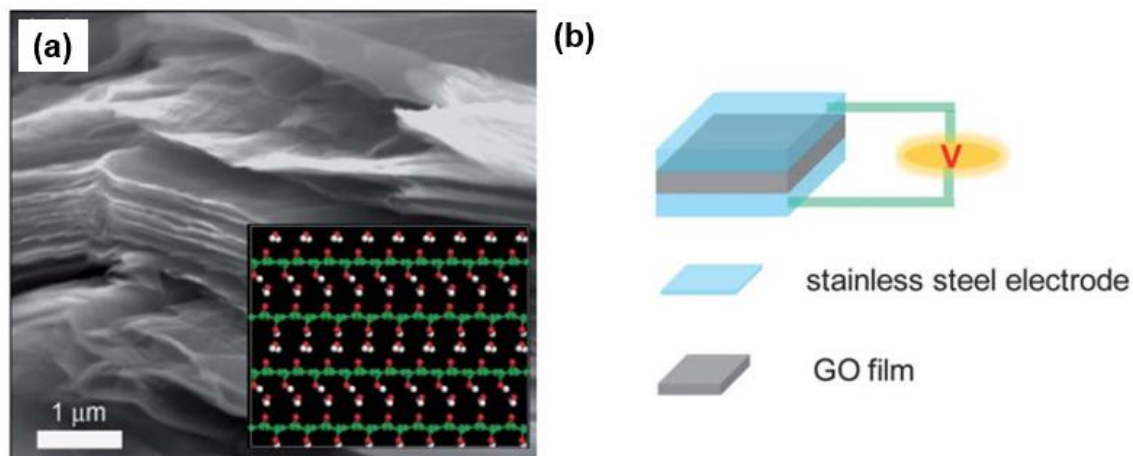
Figure 16. (a) Cross sectional SEM image of a hydrated GO film with the inset showing the hydrogen bonding between water molecules and GO sheets; (b) Scheme illustrating the assembly of a water-dielectric capacitor with a hydrated GO film as a dielectric spacer.[183]

2.4.3 Supercapacitors

Supercapacitors (SCs), also called electrochemical capacitors, are the high-performance energy storage devices with excellent power capability, short charge-discharge time, long cyclic life and outstanding reversibility.[185] The structure of the SC, similar to that of a battery, comprises two electrodes in contact with an electrolyte solution separated by a separator. Charge storage in SCs is principally based on either the pure electrostatic charge accumulation at the electrode-electrolyte interface, i.e. electrical double layer capacitance, or the fast and reversible Faradaic processes on the electrode surface, i.e. pseudo-capacitance.[185,186] Because of the diffusible ions and the tremendous electrode/electrolyte interfaces, SCs normally deliver a specific capacitance of tens or even hundreds of F g^{-1} and F cm^{-2}, while dielectric capacitors usually can merely contain up to tens or hundreds of μF cm^{-2}.[182] However, SCs store electrical charge only at the electrode surface rather than within the entire electrode so that they deliver lower energy densities compared with batteries.[187] GO, in virtue of the intriguing properties, has been developed in the enhancement of the performances

of SCs. The applications of GO in the SCs in terms of electrodes and solid-state electrolytes will be discussed below.

2.4.3.1 Contributions in electrodes

GO is probably a good choice as an electrode material for SCs, as it possesses not only a large surface area but also abundant oxygen functional groups that can provide a large additional pseudo-capacitance and improved wettability of the electrodes in electrolytes.[188] As shown in Figure 17a, GO exhibits a higher current density and a longer charge–discharge time, indicating a higher capacitance than graphene. The pseudo-capacitance of GO possibly originates from electrochemical reactions, e.g. $>C-OH \leftrightarrow >C=O+H^+ + e^-$ etc., at the electrode interfaces. The GO electrode was found to be able to deliver a maximum specific capacitance of 146 F g^{-1} and an energy density of 20.39 W h kg^{-1}.[189] An asymmetric SC using $LiCoO_2$ as a positive electrode and GO as a negative electrode in an aqueous $LiClO_4$ electrolyte presented the maximum energy and power densities of 19.05 W h kg^{-1} and 8.7 kW kg^{-1} respectively, and a long cyclic life with 85% specific capacitance retention after 1500 cycles.[190] The 3D porous GO on conductive stainless steel substrate, produced by an electroplating deposit method, was used as electrodes of the SC without adding binders or conductive additives and it achieved a capacitance, energy and power density of 493 F g^{-1}, 49.9 W h kg^{-1}, and 1700 W kg^{-1} even at 4 A g^{-1}, as well as retained ~97.83% of initial capacitance after 10,000 cycles.[191] The 3D porous nanostructure was advantageous, as it contributed more active surface area for accommodating charges and suitable pathways for charge transport.

Nonetheless, the inferior electrical conductivity of GO, to some extent, limits the performances of SCs. Various GO-based composites incorporating conventional electrode materials of SCs, therefore, are studied. Electrode materials of the SCs can mainly be divided into three categories: carbonaceous materials, transition metal oxides/nitrides/sulphides, and conductive polymers.[192] The GO and single-walled CNT composite ink with a mass ratio of 1:5 reached a highest specific capacitance of 295 F g^{-1} at a current density of 0.5 A g^{-1} and a capacitance retention of 85% after 60,000 cycles.[193] A core–shell heterostructure with multi-walled CNTs as the core and GO nanoribbons as the shell was fabricated as a SC electrode material in which

GO shell provided more active sites for electron accumulation and the inner CNT core contributed highly conductive paths for electron transport.[194] The specific capacitance of 252.4 F g^{-1} at a scan rate of 50 mV s^{-1} and the retention of more than 87% over 1000 cycles were obtained. Moreover, a flexible solid-state symmetric SC including the GO-rGO (reduced GO) patterned electrodes, which were prepared through region-specific UV-induced mild reduction of GO films, and the polymer gel electrolyte showed a capacitance of 141.2 F g^{-1} at 1 A g^{-1} and a good stability over 2000 cycles.[195] And an asymmetrical SC using a GO/cobalt(II)tetrapyrazinoporphyrazine composite as the positive electrode and GO/carbon black as the negative electrode in a Na_2SO_4 electrolyte delivered good specific capacitance, energy and power densities of ~500 F g^{-1}, 44 W h kg^{-1} and 31 kW kg^{-1}, respectively.[196] Significantly, using different electrolytes can affect the performance of the GO-based electrodes. It was reported that the SC based on GO/carbon electrodes displayed specific capacitances of 238.0 and 98.8 F g^{-1} at 0.5 mA cm^2 in Li_2SO_4 and Na_2SO_4 electrolytes, respectively, which was attributed to the larger electrochemically active areas for Li and the higher diffusion coefficient of Li^+ in the GO-based electrodes.[197]

With respect to transition metal oxide electrodes, GO can serve as a template to synthesis layered MnO_2 nanosheets for increasing the surface area[198] and also be incorporated into the MnO_2 electrode for enhancing the capacitance[199–202]. The GO-MnO_2 hybrid electrodes reach a specific capacitance of ~360.3 F g^{-1}, higher than that of pure MnO_2 nanowire electrodes (128.0 F g^{-1}) and commercial MnO_2 microparticles electrodes (22.8 F g^{-1}).[200] The functional groups of GO, functioning as anchor sites, enable the in-situ formation of MnO_2 nanoparticles attaching on the surfaces and edges of GO sheets (Figure 17b), which not only enlarge the specific surface area but also prevent the aggregation of GO and MnO_2. Likewise, the GO/Mn_3O_4 composite thin film prepared by a LBL technique exhibited a specific capacitance of 344 F g^{-1} at 5 mV s^{-1}[203] and the GO anchored porous MnS nanocrystals *via* a facile hydrothermal method based on the Kirkendall effect delivered a 390.8 F g^{-1} capacitance at 0.25 A g^{-1}[204], wherein GO had the functions of providing appropriate channels for ionic transport and pathways for fast electron transfer. Additionally, by means of an electrophoretic deposition or hydrothermal process or electrostatic coprecipitation, nickel oxide, nickel sulphide and copper oxide can be

attached on the surfaces of GO nanosheets for high-performance SCs, which achieve the specific capacitances of 569 F g^{-1} at 5 A g^{-1}[205], 800 F g^{-1} at 1 A g^{-1}[206], 245 F g^{-1} at 0.1 A g^{-1}[207], respectively. The interaction of the GO and the metal oxides/sulphides is believed to have a synergistic effect on the performance of SCs. It was also reported that both NiCo$_2$O$_4$ nanowires and ultrafine nanoparticles were deposited on the surface of GO substrate under microwave irradiation and the presence of GO significantly enhanced the retention at even higher current densities.[208] Such nanocomposites showed a superior performance as electrodes in the SC with a specific capacitance of 735 F g^{-1} retained at the current density of up to 33 A g^{-1}. GO can also promote the nucleation and in-situ growth of Co-Al layered double hydroxide nanosheets and Figure 17c illustrates the synthesis process of the Co-Al/GO composite during which positively charged Co–Al hydroxides and negatively charged GO sheets are self-assembled *via* electrostatic interactions.[209,210] A specific capacitance of 772−1030 F g^{-1} at 1 A g^{-1} and a 80% capacitance retention when the current density increased to 20 A g^{-1} were obtained. GO inhibits the aggregation of layered hydroxide nanosheets and the layer-by-layer assembly optimises the contact area of GO and Co-Al sheets, both of which are favourable for effective electron transport between active materials and the charge collector.[209]
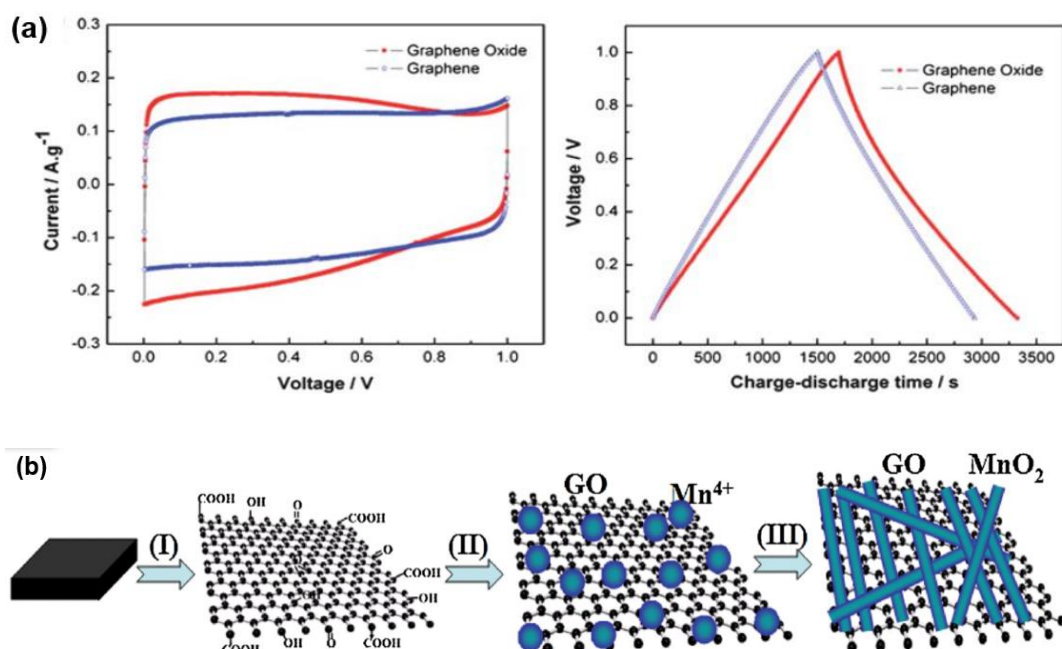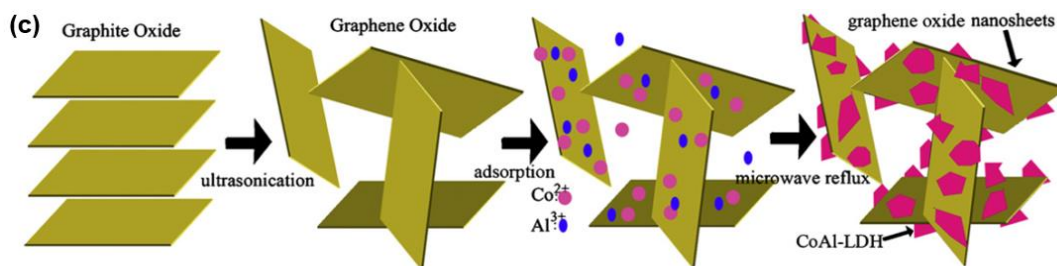
Figure 17. (a) The electrochemical capacitive behaviour of GO and graphene in cyclic voltammetry and charge–discharge curves[188]; (b) Illustration of GO/MnO$_2$ hybrid formation[200]; (c) Schematic for the synthesis process of Co-Al/GO composite[209].

Electroactive polymers, though they can provide a large pseudo-capacitance, exhibit a swelling behaviour during the redox processes that degrades the cycling stability.[211] In order to overcome this drawback, GO is widely used to functionalise the conducting polymers for high-performance SCs. The preparation of conducting polymer–GO sheets can normally be achieved by an electrostatic interactions between negatively charged GO sheets and positively charged surfactant micelles, as illustrated in Figure 18a.[212] When the surfactant micelles are electrostatically adsorbed on the GO surfaces, the addition of polymer monomer enables the monomer to be predominately solubilised in the hydrophobic cores of the surfactant micelles and subsequently the polymerisation can undergo predominately in the micelle cores. For instance, the GO/polyaniline (PANI) nanocomposite can be synthesised by in situ polymerisation[213–216] and Figure 18b presents three possible combining modes of GO and PANI composite, which include (1) $\pi - \pi$ stacking, (2) electrostatic interactions, and (3) hydrogen bonding.[217] The GO/PANI hybrids possess higher surface area and larger pore volume compared to the pure PANI, which increase the contact area of PANI nanoparticles with the electrolyte, facilitating the fast transport of electrolyte ions and electrons into the active sites of the composite electrode.[214,218,219] Besides, the oxygen functional groups on GO not only enable an easy access to ion transportation but also produce an additional pseudo-capacitance.[218,220] These features endow the GO/PANI electrodes with an increased capacitance. The specific capacitance of around 550 F g^{-1} at 0.2 A g^{-1} was reported for the GO/PANI composite, which was higher than that of the pure PANI electrodes (216 F g^{-1}).[219–221] The synergistic effect of GO and PANI also improve the cycling stability, as GO sheets endure some mechanical deformation during the Faradaic process of PANI, preventing

the destruction of the electrode material.[219] Normally, an 89 − 92% capacitance retention of the GO/PANI electrodes can be observed.[222]

Similarly, GO/polypyrrole (PPy) nanocomposites can be produced *via* either an in situ chemical polymerisation method[223–227] or an electrochemical codeposition (see Figure 18c) [228,229]. The GO/PPy composite electrodes show high specific capacitance, good rate capability and cycling stability due to their synergistic effects, e.g., a specific capacitance of 633 F g^{-1} at 1 A g^{-1} and a 6% capacitance attenuation after 100 cycles were reported, in contrast to the pure PPy with 227 F g^{-1} and 68% retention.[230] An asymmetric SC based on the GO/PPy positive electrode and activated carbon negative electrode was cycled reversibly within 0–1.6 V and reached the maximum energy density of 21.4 W h kg^{-1} at a power density of 453.9 W kg^{-1}.[225] Importantly, sodium dodecylbenzene sulfonate acting as a soft template and stabiliser can promote the intercalation of PPy into layered GO during an polymerisation process, as the addition of sodium dodecylbenzene sulfonate is favourable for homogeneous nanocomposite formation, as well as for enhanced surface wettability and accelerated electron transport and ion insertion/extraction in the electrode material during the fast charge–discharge processes.[231] Moreover, a 3D GO-based benzimidazole-crosslinked network material was prepared through the covalent crosslinking of GO sheets using a condensation reaction between the carboxylic acid groups on the GO surface and the o − aminophenyl end groups of 3,3 − diaminobenzidine (or 1,2,4,5−benzenetetraamine tetrahydrochloride), as presented in Figure 18d, wherein the GO sheets as the building blocks contributed the porous material with a high surface area.[232] Such GO/benzimidazole crosslinked composite with an increased specific surface area up to 920 m^2 g^{-1} showed a specific capacitance of 370 F g^{-1} at 0.1 A g^{-1} and a capacitance retention of 90% after 5000 cycles at 3 A g^{-1}.

Thus, the superior electrochemical performances of the GO/conducting polymer composites can be concluded as follows: (1) GO provides a large accessible surface for the conducting polymers; (2) 3D or layered composite structures enhance the mechanical strength to stabilise the polymers during the cycling processes; (3) the GO/polymer nanostructure effectively reduces the dynamic resistance of electrolyte ions; and (4) the oxygen functional groups of the GO sheets contribute a large

additional pseudo-capacitance to the overall energy storage.[212] In addition, it is interestingly found that GO, single-walled CNTs and conjugated polymers of poly(3,4-ethylene-dioxythiophene) and poly(styrenesulfonate) *via* a synergistic assembly in aqueous solution can create an adhesive and conductive glue that can be used as a conductive binder to embed insulating metal oxide powders for fabricating high-performance SC electrodes.[233]
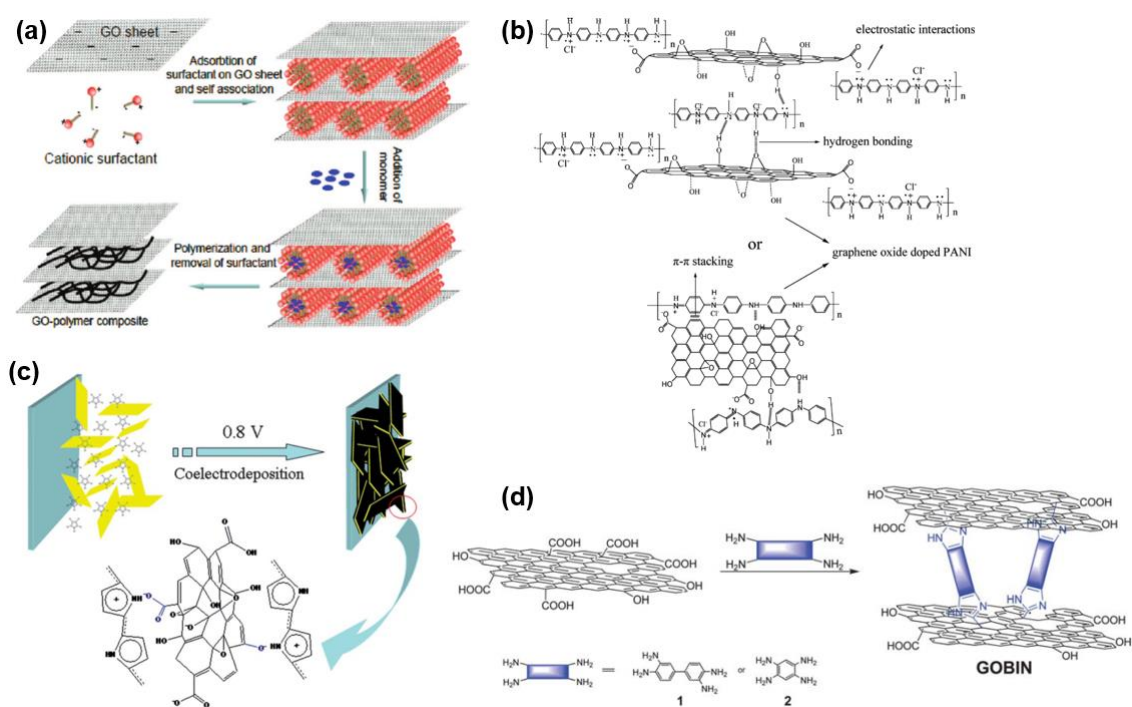
Figure 18. (a) Schematic illustration of the formation process of GO/conducting polymer composites[212]; (b) Three possible combining modes of GO and PANI composite[217]; (c) The electrochemical codeposition for the synthesis of GO/PPy nanocomposites[229]; (d) Scheme of the formation of the GO-based benzimidazole-crosslinked material[232].

Furthermore, the combination of GO and a mixture of metal oxides and/or conducting polymers and/or carbon materials are proposed as SC electrode materials and their corresponding specific capacitances and cycling performances are presented in Table 5.

Table 5. Overview of various three-component GO-based electrode materials for SCs

Samples	Specific capacitance	Retention capacitance	Ref.
MnO$_2$/PANI/GO	512 F g^{-1} at 0.25 A g^{-1}	97% after 5000 cycles	[234]
TiO$_2$/PANI/GO	430 F g^{-1} at 1 A g^{-1}	–	[235]
ZnO/PPy/GO	94.6 F g^{-1} at 1 A g^{-1}	74% after 1000 cycles	[236]
MnO$_2$/CNT/GO	360 F g^{-1} at 5 mV s^{-1}	94% after 1000 cycles	[237]
NiO/glassy carbon/GO	890 F g^{-1} at 5 mV s^{-1}	–	[238]
PANI/Carbon nanofiber/GO	450.2 F g^{-1} at 10 mV s^{-1}	90.2% after 1000 cycles	[239]

2.4.3.2 Contributions in solid-state electrolytes

It is generally acknowledged that GO possesses a superior proton conductivity property, due to the presence of the hydrophilic sites in GO, i.e., −O−, −OH, and −COOH functional groups, which attract the protons and propagate through hydrogen-bonding networks along the adsorbed water film.[240,241] The high proton conductivity allows GO to be used as a solid-state electrolyte in the SCs. A micro-SC using the reduced graphite oxide as the electrodes and the graphite oxide (multilayer GO) as the solid electrolyte gave a highest capacitance of 0.51 mF cm^{-2}.[242] This study also indicated that the graphite oxide, owing to the substantial amounts of adsorbed water, was able to function as a good ionic conductor and an electrical insulator, which made it simultaneously to be an electrolyte and an electrode separator with ion transport characteristics similar to that observed for Nafion membranes.

The SCs using the liquid electrolytes have two main disadvantages, including (1) low package energy density due to the requirement of high-standard safety encapsulation materials, and (2) the leakage of the liquid electrolytes that probably causes an environmental risk.[243] Thus, all-solid-state SCs are attractive in the future practical applications. An all-solid-state SC using the graphene-doped carbon electrodes and a GO-doped ion gel as a gel polymer electrolyte and separator was reported, which delivered a specific capacitance of 190 F g^{-1} and energy density of 76 W h Kg^{-1} at 1 A g^{-1}.[243] Such gel membrane was prepared by mixing copolymer poly(vinylidene

fluoride-hexafluoro propylene (P(VDF-HFP)) and ionic liquid 1-ethyl-3-methylimidazolium tetrafluoroborate (EMIMBF$_4$) with GO and the function of GO is explained in Figure 19a.[243,244] Without adding the GO, the ions can only transport through the disordered amorphous pathway of the gel electrolyte (Figure 19a, 1).[244] The addition of GO can decrease the degree of crystalline in the ion gel, as the abundant oxygen-containing groups on the GO sheets can interconnect with the copolymer to form a "highway" for ion transport, which results in higher ionic conductivity, as illustrated in Figure 19a, 2. However, the more addition of GO is expected to cause the restacking of GO sheets and the blocking effect by the excessive GO as shown in Figure 19a, 3, thus deteriorating the ionic conductivity. Furthermore, a new family of boron cross-linked GO/polyvinyl alcohol (GO-B-PVA) nanocomposite gel electrolyte was synthesised through a freeze-thaw/boron cross-linking method and then assembled into an electric double layer capacitor, as presented in Figure 19b.[245] GO functioned as a promoter for the ionic conductivity and the boron atoms played a role as physical or chemical cross-linkers of the PVA matrix to improve the thermal stability and the mechanical properties of GO-PVA hybrid. As a result, the SC using 20wt% GO-B-PVA/KOH gel electrolyte exhibited a stable cycling performance up to 1000 cycles and a higher discharge capacitance of 190 F g^{-1} at 0.1 A g^{-1} compared to that using the aqueous KOH electrolyte (109.4 F g^{-1}).
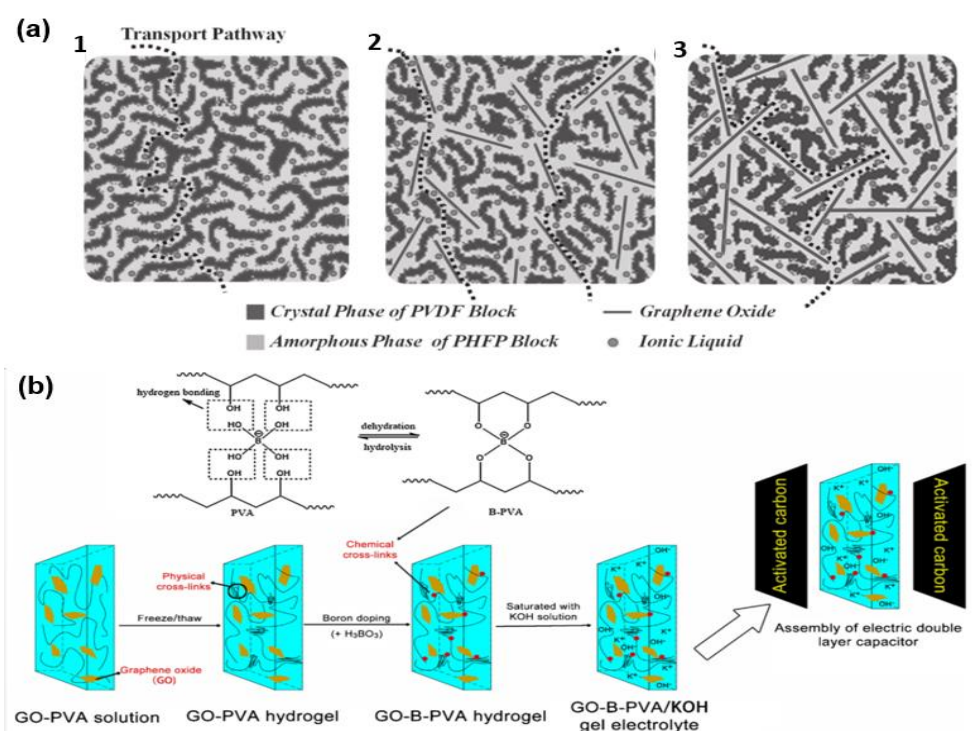
Figure 19. (a) Proposed schematic structures of GO-doped ion gels with different GO doping mass fraction:1) pure ion gel; 2) ion gel with optimised GO doping; and 3) ion gel with excess GO doping[244]; (b) Schematic for assembly of GO-B-PVA nanocomposite gel electrolyte[245].

2.4.4 Fuel cells

A fuel cell is an electrochemical conversion device that generates electricity *via* chemical redox reactions when supplied with a fuel, e.g., hydrogen, natural gas, or methanol, and an oxidant, e.g., oxygen, air, or hydrogen peroxide.[246–250] It consists of an anode, cathode and electrolyte, as shown in Figure 20a. When the fuel is supplied to the anode, the oxidation of the fuel occurs by an anodic reaction, which is accompanied with the production of electrons and either the formation of ionic species that travel through the electrolyte to the cathode or formation of compounds by reaction between the fuel and the ionic species transported through the electrolyte from the cathode to anode.[247] The electrons originated from the anodic reaction flow through the outer electrical circuit to the cathode, thus generating the power. In the cathode, consumption of electrons and either reaction between oxygen and ionic species or the formation of oxygen anions that travel through the electrolyte from the cathode to the anode happen. According to the choice of fuel and electrolyte, fuel cells can be categorised into 7 main types, which include (1) proton exchange membrane fuel cell (PEMFC); (2) direct methanol fuel cell (DMFC); (3) alkaline fuel cell (AFC); (4) phosphoric acid fuel cell (PAFC); (5) molten carbonate fuel cell (MCFC); (6) Solid oxide fuel cell (SOFC); and (7) direct ethanol fuel cell (DEFC).[247,248] Figure 20b presents the characteristics of these fuel cells based on fuel and oxidant, anodic and cathodic reactions, electrolytes and operating temperature range.[247] Noteworthy is that GO makes great contributions to the enhancement of electrocatalytic activities and the fabrication of the membranes in the fuel cells, e.g. PEMFC, DMFC, AFC, DEFC, which are discussed below.
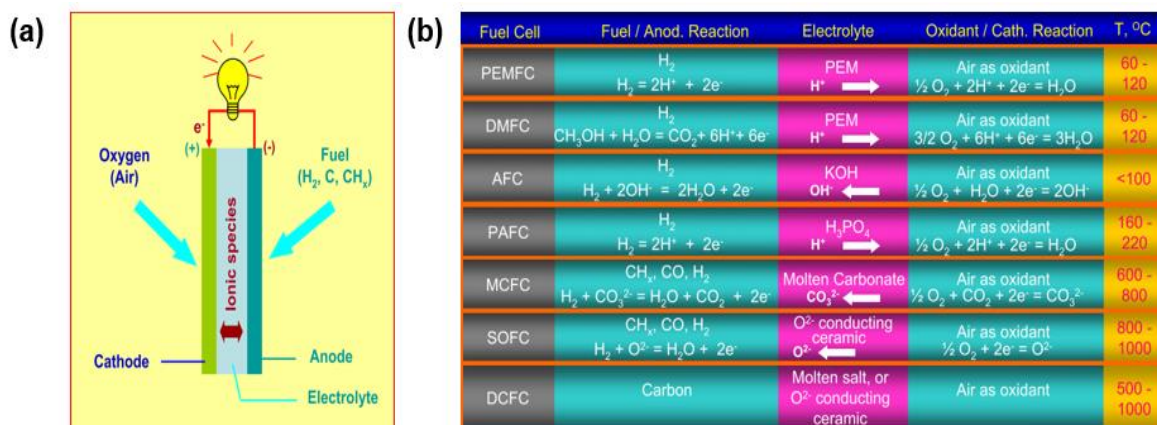
Figure 20. (a) The basic operating principle of a fuel cell; (b) Various types of fuel cells and their characteristics.[247]

2.4.4.1 Contributions in electrocatalytic activities

Platinum (Pt) has been widely used as an effective electrocatalyst in fuel cell technology for the electro-oxidation of fuel at the anode and electro-reduction of oxygen at the cathode.[251] Pt catalyst is normally supported on the high surface area carbon material such as carbon black. However, the oxidation of the carbon black can easily occur at the potential of oxygen reduction reaction, which hence causes the agglomeration and loss of Pt nanoparticles, decreasing the electrochemical surface area and the electrocatalytic activity. Importantly, it is found that the addition of small amount of GO greatly increases the durability of commercial Pt/C catalyst without sacrificing initial electrochemical active surface area.[251] This is because the GO can provide the anchoring sites of eluted metal ions, thereby inhibiting the Pt agglomeration in Pt/C catalyst. Besides, the Pt/GO/8 wt.% CeO_2 nanocomposite in a PEMFC reached a catalytic activity retention of 69% after 5000 cycles at a high voltage range of 0.8–1.23 V. The CeO_2 nanoparticles, due to its free radical scavenging activity, further alleviated the decay of Pt catalysts, resulting in the excellent cyclic life of the nanocomposite catalyst.[252] Additionally, when GO was intercalated into the protonated layered MnO_2, the improved electrocatalytic activity towards oxygen reduction reactions in alkaline media was observed.[253] The intercalation of GO decreased the interlayer distance as well as enhanced the amount of accessible Mn^{3+}/Mn^{4+} redox sites, both of which resulted in a great enhancement of the electrocatalytic activity.

Furthermore, as the Fermi level of GO is above the reduction potentials of most noble metal ions, GO can be used as the electron donors for reducing noble metal ions without adding any additional reductants and surfactants, leading to the growth of the metal nanoparticles on the GO surfaces with excellent monodispersity, uniformity and purity.[254–259] The noble metals with ultrafine sizes, possessing increased surface area and the number of edge and corner atoms, are found to be able to express a superior electrocatalytic ability in the fuel cells.[254] For example, gold nanoparticles monodispersed on GO nanosheets were successfully synthesised by the redox reaction between $AuCl_4^{2-}$ and GO, which exhibited a high electrocatalytic activity and a dominant four-electron pathway toward oxygen reduction reaction.[257] The spontaneous electron transfer from the GO to the $AuCl_4^{2-}$ is due to their relative potential levels. The Fermi level of the GO is +0.24 V vs. standard hydrogen electrode (SHE), which is well above the reduction potential of $AuCl_4^{2-}$ (+1.002 V vs. SHE). Likewise, bimetallic Pd-Pt alloy nanoparticles on GO with an excellent electrocatalytic activity can also be prepared by adding CO as a reducing agent in $PdCl_4^{2-}$ and $PtCl_6^{2-}$ mixing solutions.[256] More interestingly, a 3D GO/carbon sphere supported silver composite was produced using GO as the reductant, which presented a significantly improved activity towards the oxygen reduction reaction in alkaline media.[258] The 3D architecture was advantageous, as it not only increased the electrical conductivity but also enforced the mass transport in the catalyst layer that facilitated the reactants access to the active sites. Besides, the Au, Fe-Au and Ag-Au nanoparticles, synthesised on the GO surfaces, were investigated regarding their electrocatalytic activities for methanol oxidation.[259] The oxidation peak current densities for GO-supported Au, Fe-Au and Ag-Au were approximately 1.21, 8.75 and 14.79 mA cm^{-2}, respectively. And the pure GO delivered a peak current density of around 0.61 mA cm^{-2}, which indicated that the GO also played an important role to catalyse methanol.

Nevertheless, the high cost of the noble metal catalysts is a major barrier for the commercialisation of fuel cells.[260] Thus efforts have been made to develop highly active, durable and cost-effective non-metal catalysts. Electrically conductive $\pi-$conjugated polymers have attracted interest as an acceptable candidate in terms of their low cost and high performance. The embedding of GO into the polymer matrix can increase its conductivity and reduce biofouling of the matrix for catalytic

applications.[260] The GO/polymer composite can be formed through hydrogen bonding and a ring-opening reaction of the epoxide groups with the amine to form a new C–N bond. Such C–N bonds and the sulphur atoms in the polymer backbone play a function of the active sites for the electrocatalytic reduction of O_2 to H_2O. Moreover, nitrogen-doped carbon is considered as one of the promising alternatives to Pt.[261] S and N co-doped GO was prepared by a conventional chemical vapour deposition method using pyrimidine and thiophene as precursors for the application of the oxygen reduction reaction.[262] Thanks to a synergetic effect of N and S co-doping, the dual-doped GO exhibited a competitive catalytic activity (10.0 mA cm^{-2} kinetic-limiting current density at -0.25 V) and an efficient four-electron-dominant process for oxygen reduction reaction.

2.4.4.2 Contributions in membranes

As GO exhibits a high proton conduction, which is mainly ascribed to the epoxide groups that act as the site for proton transfer after water molecules bind to them, GO can be applied as a proton electrolyte membrane in various fuel cells (Figure 21a).[263–265] It is demonstrated that GO possesses a slightly higher water uptake, which possibly results in a better water retention for high temperature operation, and higher tensile strength and elastic modulus than Nafion.[264] Its proton conductivity increases with increasing humidity under all temperature conditions. But when the temperature is over 70°C, the conductivity decreases, which is probably due to partial reduction of the proton-conducting oxygen groups. The free-standing GO membrane, synthesised through a vacuum filtration method, in a PEMFC presented a maximum power density of ~34 mW cm^{-2} within the temperature range of 30$-$80°C, which was close to that of a Nafion electrolyte based fuel cell under the similar conditions.[264] Furthermore, functionalised GO sheets, such as ozonated GO and sulfonic acid treated GO, show an enhanced proton conductivity owing to the higher quantity of oxygenated functional groups on the GO sheets, which thus significantly improve the performance of the fuel cells.[266–268]

Nafion as a common ionomer membrane has been extensively used in PEMFCs. However, it has two main drawbacks, including low water retention capacity at temperatures above 80°C and inability to operate under low humidity for extended

periods.[269] Recently, Nafion/GO composite membranes are investigated in order to improve the physical and chemical properties of the Nafion membrane.[269–273] The addition of GO into the Nafion membrane can lead to further enhancement in power density of the fuel cells, which is because GO can retain more water within the membrane to increase the proton conductivity.[271] It was reported that the porous rolled-up GO sheets, produced by simply evaporating their dispersion, were able to act as an excellent supporting material to interact with the Nafion matrix, significantly facilitating the proton transfer. Besides, 10 wt% sulfonated GO/Nafion membrane in a PEMFC was found to display a higher power density of 150 mW cm^{-2} than the pure Nafion membrane (42 mW cm^{-2}).[273] Moreover, the GO or functionalised GO/Nafion composite membranes can also be used in DMFCs, which greatly decrease the methanol permeability while maintaining ionic conductivity.[274–279] In particular, the exfoliated and orderly GO sheets show an effective reduction of the diffusion of methanol, which is attributed to an increase in the tortuosity pathway, as shown in Figure 21b.[276–279] The highly ordered delaminated sulfonated GO with Nafion membrane showed a power density of ~120 mW cm^{-2} at 90°C.[278]
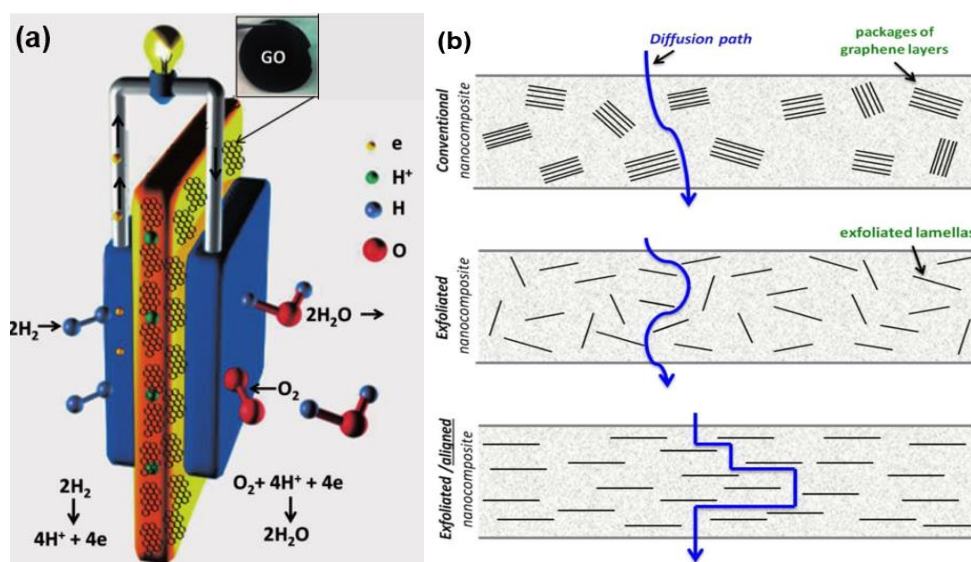

Figure 21. (a) A typical GO membrane based proton exchange membrane fuel cell (PEMFC)[266]; (b) The proposed diffusion pathways of methanol molecules through a conventional, exfoliated and exfoliated/aligned nanocomposite membrane, respectively[278].

As the Nafion is an expensive material, the embedding of GO or functionalised GO into other polymers as the proton exchange membranes is also studied and exhibits a competitive performance in the fuel cells.[280–291] For instance, poly (ethylene oxide) (PEO) cross-linked GO membrance with the enhanced chemical, thermal, and mechanical stabilities showed a maximum power density of 53 mW cm^{-2} at the operation temperature of 60°C in a PEMFC.[283] The sulfonated GO/SPEEK composite membrane in PEMFC possessed a power density of 378 mW cm^{-2} at 80°C with a 30% relative humidity.[289] The SPEEK/poly(vinyl alcohol) (PVA)/sulfonated GO/Fe_3O_4 nanocomposite membrane in a DMFC with a low methanol permeability, excellent tensile strength and superior proton conductivity presented a high power density of 122.7 mW cm^{-2} at 80°C.[281] The introduction of GO into the membranes not only increases the ion-exchange capacity, water uptake, proton conductivity and mechanical properties in PEMFCs and DMFCs, but also reduces the methanol permeability and improves the selectivity of the membrane in DMFCs.[284,286] Importantly, the size of GO sheets is found to have an effect on the performance of the fuel cells.[292] The smallest sized GO combined with the polymer showed the best performance. This is because GO sheets with the smallest size have a stronger hydrogen bonding interaction with the polymer matrix, thus promoting the formation of the well-defined microstructure and well-connected proton transport pathways.

2.5 Summary

While GO and related materials have been known for more than 150 years, they remain the primary foci of many fundamental and applied studies. GO as a 2D soft molecule with amphiphilic nature is characterised by plentiful self-concentrating phenomena at interfaces, and these interfacial properties together with the developed self-assembly techniques provide simple and effective strategies for producing a variety of novel carbon nanostructures and materials with designed functions.[1] With respect to electrochemical properties and applications, the main advantages of GO over other kinds of carbon-based materials include its facile synthesis, substantial solubility and processability, adjustable moderate conductivity, high surface area, excellent biocompatibility, and abundance of inexpensive source material.[56] Owing to these advantageous structural and physicochemical properties, GO-based materials have been used to design and prepare GO-based electrodes, solid electrolytes and

dielectric materials for a wide range of applications in electrochemical field. To date, considerable advances in this area have already been made.

Nonetheless, research toward the wider application of GO-based materials in electrochemistry is still in its infancy. Much work remains to be done in facilitating the practical applications of GO-based materials and broadening the scope of their electrochemical applications. Therefore, as GO-based materials offer many advantages for promising electrochemical applications, oxidised CNTs that have the same oxygen functional groups as the GO will be used as the electrodes in this project to construct different kinds of supercapacitors. This can not only further understand the potential of GO-based materials in energy storage but also widen their electrochemical applications.

2.6 References

[1]   Shao J-J, Lv W, Yang Q-H. Self-Assembly of Graphene Oxide at Interfaces. Adv Mater 2014.

[2]   Dreyer DR, Park S, Bielawski CW, Ruoff RS. The chemistry of graphene oxide. Chem Soc Rev 2010;39:228–40.

[3]   Chen D, Feng H, Li J. Graphene oxide: preparation, functionalization, and electrochemical applications. Chem Rev 2012;112:6027–53.

[4]   Szabó T, Berkesi O, Forgó P. Evolution of surface functional groups in a series of progressively oxidized graphite oxides. Chem Mater 2006;18:2740–9.

[5]   Sun H, Yang Y, Huang Q. Preparation and Structural Variation of Graphite Oxide and Graphene Oxide. Integr Ferroelectr 2011;128:163–70.

[6]   Lu N, Yin D, Li Z, Yang J. Structure of Graphene Oxide: Thermodynamics versus Kinetics. J Phys Chem C 2011;115:11991–5.

[7]   Andre Mkhoyan K, Contryman AW, Silcox J, Stewart D a, Eda G, Mattevi C, et al. Atomic and electronic structure of graphene-oxide. Nano Lett 2009;9:1058–63.

[8]   Kim J, Cote LJ, Kim F, Yuan W, Shull KR, Huang J. Graphene oxide sheets at interfaces. J Am Chem Soc 2010;132:8180–6.

[9]   Cote LJ, Kim J, Tung VC, Luo J, Kim F, Huang J. Graphene oxide as surfactant sheets. Pure Appl Chem 2010;83:95–110.

[10] Paredes JI, Villar-Rodil S, Martínez-Alonso a, Tascón JMD. Graphene oxide dispersions in organic solvents. Langmuir 2008;24:10560–4.

[11] Stankovich S, Piner RD, Nguyen ST, Ruoff RS. Synthesis and exfoliation of isocyanate-treated graphene oxide nanoplatelets. Carbon N Y 2006;44:3342–7.

[12] Wang G, Wang B, Park J, Yang J, Shen X, Yao J. Synthesis of enhanced hydrophilic and hydrophobic graphene oxide nanosheets by a solvothermal method. Carbon N Y 2009;47:68–72.

[13] Stankovich S, Piner RD, Chen X, Wu N, Nguyen ST, Ruoff RS. Stable aqueous dispersions of graphitic nanoplatelets via the reduction of exfoliated graphite oxide in the presence of poly(sodium 4-styrenesulfonate). J Mater Chem 2006;16:155.

[14] Dimiev A, Kosynkin D V, Alemany LB, Chaguine P, Tour JM. Pristine graphite oxide. J Am Chem Soc 2012;134:2815–22.

[15] Erickson K, Erni R, Lee Z, Alem N, Gannett W, Zettl A. Determination of the local chemical structure of graphene oxide and reduced graphene oxide. Adv Mater 2010;22:4467–72.

[16] Lerf A, He H, Forster M, Klinowski J. Structure of Graphite Oxide Revisited. J Phys Chem B 1998;102:4477–82.

[17] Nakajima T, Matsuo Y. Formation process and structure of graphite oxide. Carbon N Y 1994;32:469–75.

[18] Schniepp HC, Li J-L, McAllister MJ, Sai H, Herrera-Alonso M, Adamson DH, et al. Functionalized single graphene sheets derived from splitting graphite oxide. J Phys Chem B 2006;110:8535–9.

[19] Cai W, Piner RD, Stadermann FJ, Park S, Shaibat M a, Ishii Y, et al. Synthesis and solid-state NMR structural characterization of 13C-labeled graphite oxide. Science 2008;321:1815–7.

[20] Kim F, Cote LJ, Huang J. Graphene oxide: surface activity and two-dimensional assembly. Adv Mater 2010;22:1954–8.

[21] Chao Xu, Xiaodong Wu, Junwu Zhu XW. Synthesis of amphiphilic graphite oxide. Carbon N Y 2008;46:386–9.

[22] Kim JE, Han TH, Lee SH, Kim JY, Ahn CW, Yun JM, et al. Graphene oxide liquid crystals. Angew Chem Int Ed Engl 2011;50:3043–7.

[23] Pretula J, Kaluzynski K, Wisniewski B, Szymanski R, Loontjens T, Penczek S. Growing Poly(N-vinylcarbazole) from the Surface of Graphene Oxide via RAFT Polymerization. J Polym Sci Part a-Polymer Chem 2008;46:830–43.

[24] Hou S, Su S, Kasner ML, Shah P, Patel K, Madarang CJ. Formation of highly stable dispersions of silane-functionalized reduced graphene oxide. Chem Phys Lett 2010;501:68–74.

[25] Bai H, Li C, Wang X, Shi G. A pH-sensitive graphene oxide composite hydrogel. Chem Commun (Camb) 2010;46:2376–8.

[26] Lv W, You CH, Wu S, Li B, Zhu ZP, Wang M, et al. PH-Mediated fine-tuning of optical properties of graphene oxide membranes. Carbon N Y 2012;50:3233–9.

[27] Fan X, Peng W, Li Y, Li X, Wang S, Zhang G, et al. Deoxygenation of exfoliated graphite oxide under alkaline conditions: a green route to graphene preparation. Adv Mater 2008;20:4490–3.

[28] Cote LJ, Kim J, Zhang Z, Sun C, Huang J. Tunable assembly of graphene oxide surfactant sheets: wrinkles, overlaps and impacts on thin film properties. Soft Matter 2010;6:6096.

[29] Wang S, Chia PJ, Chua LL, Zhao LH, Png RQ, Sivaramakrishnan S, et al. Band-like transport in surface-functionalized highly solution-processable graphene nanosheets. Adv Mater 2008;20:3440–6.

[30] Park S, Dikin D a., Nguyen ST, Ruoff RS. Graphene oxide sheets chemically cross-linked by polyallylamine. J Phys Chem C 2009;113:15801–4.

[31] Lu CH, Yang HH, Zhu CL, Chen X, Chen GN. A graphene platform for sensing biomolecules. Angew Chemie - Int Ed 2009;48:4785–7.

[32] Eigler S, Grimm S, Hirsch A. Investigation of the thermal stability of the carbon framework of graphene oxide. Chemistry 2014;20:984–9.

[33] Jeong H-K, Lee YP, Jin MH, Kim ES, Bae JJ, Lee YH. Thermal stability of graphite oxide. Chem Phys Lett 2009;470:255–8.

[34] Acik M, Mattevi C, Gong C, Lee G, Cho K, Chhowalla M, et al. The role of intercalated water in multilayered graphene oxide. ACS Nano 2010;4:5861–8.

[35] Eigler S, Grimm S, Hof F, Hirsch A. Graphene oxide: a stable carbon framework for functionalization. J Mater Chem A 2013;1:11559.

[36] Eigler S, Dotzer C, Hirsch A. Formation and decomposition of CO2 intercalated

graphene oxide. Chem Mater 2012;24:1276–82.

[37]   Song J, Wang X, Chang C-T. Preparation and Characterization of Graphene Oxide. J Nanomater 2014;2014:1–6.

[38]   Zhou S, Bongiorno A. Origin of the chemical and kinetic stability of graphene oxide. Sci Rep 2013;3:2484.

[39]   Kumar P V, Bardhan NM, Tongay S, Wu J, Belcher AM, Grossman JC. Scalable enhancement of graphene oxide properties by thermally driven phase transformation. Nat Chem 2014;6:151–8.

[40]   Kim S, Zhou S, Hu Y, Acik M, Chabal YJ, Berger C, et al. Room-temperature metastability of multilayer graphene oxide films. Nat Mater 2012;11:544–9.

[41]   Krishnan D, Kim F, Luo J, Cruz-Silva R, Cote LJ, Jang HD, et al. Energetic graphene oxide: Challenges and opportunities. Nano Today 2012;7:137–52.

[42]   Mu X, Wu X, Zhang T, Go DB, Luo T. Thermal transport in graphene oxide--from ballistic extreme to amorphous limit. Sci Rep 2014;4:3909.

[43]   Pacilé D, Meyer JC, Fraile Rodríguez a., Papagno M, Gómez-Navarro C, Sundaram RS, et al. Electronic properties and atomic structure of graphene oxide membranes. Carbon N Y 2011;49:966–72.

[44]   Becerril H a., Mao J, Liu Z, Stoltenberg RM, Bao Z, Chen Y. Evaluation of solution-processed reduced graphene oxide films as transparent conductors. ACS Nano 2008;2:463–70.

[45]   Eda G, Chhowalla M. Chemically derived graphene oxide: towards large-area thin-film electronics and optoelectronics. Adv Mater 2010;22:2392–415.

[46]   Jin M, Jeong H-K, Yu WJ, Bae DJ, Kang BR, Lee YH. Graphene oxide thin film field effect transistors without reduction. J Phys D Appl Phys 2009;42:135109.

[47]   Kulkarni DD, Kim S, Chyasnavichyus M, Hu K, Fedorov AG, Tsukruk V V. Chemical reduction of individual graphene oxide sheets as revealed by electrostatic force microscopy. J Am Chem Soc 2014;136:6546–9.

[48]   Chua CK, Pumera M. Chemical reduction of graphene oxide: a synthetic chemistry viewpoint. Chem Soc Rev 2014;43:291–312.

[49]   Mcallister MJ, Li J, Adamson DH, Schniepp HC, Abdala A a, Liu J, et al. Single Sheet Functionalized Graphene by Oxidation and Thermal Expansion of Graphite. Society 2007;19:4396–404.

[50] Zhu Y, Stoller MD, Cai W, Velamakanni A, Piner RD, Chen D, et al. Exfoliation of graphite oxide in propylene carbonate and thermal reduction of the resulting graphene oxide platelets. ACS Nano, vol. 4, 2010, p. 1227–33.

[51] Jung I, Dikin D a., Piner RD, Ruoff RS. Tunable electrical conductivity of individual graphene oxide sheets reduced at "Low" temperatures. Nano Lett 2008;8:4283–7.

[52] Stankovich S, Dikin D a., Piner RD, Kohlhaas K a., Kleinhammes A, Jia Y, et al. Synthesis of graphene-based nanosheets via chemical reduction of exfoliated graphite oxide. Carbon N Y 2007;45:1558–65.

[53] Chien CT, Li SS, Lai WJ, Yeh YC, Chen HA, Chen IS, et al. Tunable photoluminescence from graphene oxide. Angew Chemie - Int Ed 2012;51:6662–6.

[54] Maiti R, Midya a, Narayana C, Ray SK. Tunable optical properties of graphene oxide by tailoring the oxygen functionalities using infrared irradiation. Nanotechnology 2014;25:495704.

[55] Liu L, Zhang J, Zhao J, Liu F. Mechanical properties of graphene oxides. Nanoscale 2012;4:5910–6.

[56] Dreyer DR, Todd AD, Bielawski CW. Harnessing the chemistry of graphene oxide. Chem Soc Rev 2014;43:5288–301.

[57] Medhekar N V, Ramasubramaniam A, Ruoff RS, Shenoy VB. Hydrogen bond networks in graphene oxide composite paper: structure and mechanical properties. ACS Nano 2010;4:2300–6.

[58] Suk JW, Piner RD, An J, Ruoff RS. Mechanical properties of monolayer graphene oxide. ACS Nano 2010;4:6557–64.

[59] Dikin D a, Stankovich S, Zimney EJ, Piner RD, Dommett GHB, Evmenenko G, et al. Preparation and characterization of graphene oxide paper. Nature 2007;448:457–60.

[60] Park S, Lee K-S, Bozoklu G, Cai W, Nguyen ST, Ruoff RS. Graphene oxide papers modified by divalent ions-enhancing mechanical properties via chemical cross-linking. ACS Nano 2008;2:572–8.

[61] Zaman I, Kuan HC, Meng Q, Michelmore A, Kawashima N, Pitt T, et al. A facile approach to chemically modified graphene and its polymer nanocomposites. Adv

Funct Mater 2012;22:2735–43.

[62] Compton OC, Cranford SW, Putz KW, An Z, Brinson LC, Buehler MJ, et al. Tuning the mechanical properties of graphene oxide paper and its associated polymer nanocomposites by controlling cooperative intersheet hydrogen bonding. ACS Nano 2012;6:2008–19.

[63] Wu Z-S, Zhou G, Yin L-C, Ren W, Li F, Cheng H-M. Graphene/metal oxide composite electrode materials for energy storage. Nano Energy 2012;1:107–31.

[64] Raccichini R, Varzi A, Passerini S, Scrosati B. The role of graphene for electrochemical energy storage. Nat Mater 2015;14:271–9.

[65] Brodie BC. On the Atomic Weight of Graphite. Philos Trans R Soc London 1859;149:249–59.

[66] Staudenmaier L. Procedure for the preparation of graphitic acid. Ber Dtsch Chem Ges 1899;32:1394–9.

[67] Poh HL, Šaněk F, Ambrosi A, Zhao G, Sofer Z, Pumera M. Graphenes prepared by Staudenmaier, Hofmann and Hummers methods with consequent thermal exfoliation exhibit very different electrochemical properties. Nanoscale 2012;4:3515–22.

[68] Hummer WSJ, Offeman RE. Preparation of Graphitic Oxide. J Am Chem Soc 1958;80:1339.

[69] Wu T-T, Ting J-M. Preparation and characteristics of graphene oxide and its thin films. Surf Coatings Technol 2013;231:487–91.

[70] Compton OC, Nguyen ST. Graphene oxide, highly reduced graphene oxide, and graphene: versatile building blocks for carbon-based materials. Small 2010;6:711–23.

[71] Chen J, Yao B, Li C, Shi G. An improved Hummers method for eco-friendly synthesis of graphene oxide. Carbon N Y 2013;64:225–9.

[72] Marcano DC, Kosynkin D V, Berlin JM, Sinitskii A, Sun Z, Slesarev A, et al. Improved synthesis of graphene oxide. ACS Nano 2010;4:4806–14.

[73] Lu J, Yang J, Wang J, Lim A, Wang S, Loh KP. One-Pot Synthesis of Fluorescent Carbon Graphene by the Exfoliation of Graphite in Ionic Liquids. ACS Nano 2009;3:2367–75.

[74] Stankovich S, Dikin D a, Dommett GHB, Kohlhaas KM, Zimney EJ, Stach E a, et

al. Graphene-based composite materials. Nature 2006;442:282–6.

[75] Cai D, Song M. Preparation of fully exfoliated graphite oxide nanoplatelets in organic solvents. J Mater Chem 2007;17:3678.

[76] Park S, An J, Jung I, Piner RD, An SJ, Li X, et al. Colloidal suspensions of highly reduced graphene oxide in a wide variety of organic solvents. Nano Lett 2009;9:1593–7.

[77] Zhang L, Liang J, Huang Y, Ma Y, Wang Y, Chen Y. Size-controlled synthesis of graphene oxide sheets on a large scale using chemical exfoliation. Carbon N Y 2009;47:3365–8.

[78] Kosynkin D V, Higginbotham AL, Sinitskii A, Lomeda JR, Dimiev A, Price BK, et al. Longitudinal unzipping of carbon nanotubes to form graphene nanoribbons. Nature 2009;458:872–6.

[79] Zuo P-P, Feng H-F, Xu Z-Z, Zhang L-F, Zhang Y-L, Xia W, et al. Fabrication of biocompatible and mechanically reinforced graphene oxide-chitosan nanocomposite films. Chem Cent J 2013;7:39.

[80] Bornside DE, Macosko CW, Scriven LE. Spin coating: One-dimensional model. J Appl Phys 1989;66:5185.

[81] Scriven L. Physics and applications of dip coating and spin coating. MRS Proc 1988;121:717–29.

[82] Bardecker J a, Afzali A, Tulevski GS, Graham T, Hannon JB, Jen AK-Y. Directed assembly of single-walled carbon nanotubes via drop-casting onto a UV-patterned photosensitive monolayer. J Am Chem Soc 2008;130:7226–7.

[83] Pham VH, Cuong TV, Hur SH, Shin EW, Kim JS, Chung JS, et al. Fast and simple fabrication of a large transparent chemically-converted graphene film by spray-coating. Carbon N Y 2010;48:1945–51.

[84] Zou J, Kim F. Diffusion driven layer-by-layer assembly of graphene oxide nanosheets into porous three-dimensional macrostructures. Nat Commun 2014;5:5254.

[85] Putz KW, Compton OC, Segar C, An Z, Nguyen ST, Brinson LC. Evolution of order during vacuum-assisted self-assembly of graphene oxide paper and associated polymer nanocomposites. ACS Nano 2011;5:6601–9.

[86] Shao J-J, Wu S-D, Zhang S-B, Lv W, Su F-Y, Yang Q-H. Graphene oxide

hydrogel at solid/liquid interface. Chem Commun (Camb) 2011;47:5771–3.

[87]   An SJ, Zhu Y, Lee SH, Stoller MD, Emilsson T, Park S, et al. Thin film fabrication and simultaneous anodic reduction of deposited graphene oxide platelets by electrophoretic deposition. J Phys Chem Lett 2010;1:1259–63.

[88]   Qiu L, Liu JZ, Chang SLY, Wu Y, Li D. Biomimetic superelastic graphene-based cellular monoliths. Nat Commun 2012;3:1241.

[89]   Gudarzi MM, Sharif F. Self assembly of graphene oxide at the liquid–liquid interface: A new route to the fabrication of graphene based composites. Soft Matter 2011;7:3432.

[90]   Chen F, Liu S, Shen J, Wei L, Liu A, Chan-Park MB, et al. Ethanol-assisted graphene oxide-based thin film formation at pentane-water interface. Langmuir 2011;27:9174–81.

[91]   Guo P, Song H, Chen X. Hollow graphene oxide spheres self-assembled by W/O emulsion. J Mater Chem 2010;20:4867.

[92]   Lee SH, Kim HW, Hwang JO, Lee WJ, Kwon J, Bielawski CW, et al. Three-Dimensional Self-Assembly of Graphene Oxide Platelets into Mechanically Flexible Macroporous Carbon Films. Angew Chemie 2010;122:10282–6.

[93]   Chen C, Yang Q-H, Yang Y, Lv W, Wen Y, Hou P-X, et al. Self-Assembled Free-Standing Graphite Oxide Membrane. Adv Mater 2009;21:3007–11.

[94]   Shao J-J, Lv W, Guo Q, Zhang C, Xu Q, Yang Q-H, et al. Hybridization of graphene oxide and carbon nanotubes at the liquid/air interface. Chem Commun (Camb) 2012;48:3706–8.

[95]   Luo J, Jang HD, Sun T, Xiao L, He Z, Katsoulidis AP, et al. Compression and aggregation-resistant particles of crumpled soft sheets. ACS Nano 2011;5:8943–9.

[96]   Cote LJ, Kim F, Huang J. Langmuir-Blodgett assembly of graphite oxide single layers. J Am Chem Soc 2009;131:1043–9.

[97]   Zheng Q, Zhang B, Lin X, Shen X, Yousefi N, Huang Z-D, et al. Highly transparent and conducting ultralarge graphene oxide/single-walled carbon nanotube hybrid films produced by Langmuir–Blodgett assembly. J Mater Chem 2012;22:25072.

[98]   Lee SW, Yabuuchi N, Gallant BM, Chen S, Kim B-S, Hammond PT, et al. High-

power lithium batteries from functionalized carbon-nanotube electrodes. Nat Nanotechnol 2010;5:531–7.

[99] Armand M. Issues and challenges facing rechargeable lithium batteries. Nature 2001;414:359–67.

[100] Kiani M a., Mousavi MF, Rahmanifar MS. Challenges in the development of advanced Li-ion batteries: a review. Int J Electrochem Sci 2011;6:2581–95.

[101] Song Z, Zhou H. Towards sustainable and versatile energy storage devices: an overview of organic electrode materials. Energy Environ Sci 2013;6:2280.

[102] Xu B, Qian D, Wang Z, Meng YS. Recent progress in cathode materials research for advanced lithium ion batteries. Mater Sci Eng R Reports 2012;73:51–65.

[103] Scrosati B, Sapienza L, Moro PA. Recent advances in lithium ion battery materials. Electrochim Acta 2000;45:2461–6.

[104] Ke Wang, Yonggang Wang, Congxiao Wang YX. Graphene oxide assisted Solvothermal synthesis of LiMnPO 4 naonparticles for lithium ion batteries cathode. Electrochim Acta 2013;146:8–14.

[105] Ai W, Du Z, Fan Z, Jiang J, Wang Y, Zhang H, et al. Chemically engineered graphene oxide as high performance cathode materials for Li-ion batteries. Carbon N Y 2014;76:148–54.

[106] Xu C, Li L, Qiu F, An C, Xu Y, Wang Y, et al. Graphene oxide assisted facile hydrothermal synthesis of LiMn0.6Fe0.4PO4 nanoparticles as cathode material for lithium ion battery. J Energy Chem 2014;23:397–402.

[107] Xu J, Zhaolong Li, Zhang X, Huang S, Jian S, Zhu Q, et al. Self-assembled V3O7/graphene oxide nanocomposites as cathode material for lithium-ion batteries. Int J Nanotechnol 2014;11:808–18.

[108] Reddy Channu VS, Ravichandran D, Rambabu B, Holze R. Carbon and functionalized graphene oxide coated vanadium oxide electrodes for lithium ion batteries. Appl Surf Sci 2014;305:596–602.

[109] Yu F, Zhang L, Lai L, Zhu M, Guo Y, Xia L, et al. High Electrochemical Performance of LiFePO4 Cathode Material via In-Situ Microwave Exfoliated Graphene Oxide. Electrochim Acta 2015;151:240–8.

[110] Stournara ME, Shenoy VB. Enhanced Li capacity at high lithiation potentials in

graphene oxide. J Power Sources 2011;196:5697–703.

[111] Wang D-W, Sun C, Zhou G, Li F, Wen L, Donose BC, et al. The examination of graphene oxide for rechargeable lithium storage as a novel cathode material. J Mater Chem A 2013;1:3607.

[112] Channu VS, Bobba R, Holze R. Graphite and graphene oxide electrodes for lithium ion batteries. Colloids Surfaces A Physicochem … 2013;436:245–51.

[113] Petnikota S, Marka SK, Banerjee A, Reddy MV, Srikanth VVSS, Chowdari BVR. Graphenothermal reduction synthesis of "exfoliated graphene oxide/iron (II) oxide" composite for anode application in lithium ion batteries. J Power Sources 2015;293:253–63.

[114] Feng F, Kang W, Yu F, Zhang H, Shen Q. High-rate lithium storage capability of cupric-cobaltous oxalate induced by unavoidable crystal water and functionalized graphene oxide. J Power Sources 2015;282:109–17.

[115] Xie Z, Li X, Li W, Chen M, Qu M. Graphene oxide / lithium titanate composite with binder-free as high capacity anode material for lithium-ion batteries. J Power Sources 2015;273:754–60.

[116] Zhu YG, Wang Y, Xie J, Cao G-S, Zhu T-J, Zhao X, et al. Effects of Graphene Oxide Function Groups on SnO2/Graphene Nanocomposites for Lithium Storage Application. Electrochim Acta 2015;154:338–44.

[117] Song H, Li N, Wang C. Enhanced capability and cyclability of SnO2–graphene oxide hybrid anode by firmly anchored SnO2 quantum dots. J Mater Chem A 2013;1:7558–62.

[118] Information S, Bhaskar A, Deepa M, Ramakrishna M, Rao TN. Poly (3 , 4-ethylenedioxythiophene) Sheath Over a SnO 2 Hollow Spheres / Graphene Oxide Hybrid for a Durable Anode in Li-Ion Batteries. J Phys Chem C 2014;118:7296–306.

[119] Zhang J, Cai Y, Wu J, Yao J. Graphene oxide-confined synthesis of Li4Ti5O12 microspheres as high-performance anodes for lithium ion batteries. Electrochim Acta 2015;165:422–9.

[120] Yunwei Shi, Dongyun Zhang, Chengkang Chang KH, Holze R. Enhanced electrochemical performance of oxygen-deficient Li4Ti5O12−x anode material induced by graphene oxide. J Alloys Compd 2015;639:274–9.

[121] Meng X, Xu Y, Sun X, Wang J, Xiong L, Du X, et al. Graphene oxide sheets-induced growth of nanostructured Fe_3O_4 for a high-performance anode material of lithium ion batteries. J Mater Chem A 2015;3:12938–46.

[122] Xu Y-T, Guo Y, Li C, Zhou X-Y, Tucker MC, Fu X-Z, et al. Graphene oxide nano-sheets wrapped Cu2O microspheres as improved performance anode materials for lithium ion batteries. Nano Energy 2015;11:38–47.

[123] Xu Y-T, Guo Y, Jiang H, Xie X-B, Zhao B, Zhu P-L, et al. Enhanced Performance of Lithium-Ion Batteries with Copper Oxide Microspheres @ Graphene Oxide Micro/Nanocomposite Electrodes. Energy Technol 2015;3:488–95.

[124] Qu Q, Gao T, Zheng H, Li X, Liu H, Shen M, et al. Graphene oxides-guided growth of ultrafine Co3O4 nanocrystallites from MOFs as high-performance anode of Li-ion batteries. Carbon N Y 2015;92:119–25.

[125] Ye Y, Wang P, Sun H, Tian Z, Liu J, Liang C. Structural and electrochemical evaluation of a TiO_2 –graphene oxide based sandwich structure for lithium-ion battery anodes. RSC Adv 2015;5:45038–43.

[126] Fang C, Deng Y, Xie Y, Su J, Chen G. Improving the Electrochemical Performance of Si Nanoparticle Anode Material by Synergistic Strategies of Polydopamine and Graphene Oxide Coatings. J Phys Chem C 2015;119:1720–8.

[127] Zhang J, Xie Z, Li W, Dong S, Qu M. High-capacity graphene oxide/graphite/carbon nanotube composites for use in Li-ion battery anodes. Carbon N Y 2014;74:153–62.

[128] Zhang J, Cao H, Tang X, Fan W, Peng G, Qu M. Graphite/graphene oxide composite as high capacity and binder-free anode material for lithium ion batteries. J Power Sources 2013;241:619–26.

[129] Richard Prabakar SJ, Hwang YH, Bae EG, Lee DK, Pyo M. Graphene oxide as a corrosion inhibitor for the aluminum current collector in lithium ion batteries. Carbon N Y 2013;52:128–36.

[130] Gao S, Zhong J, Xue G, Wang B. Ion conductivity improved polyethylene oxide/lithium perchlorate electrolyte membranes modified by graphene oxide. J Memb Sci 2014;470:316–22.

[131] Cheng S, Smith DM, Li CY. Anisotropic Ion Transport in a Poly(ethylene oxide)–LiClO 4 Solid State Electrolyte Templated by Graphene Oxide. Macromolecules

2015;48:4503–10.

[132] Shim J, Kim D-G, Kim HJ, Lee JH, Baik J-H, Lee J-C. Novel composite polymer electrolytes containing poly(ethylene glycol)-grafted graphene oxide for all-solid-state lithium-ion battery applications. J Mater Chem A Mater Energy Sustain 2014;2:13873–83.

[133] Manthiram A, Fu Y, Su Y-S. Challenges and Prospects of Lithium-Sulfur Batteries. Acc Chem Res 2013;46:1125–34.

[134] Shin ES, Kim K, Oh SH, Cho W II. Polysulfide dissolution control: the common ion effect. Chem Commun (Camb) 2013;49:2004–6.

[135] Wu H, Huang Y, Zong M, Ding X, Ding J, Sun X. Electrostatic self-assembly of graphene oxide wrapped sulfur particles for lithium–sulfur batteries. Mater Res Bull 2015;64:12–6.

[136] Rong J, Ge M, Fang X, Zhou C. Solution ionic strength engineering as a generic strategy to coat graphene oxide (GO) on various functional particles and its application in high-performance lithium-sulfur (Li-S) batteries. Nano Lett 2014;14:473–9.

[137] Xiao M, Huang M, Zeng S, Han D, Wang S, Sun L, et al. Sulfur@graphene oxide core–shell particles as a rechargeable lithium–sulfur battery cathode material with high cycling stability and capacity. RSC Adv 2013;3:4914.

[138] Cells LS, Ji L, Rao M, Zheng H, Zhang L, Li OY, et al. Graphene Oxide as a Sulfur Immobilizer in High Performance Lithium/Surfur cells. J Am Chem Soc 2011;133:18522–5.

[139] Zhang L, Ji L, Glans P-A, Zhang Y, Zhu J, Guo J. Electronic structure and chemical bonding of a graphene oxide–sulfur nanocomposite for use in superior performance lithium–sulfur cells. Phys Chem Chem Phys 2012;14:13670.

[140] Feng X, Song M-K, Stolte WC, Gardenghi D, Zhang D, Sun X, et al. Understanding the degradation mechanism of rechargeable lithium/sulfur cells: a comprehensive study of the sulfur-graphene oxide cathode after discharge-charge cycling. Phys Chem Chem Phys 2014.

[141] Bao W, Zhang Z, Chen W, Zhou C, Lai Y, Li J. Facile synthesis of graphene oxide @ mesoporous carbon hybrid nanocomposites for lithium sulfur battery. Electrochim Acta 2014;127:342–8.

[142] Liu S, Xie K, Li Y, Chen Z, Hong X, Zhou L, et al. Graphene oxide wrapped hierarchical porous carbon–sulfur composite cathode with enhanced cycling and rate performance for lithium sulfur batteries. RSC Adv 2015;5:5516–22.

[143] Zhou W, Chen H, Yu Y, Wang D, Cui Z, Disalvo FJ, et al. Amylopectin Wrapped Graphene Oxide / Sulfur for Improved Cyclability of Lithium A Sulfur Battery. ACS Nano 2013;7:8801–8.

[144] Moon S, Jung YH, Kim DK. Enhanced electrochemical performance of a crosslinked polyaniline-coated graphene oxide-sulfur composite for rechargeable lithium–sulfur batteries. J Power Sources 2015;294:386–92.

[145] Zhang J, Yang N, Yang X, Li S, Yao J, Cai Y. Hollow sulfur@graphene oxide core–shell composite for high-performance Li–S batteries. J Alloys Compd 2015;650:604–9.

[146] Sun C, Shi L, Fan C, Fu X, Ren Z, Qian G, et al. Bowl-like sulfur particles wrapped by graphene oxide as cathode material of lithium–sulfur batteries. RSC Adv 2015;5:28832–5.

[147] Seh ZW, Wang H, Liu N, Zheng G, Li W, Yao H, et al. High-capacity Li2S–graphene oxide composite cathodes with stable cycling performance. Chem Sci 2014;5:1396.

[148] Hwa Y, Zhao J, Cairns EJ. Lithium Sulfide (Li 2 S)/Graphene Oxide Nanospheres with Conformal Carbon Coating as a High-Rate, Long-Life Cathode for Li/S Cells. Nano Lett 2015:150430103348003.

[149] Zeng Q (Ray), Leng X, Wu K-H, Gentle IR, Wang D-W. Electroactive cellulose-supported graphene oxide interlayers for Li–S batteries. Carbon N Y 2015;93:611–9.

[150] Zhang Y, Miao L, Ning J, Xiao Z, Hao L, Wang B, et al. A graphene-oxide-based thin coating on the separator: an efficient barrier towards high-stable lithium–sulfur batteries. 2D Mater 2015;2:024013.

[151] Huang J-Q, Zhuang T-Z, Zhang Q, Peng H-J, Chen C-M, Wei F. Permselective Graphene Oxide Membrane for Highly Stable and Anti-Self-Discharge Lithium-Sulfur Batteries. ACS Nano 2015;9:3002–11.

[152] Chabot V, Higgins D, Yu A, Xiao X, Chen Z, Zhang J. A review of graphene and graphene oxide sponge: material synthesis and applications to energy and the environment. Energy Environ Sci 2014;7:1564.

[153] Song MK, Park S, Alamgir FM, Cho J, Liu M. Nanostructured electrodes for lithium-ion and lithium-air batteries: The latest developments, challenges, and perspectives. Mater Sci Eng R Reports 2011;72:203–52.

[154] Cetinkaya T, Ozcan S, Uysal M, Guler MO, Akbulut H. Free-standing flexible graphene oxide paper electrode for rechargeable Li-O2 batteries. J Power Sources 2014;267:140–7.

[155] Wang ZL, Xu D, Xu JJ, Zhang LL, Zhang XB. Graphene oxide gel-derived, free-standing, hierarchically porous carbon for high-capacity and high-rate rechargeable Li-O 2 batteries. Adv Funct Mater 2012;22:3699–705.

[156] Leung PK, Li X, Ponce de León C, Berlouis L, Low CTJ, Walsh FC. Progress in redox flow batteries, remaining challenges and their applications in energy storage. RSC Adv 2012;2:10125–56.

[157] Wang W, Luo Q, Li B, Wei X, Li L, Yang Z. Recent progress in redox flow battery research and development. Adv Funct Mater 2013;23:970–86.

[158] Weber AZ, Mench MM, Meyers JP, Ross PN, Gostick JT, Liu Q. Redox flow batteries: A review. J Appl Electrochem 2011;41:1137–64.

[159] Chakrabarti MH, Brandon NP, Hajimolana S a., Tariq F, Yufit V, Hashim M a., et al. Application of carbon materials in redox flow batteries. J Power Sources 2014;253:150–66.

[160] Han P, Wang H, Liu Z, Chen X, Ma W, Yao J, et al. Graphene oxide nanoplatelets as excellent electrochemical active materials for VO2+/VO2+ and V2+/V3+ redox couples for a vanadium redox flow battery. Carbon N Y 2011;49:693–700.

[161] Di Blasi O, Briguglio N, Busacca C, Ferraro M, Antonucci V, Di Blasi a. Electrochemical investigation of thermally treated graphene oxides as electrode materials for vanadium redox flow battery. Appl Energy 2015;147:74–81.

[162] González Z, Botas C, Blanco C, Santamaría R, Granda M, Álvarez P, et al. Thermally reduced graphite and graphene oxides in VRFBs. Nano Energy 2013;2:1322–8.

[163] González Z, Botas C, Blanco C, Santamaría R, Granda M, Álvarez P, et al. Graphite oxide-based graphene materials as positive electrodes in vanadium redox flow batteries. J Power Sources 2013;241:349–54.

[164] Li W, Liu J, Yan C. Reduced graphene oxide with tunable C/O ratio and its activity towards vanadium redox pairs for an all vanadium redox flow battery. Carbon N Y 2013;55:313–20.

[165] Park M, Jeon I-Y, Ryu J, Baek J-B, Cho J. Exploration of the Effective Location of Surface Oxygen Defects in Graphene-Based Electrocatalysts for All-Vanadium Redox-Flow Batteries. Adv Energy Mater 2014;5:1–7.

[166] Tsai HM, Yang SY, Ma CCM, Xie X. Preparation and electrochemical properties of graphene-modified electrodes for all-vanadium redox flow batteries. Electroanalysis 2011;23:2139–43.

[167] Xie Z, Yang B, Yang L, Xu X, Cai D, Chen J, et al. Addition of graphene oxide into graphite toward effective positive electrode for advanced zinc-cerium redox flow battery. J Solid State Electrochem 2015:1–7.

[168] Han P, Yue Y, Liu Z, Xu W, Zhang L, Xu H, et al. Graphene oxide nanosheets/multi-walled carbon nanotubes hybrid as an excellent electrocatalytic material towards VO2+/VO2+ redox couples for vanadium redox flow batteries. Energy Environ Sci 2011;4:4710.

[169] Rui X, Oo MO, Sim DH, Raghu SC, Yan Q, Lim TM, et al. Graphene oxide nanosheets/polymer binders as superior electrocatalytic materials for vanadium bromide redox flow batteries. Electrochim Acta 2012;85:175–81.

[170] Govindan M, Moon IS. Improved electrochemical preparation of nano porous-graphene oxide edge like electrode for cerium/vanadium redox flow batteries. Int J Electrochem Sci 2013;8:12172–83.

[171] Dai W, Shen Y, Li Z, Yu L, Qiu X. SPEEK/graphene oxide nanocomposite membranes with superior cyclability for highly efficient vanadium redox flow battery. Journals Mater Chem A 2014;2:12423–32.

[172] Tseng CY, Ye YS, Cheng MY, Kao KY, Shen WC, Rick J, et al. Sulfonated polyimide proton exchange membranes with graphene oxide show improved proton conductivity, methanol crossover impedance, and mechanical properties. Adv Energy Mater 2011;1:1220–4.

[173] Kim BG, Han TH, Cho CG. Sulfonated Graphene Oxide/Nafion Composite Membrane for Vanadium Redox Flow Battery. J Nanosci Nanotechnol 2014;14:9073–7.

[174] Lee KJ, Chu YH. Preparation of the graphene oxide (GO)/Nafion composite

membrane for the vanadium redox flow battery (VRB) system. Vacuum 2014;107:269–76.

[175] Han MH, Gonzalo E, Singh G, Rojo T. A comprehensive review of sodium layered oxides: powerful cathodes for Na-ion batteries. Energy Environ Sci 2015;8:81–102.

[176] Kundu D, Talaie E, Duffort V, Nazar LF. The Emerging Chemistry of Sodium Ion Batteries for Electrochemical Energy Storage. Angew Chemie Int Ed 2015; 54: 3431-48

[177] Palomares V, Serras P, Villaluenga I, Hueso KB, Carretero-González J, Rojo T. Na-ion batteries, recent advances and present challenges to become low cost energy storage systems. Energy Environ Sci 2012;5:5884.

[178] Luo C, Zhu Y, Xu Y, Liu Y, Gao T, Wang J, et al. Graphene oxide wrapped croconic acid disodium salt for sodium ion battery electrodes. J Power Sources 2014;250:372–8.

[179] Luo W, Bommier C, Jian Z, Li X, Carter R, Vail S, et al. Low-Surface-Area Hard Carbon Anode for Na-Ion Batteries via Graphene Oxide as a Dehydration Agent. ACS Appl Mater Interfaces 2015;7:2626–31.

[180] Basirun WJ, Sookhakian M, Baradaran S, Endut Z, Mahmoudian MR, Ebadi M, et al. Graphene oxide electrocatalyst on MnO2 air cathode as an efficient electron pump for enhanced oxygen reduction in alkaline solution. Sci Rep 2015;5:9108.

[181] Tateishi H, Koga T, Hatakeyama K, Funatsu a., Koinuma M, Taniguchi T, et al. Graphene Oxide Lead Battery (GOLB). ECS Electrochem Lett 2014;3:A19–21.

[182] Zhang Q, Scrafford K, Li M, Cao Z, Xia Z, Ajayan PM, et al. Anomalous Capacitive Behaviors of Graphene Oxide Based Solid State Supercapacitors. Nano Lett 2014.

[183] Wang D-W, Du A, Taran E, Lu GQ (Max), Gentle IR. A water-dielectric capacitor using hydrated graphene oxide film. J Mater Chem 2012;22:21085.

[184] Wu C, Huang X, Wu X, Xie L, Yang K, Jiang P. Graphene oxide-encapsulated carbon nanotube hybrids for high dielectric performance nanocomposites with enhanced energy storage density. Nanoscale 2013;5:3847–55.

[185] Zhang LL, Zhou R, Zhao XS. Graphene-based materials as supercapacitor

electrodes. J Mater Chem 2010;20:5983.

[186] Yang P, Mai W. Flexible solid-state electrochemical supercapacitors. Nano Energy 2014;8:274–90.

[187] Faraji S, Nasir F. The development supercapacitor from activated carbon by electroless plating — A review. Renew Sustain Energy Rev 2015;42:823–34.

[188] Xu B, Yue S, Sui Z, Zhang X, Hou S, Cao G, et al. What is the choice for supercapacitors: graphene or graphene oxide? Energy Environ Sci 2011;4:2826–30.

[189] Karthika P. Functionalized Exfoliated Graphene Oxide as Supercapacitor Electrodes. Soft Nanosci Lett 2012;02:59–66.

[190] Dighe AB, Dubal DP, Holze R. Screen Printed Asymmetric Supercapacitors based on LiCoO2 and Graphene Oxide. Zeitschrift Für Anorg Und Allg Chemie 2014;640:2852–7.

[191] Wang Y, Zhu J. One-step electroplating porous graphene oxide electrodes of supercapacitors for ultrahigh capacitance and energy density. Nanotechnology 2015;26:055401.

[192] Zhang Y, Feng H, Wu X, Wang L, Zhang A, Xia T, et al. Progress of electrochemical capacitor electrode materials: A review. Int J Hydrogen Energy 2009;34:4889–99.

[193] Guo SR, Wang W, Ozkan CS, Ozkan M. Assembled graphene oxide and single-walled carbon nanotube ink for stable supercapacitors. J Mater Res 2013;28:918–26.

[194] Lin L-Y, Yeh M-H, Tsai J-T, Huang Y-H, Sun C-L, Ho K-C. A novel core–shell multi-walled carbon nanotube@graphene oxide nanoribbon heterostructure as a potential supercapacitor material. J Mater Chem A 2013;1:11237.

[195] Xue Y, Zhu L, Chen H, Qu J, Dai L. Multiscale patterning of graphene oxide and reduced graphene oxide for flexible supercapacitors. Carbon N Y 2015;92:305–10.

[196] Lekitima JN, Ozoemena KI, Jafta CJ, Kobayashi N, Song Y, Tong D, et al. High-performance aqueous asymmetric electrochemical capacitors based on graphene oxide/cobalt(ii)-tetrapyrazinoporphyrazine hybrids. J Mater Chem A 2013;1:2821.

[197] Hsieh C-T, Hsu S-M, Lin J-Y, Teng H. Electrochemical Capacitors Based on Graphene Oxide Sheets Using Different Aqueous Electrolytes. J Phys Chem C 2011;115:12367–74.

[198] Zhao G, Li J, Jiang L, Dong H, Wang X, Hu W. Synthesizing MnO2 nanosheets from graphene oxide templates for high performance pseudosupercapacitors. Chem Sci 2012;3:433.

[199] Dai K, Lu L, Liang C, Dai J, Liu Q, Zhang Y, et al. In situ assembly of MnO2 nanowires/graphene oxide nanosheets composite with high specific capacitance. Electrochim Acta 2014;116:111–7.

[200] Chen S, Zhu J, Wu X, Han Q, Wang X. Graphene oxide‾ MnO2 nanocomposites for supercapacitors. ACS Nano 2010;4:2822–30.

[201] Jafta CJ, Nkosi F, Le Roux L, Mathe MK, Kebede M, Makgopa K, et al. Manganese oxide/graphene oxide composites for high-energy aqueous asymmetric electrochemical capacitors. Electrochim Acta 2013;110:228–33.

[202] Liu Y, Yan D, Li Y, Wu Z, Zhuo R, Li S, et al. Manganese dioxide nanosheet arrays grown on graphene oxide as an advanced electrode material for supercapacitors. Electrochim Acta 2014;117:528–33.

[203] Gund GS, Dubal DP, Patil BH, Shinde SS, Lokhande CD. Enhanced activity of chemically synthesized hybrid graphene oxide/Mn 3O4 composite for high performance supercapacitors. Electrochim Acta 2013;92:205–15.

[204] Tang Y, Chen T, Yu S, Qiao Y, Mu S, Hu J, et al. Synthesis of graphene oxide anchored porous manganese sulfide nanocrystals via the nanoscale Kirkendall effect for supercapacitors. J Mater Chem A 2015;3:12913–9.

[205] Wu M-S, Lin Y-P, Lin C-H, Lee J-T. Formation of nano-scaled crevices and spacers in NiO-attached graphene oxide nanosheets for supercapacitors. J Mater Chem 2012;22:2442.

[206] Wang A, Wang H, Zhang S, Mao C, Song J, Niu H, et al. Controlled synthesis of nickel sulfide/graphene oxide nanocomposite for high-performance supercapacitor. Appl Surf Sci 2013;282:704–8.

[207] Pendashteh A, Mousavi MF, Rahmanifar MS. Fabrication of anchored copper oxide nanoparticles on graphene oxide nanosheets via an electrostatic coprecipitation and its application as supercapacitor. Electrochim Acta 2013;88:347–57.

[208] Carriazo D, Patiño J, Gutiérrez MC, Ferrer ML, del Monte F. Microwave-assisted synthesis of NiCo2O4–graphene oxide nanocomposites suitable as electrodes for supercapacitors. RSC Adv 2013;3:13690.

[209] Fang J, Li M, Li Q, Zhang W, Shou Q, Liu F, et al. Microwave-assisted synthesis of CoAl-layered double hydroxide/graphene oxide composite and its application in supercapacitors. Electrochim Acta 2012;85:248–55.

[210] Wang L, Wang D, Dong XY, Zhang ZJ, Pei XF, Chen XJ, et al. Layered assembly of graphene oxide and Co-Al layered double hydroxide nanosheets as electrode materials for supercapacitors. Chem Commun (Camb) 2011;47:3556–8.

[211] Simon P, Gogotsi Y. Materials for electrochemical capacitors. Nat Mater 2008;7:845–54.

[212] Zhang LL, Zhao S, Tian XN, Zhao XS. Layered graphene oxide nanostructures with sandwiched conducting polymers as supercapacitor electrodes. Langmuir 2010;26:17624–8.

[213] Liu Y, Deng R, Wang Z, Liu H. Carboxyl-functionalized graphene oxide–polyaniline composite as a promising supercapacitor material. J Mater Chem 2012;22:13619.

[214] Xu G, Wang N, Wei J, Lv L, Zhang J, Chen Z, et al. Preparation of Graphene Oxide/Polyaniline Nanocomposite with Assistance of Supercritical Carbon Dioxide for Supercapacitor Electrodes. Ind Eng Chem Res 2012;51:14390–8.

[215] Wang H, Hao Q, Yang X, Lu L, Wang X. Graphene oxide doped polyaniline for supercapacitors. Electrochem Commun 2009;11:1158–61.

[216] Luo Z, Zhu L, Zhang H, Tang H. Polyaniline uniformly coated on graphene oxide sheets as supercapacitor material with improved capacitive properties. Mater Chem Phys 2013;139:572–9.

[217] Wang H, Hao Q, Yang X, Lu L, Wang X. Effect of graphene oxide on the properties of its composite with polyaniline. ACS Appl Mater Interfaces 2010;2:821–8.

[218] Zhang Q, Li Y, Feng Y, Feng W. Electropolymerization of graphene oxide/polyaniline composite for high-performance supercapacitor. Electrochim Acta 2013;90:95–100.

[219] Xu J, Wang K, Zu S-Z, Han B-H, Wei Z. Hierarchical nanocomposites of polyaniline nanowire arrays on graphene oxide sheets with synergistic effect for energy storage. ACS Nano 2010;4:5019–26.

[220] Mitchell E, Candler J, Souza F De, Gupta RK, Gupta BK, Dong LF. High performance supercapacitor based on multilayer of polyaniline and graphene oxide. Synth Met 2015;199:214–8.

[221] Li ZF, Zhang H, Liu Q, Liu Y, Stanciu L, Xie J. Covalently-grafted polyaniline on graphene oxide sheets for high performance electrochemical supercapacitors. Carbon N Y 2014;71:257–67.

[222] Yan J, Yang L, Cui M, Wang X, Chee KJ, Nguyen VC, et al. Aniline Tetramer-Graphene Oxide Composites for High Performance Supercapacitors. Adv Energy Mater 2014;4.

[223] Konwer S, Boruah R, Dolui SK. Studies on Conducting Polypyrrole/Graphene Oxide Composites as Supercapacitor Electrode. J Electron Mater 2011;40:2248–55.

[224] Li J, Xie H, Li Y. Fabrication of graphene oxide/polypyrrole nanowire composite for high performance supercapacitor electrodes. J Power Sources 2013;241:388–95. d

[225] Hsu F-H, Wu T-M. Enhanced capacitance of one-dimensional polypyrrole/graphene oxide nanoribbon nanocomposite as electrode material for high performance supercapacitors. Synth Met 2014;198:188–95.

[226] Bora C, Dolui SK. Fabrication of polypyrrole/graphene oxide nanocomposites by liquid/liquid interfacial polymerization and evaluation of their optical, electrical and electrochemical properties. Polym (United Kingdom) 2012;53:923–32.

[227] Fan LQ, Liu GJ, Wu JH, Liu L, Lin JM, Wei YL. Asymmetric supercapacitor based on graphene oxide/polypyrrole composite and activated carbon electrodes. Electrochim Acta 2014;137:26–33.

[228] Zhou H, Han G, Xiao Y, Chang Y, Zhai HJ. Facile preparation of polypyrrole/graphene oxide nanocomposites with large areal capacitance using electrochemical codeposition for supercapacitors. J Power Sources 2014;263:259–67.

[229] Zhu C, Zhai J, Wen D, Dong S. Graphene oxide/polypyrrole nanocomposites: one-step electrochemical doping, coating and synergistic effect for energy

storage. J Mater Chem 2012;22:6300.

[230] Li J, Xie H. Synthesis of graphene oxide/polypyrrole nanowire composites for supercapacitors. Mater Lett 2012;78:106–9.

[231] Zhang Y, Li M, Yang L, Yi K, Li Z, Yao J. Facilely prepared polypyrrole-graphene oxide-sodium dodecylbenzene sulfonate nanocomposites by in situ emulsion polymerization for high-performance supercapacitor electrodes. J Solid State Electrochem 2014;18:2139–47.

[232] Cui Y, Cheng Q-Y, Wu H, Wei Z, Han B-H. Graphene oxide-based benzimidazole-crosslinked networks for high-performance supercapacitors. Nanoscale 2013;5:8367.

[233] Luo J, Tung VC, Koltonow AR, Jang HD, Huang J. Graphene oxide based conductive glue as a binder for ultracapacitor electrodes. J Mater Chem 2012;22:12993.

[234] Han G, Liu Y, Zhang L, Kan E, Zhang S, Tang J, et al. MnO2 nanorods intercalating graphene oxide/polyaniline ternary composites for robust high-performance supercapacitors. Sci Rep 2014;4:4824.

[235] Su H, Wang T, Zhang S, Song J, Mao C, Niu H, et al. Facile synthesis of polyaniline/TiO 2/graphene oxide composite for high performance supercapacitors. Solid State Sci 2012;14:677–81.

[236] Chee WK, Lim HN, Harrison I, Chong KF, Zainal Z, Ng CH, et al. Performance of Flexible and Binderless Polypyrrole/Graphene Oxide/Zinc Oxide Supercapacitor Electrode in a Symmetrical Two-Electrode Configuration. Electrochim Acta 2015;157:88–94.

[237] You B, Li N, Zhu H, Zhu X, Yang J. Graphene oxide-dispersed pristine CNTs support for MnO2 nanorods as high performance supercapacitor electrodes. ChemSusChem 2013;6:474–80.

[238] Yuan B, Xu C, Deng D, Xing Y, Liu L, Pang H, et al. Graphene oxide/nickel oxide modified glassy carbon electrode for supercapacitor and nonenzymatic glucose sensor. Electrochim Acta 2013;88:708–12.

[239] Xu D, Xu Q, Wang K, Chen J, Chen Z. Fabrication of Free-Standing Hierarchical Carbon Nano fi ber / Graphene Oxide / Polyaniline Films for Supercapacitors. ACS Appl Mater Interfaces, 2013;6:200–9.

[240] Karim MR, Hatakeyama K, Matsui T, Takehira H, Taniguchi T, Koinuma M, et al. Graphene oxide nanosheet with high proton conductivity. J Am Chem Soc 2013;135:8097–100.

[241] Hatakeyama K, Karim MR, Ogata C, Tateishi H, Funatsu A, Taniguchi T, et al. Proton conductivities of graphene oxide nanosheets: single, multilayer, and modified nanosheets. Angew Chem Int Ed Engl 2014;53:6997–7000.

[242] Gao W, Singh N, Song L, Liu Z, Reddy ALM, Ci L, et al. Direct laser writing of micro-supercapacitors on hydrated graphite oxide films. Nat Nanotechnol 2011;6:496–500.

[243] Yang X, Zhang L, Zhang F, Zhang T, Huang Y, Chen Y. A high-performance all-solid-state supercapacitor with graphene-doped carbon material electrodes and a graphene oxide-doped ion gel electrolyte. Carbon N Y 2014;72:381–6.

[244] Yang X, Zhang F, Zhang L, Zhang T, Huang Y, Chen Y. A High-Performance Graphene Oxide-Doped Ion Gel as Gel Polymer Electrolyte for All-Solid-State Supercapacitor Applications. Adv Funct Mater 2013;23:3353–60.

[245] Huang Y-F, Wu P-F, Zhang M-Q, Ruan W-H, Giannelis EP. Boron cross-linked graphene oxide/polyvinyl alcohol nanocomposite gel electrolyte for flexible solid-state electric double layer capacitor with high performance. Electrochim Acta 2014;132:103–11.

[246] Chandan A, Hattenberger M, El-kharouf A, Du S, Dhir A, Self V, et al. High temperature (HT) polymer electrolyte membrane fuel cells (PEMFC) – A review. J Power Sources 2013;231:264–78.

[247] Giddey S, Badwal SPS, Kulkarni a., Munnings C. A comprehensive review of direct carbon fuel cell technology. Prog Energy Combust Sci 2012;38:360–99.

[248] Mekhilef S, Saidur R, Safari a. Comparative study of different fuel cell technologies. Renew Sustain Energy Rev 2012;16:981–9.

[249] Wang Y-J, Qiao J, Baker R, Zhang J. Alkaline polymer electrolyte membranes for fuel cell applications. Chem Soc Rev 2013;42:5768–87.

[250] Wang Y, Chen KS, Mishler J, Cho SC, Adroher XC. A review of polymer electrolyte membrane fuel cells: Technology, applications, and needs on fundamental research. Appl Energy 2011;88:981–1007.

[251] Jung JH, Park HJ, Kim J, Hur SH. Highly durable Pt/graphene oxide and Pt/C

hybrid catalyst for polymer electrolyte membrane fuel cell. J Power Sources 2014;248:1156–62.

[252] Lei M, Wang ZB, Li JS, Tang HL, Liu WJ, Wang YG. CeO2 nanocubes-graphene oxide as durable and highly active catalyst support for proton exchange membrane fuel cell. Sci Rep 2014;4:7415.

[253] Park HY, Shin TJ, Joh HI, Jang JH, Ahn D, Yoo SJ. Graphene-oxide-intercalated layered manganese oxides as an efficient oxygen reduction reaction catalyst in alkaline media. Electrochem Commun 2014;41:35–8.

[254] Chen X, Wu G, Chen J, Chen X, Xie Z, Wang X. Synthesis of "clean" and well-dispersive pd nanoparticles with excellent electrocatalytic property on graphene oxide. J Am Chem Soc 2011;133:3693–5.

[255] Kakaei K. Decoration of graphene oxide with Platinum Tin nanoparticles for ethanol oxidation. Electrochim Acta 2015;165:330–7..

[256] Khan M, Yousaf A Bin, Chen M, Wei C, Wu X, Huang N, et al. Mixed-phase Pd–Pt bimetallic alloy on graphene oxide with high activity for electrocatalytic applications. J Power Sources 2015;282:520–8.

[257] Li X-R, Li X-L, Xu M-C, Xu J-J, Chen H-Y. Gold nanodendrities on graphene oxide nanosheets for oxygen reduction reaction. J Mater Chem A 2014;2:1697.

[258] Yuan L, Jiang L, Liu J, Xia Z, Wang S, Sun G. Facile synthesis of silver nanoparticles supported on three dimensional graphene oxide/carbon black composite and its application for oxygen reduction reaction. Electrochim Acta 2014;135:168–74.

[259] Gupta VK, Yola ML, Atar N, Üstündağ Z, Solak AO. Electrochemical studies on graphene oxide-supported metallic and bimetallic nanoparticles for fuel cell applications. J Mol Liq 2014;191:172–6.

[260] Naveen MH, Noh H-B, Hossain MS Al, Kim JH, Shim Y-B. Facile potentiostatic preparation of functionalized polyterthiophene-anchored graphene oxide as a metal-free electrocatalyst for the oxygen reduction reaction. J Mater Chem A 2015;3:5426–33.

[261] Qu K, Zheng Y, Dai S, Qiao SZ. Polydopamine–graphene oxide derived mesoporous carbon nanosheets for enhanced oxygen reduction. Nanoscale 2015;7:12598–605.

[262] Xu J, Dong G, Jin C, Huang M, Guan L. Sulfur and nitrogen co-doped, few-layered graphene oxide as a highly efficient electrocatalyst for the oxygen-reduction reaction. ChemSusChem 2013;6:493–9.

[263] Tateishi H, Hatakeyama K, Ogata C, Gezuhara K, Kuroda J, Funatsu a., et al. Graphene Oxide Fuel Cell. J Electrochem Soc 2013;160:F1175–8.

[264] Bayer T, Bishop SR, Nishihara M, Sasaki K, Lyth SM. Characterization of a graphene oxide membrane fuel cell. J Power Sources 2014;272:239–47.

[265] Transactions ECS, Society TE. Graphene Oxide Membrane Fuel Cells: Utilizing of a New Class of Ionic Conductor. ECS Trans 2014;64:441–8.

[266] Gao W, Wu G, Janicke MT, Cullen D a., Mukundan R, Baldwin JK, et al. Ozonated graphene oxide film as a proton-exchange membrane. Angew Chemie - Int Ed 2014;53:3588–93.

[267] Ravikumar, Scott K. Freestanding sulfonated graphene oxide paper: a new polymer electrolyte for polymer electrolyte fuel cells. Chem Commun 2012;48:5584.

[268] Jiang Z, Shi Y, Jiang Z-J, Tian X, Luo L, Chen W. High performance of a free-standing sulfonic acid functionalized holey graphene oxide paper as a proton conducting polymer electrolyte for air-breathing direct methanol fuel cells. J Mater Chem A 2014;2:6494.

[269] Kim Y, Ketpang K, Jaritphun S, Park JS, Shanmugam S. A polyoxometalate coupled graphene oxide–Nafion composite membrane for fuel cells operating at low relative humidity. J Mater Chem A 2015;3:8148–55.

[270] Feng K, Tang B, Wu P. "Evaporating" graphene oxide sheets (GOSs) for rolled up GOSs and its applications in proton exchange membrane fuel cell. ACS Appl Mater Interfaces 2013;5:1481–8.

[271] Lee DC, Yang HN, Park SH, Kim WJ. Nafion/graphene oxide composite membranes for low humidifying polymer electrolyte membrane fuel cell. J Memb Sci 2014;452:20–8.

[272] Wang L, Kang J, Nam J-D, Suhr J, Prasad a. K, Advani SG. Composite Membrane Based on Graphene Oxide Sheets and Nafion for Polymer Electrolyte Membrane Fuel Cells. ECS Electrochem Lett 2014;4:F1–4.

[273] Zarrin H, Higgins D, Jun Y, Chen Z, Fowler M. Functionalized graphene oxide

nanocomposite membrane for low humidity and high temperature proton exchange membrane fuel cells. J Phys Chem C 2011;115:20774–81.

[274] Chien HC, Tsai LD, Huang CP, Kang CY, Lin JN, Chang FC. Sulfonated graphene oxide/Nafion composite membranes for high-performance direct methanol fuel cells. Int J Hydrogen Energy 2013;38:13792–801.

[275] Choi BG, Huh YS, Park YC, Jung DH, Hong WH, Park H. Enhanced transport properties in polymer electrolyte composite membranes with graphene oxide sheets. Carbon N Y 2012;50:5395–402.

[276] Lin CW, Lu YS. Highly ordered graphene oxide paper laminated with a Nafion membrane for direct methanol fuel cells. J Power Sources 2013;237:187–94.

[277] Lue SJ, Pai Y-L, Shih C-M, Wu M-C, Lai S-M. Novel bilayer well-aligned Nafion/graphene oxide composite membranes prepared using spin coating method for direct liquid fuel cells. J Memb Sci 2015;493:212–23.

[278] Nicotera I, Simari C, Coppola L, Zygouri P, Gournis D, Brutti S, et al. Sulfonated Graphene Oxide Platelets in Nafion Nanocomposite Membrane: Advantages for Application in Direct Methanol Fuel Cells. J Phys Chem C 2014;118:24357–68.

[279] Sha Wang L, Nan Lai A, Xiao Lin C, Gen Zhang Q, Mei Zhu A, Lin Liu Q. Orderly sandwich-shaped graphene oxide/Nafion composite membranes for direct methanol fuel cells. J Memb Sci 2015;492:58–66.

[280] Beydaghi H, Javanbakht M. Aligned Nanocomposite Membranes Containing Sulfonated Graphene Oxide with Superior Ionic Conductivity for Direct Methanol Fuel Cell Application. Ind Eng Chem Res 2015;54:7028–37.

[281] Beydaghi H, Javanbakht M, Bagheri A, Salarizadeh P, Zahmatkesh HG-, Kashefi S, et al. Novel nanocomposite membranes based on blended sulfonated poly(ether ether ketone)/poly(vinyl alcohol) containing sulfonated graphene oxide/Fe$_3$O$_4$ nanosheets for DMFC applications. RSC Adv 2015;5:74054–64.

[282] Beydaghi H, Javanbakht M, Kowsari E. Synthesis and Characterization of Poly(vinyl alcohol)/Sulfonated Graphene Oxide Nanocomposite Membranes for Use in Proton Exchange Membrane Fuel Cells (PEMFCs). Ind Eng Chem Res 2014;53:16621–32.

[283] Cao YC, Xu C, Wu X, Wang X, Xing L, Scott K. A poly (ethylene oxide)/graphene oxide electrolyte membrane for low temperature polymer fuel cells. J Power Sources 2011;196:8377–82.

[284] Heo Y, Im H, Kim J. The effect of sulfonated graphene oxide on Sulfonated Poly (Ether Ether Ketone) membrane for direct methanol fuel cells. J Memb Sci 2013;425-426:11–22.

[285] He Y, Wang J, Zhang H, Zhang T, Zhang B, Cao S, et al. Polydopamine-modified graphene oxide nanocomposite membrane for proton exchange membrane fuel cell under anhydrous conditions. J Mater Chem A 2014;2:9548.

[286] Jiang Z, Zhao X, Fu Y, Manthiram A. Composite membranes based on sulfonated poly(ether ether ketone) and SDBS-adsorbed graphene oxide for direct methanol fuel cells. J Mater Chem 2012:24862–9.

[287] Jiang Z, Zhao X, Manthiram A. Sulfonated poly(ether ether ketone) membranes with sulfonated graphene oxide fillers for direct methanol fuel cells. Int J Hydrogen Energy 2013;38:5875–84.

[288] Ko T, Kim K, Lim M-Y, Nam SY, Kim T-H, Kim S-K, et al. Sulfonated Poly(arylene ether sulfone) Composite Membranes Having Poly(2,5-benzimidazole)-Grafted Graphene Oxide for Fuel Cell Applications. J Mater Chem A 2015.

[289] Kumar R, Mamlouk M, Scott K. Sulfonated polyether ether ketone – sulfonated graphene oxide composite membranes for polymer electrolyte fuel cells. RSC Adv 2014;4:617.

[290] Yuan T, Pu L, Huang Q, Zhang H, Li X, Yang H. An effective methanol-blocking membrane modified with graphene oxide nanosheets for passive direct methanol fuel cells. Electrochim Acta 2014;117:393–7.

[291] Xue C, Zou J, Sun Z, Wang F, Han K, Zhu H. Graphite oxide/functionalized graphene oxide and polybenzimidazole composite membranes for high temperature proton exchange membrane fuel cells. Int J Hydrogen Energy 2014;39:7931–9.

[292] He Y, Tong C, Geng L, Liu L, Lü C. Enhanced performance of the sulfonated polyimide proton exchange membranes by graphene oxide: Size effect of graphene oxide. J Memb Sci 2014;458:36–46.

Chapter 3 Study of Oxidised CNTs with Different Degrees of Oxidation

3.1 Introduction

It is reported that a carbon nanotube (CNT) is unzipped from the central part and then is longitudinally scissored to form a nanoribbon, as illustrated in Figure 22a.[1] The proposed first step in the process is manganate ester formation (2, Figure 22b) as the rate-determining step, and further oxidation is possible to afford the dione (3, Figure 22b) in the dehydrating medium. The adjacent ketones distort the β,γ-alkenes (red in 3), making them more prone to the next attack by permanganate. As the process continues, the bond-angle strain induced by the enlarging hole would make the β,γ-alkenes (4, Figure 22b) increasingly reactive.[1] Hence, once an opening has been initiated, its further opening is enhanced relative to an unopened tube or to an uninitiated site on the same tube. The ketones can be further converted to the carboxylic acids that will line the edges of the nanoribbons.[1] Finally, relief of the bond-angle strain when the nanotube opens to the nanoribbon (5, Figure 22b) slows further dione formation and cutting. Also, the degree of consecutive tube opening in the multiwalled CNTs can be controlled by adjusting the amount of oxidizing agent introduced into the system.
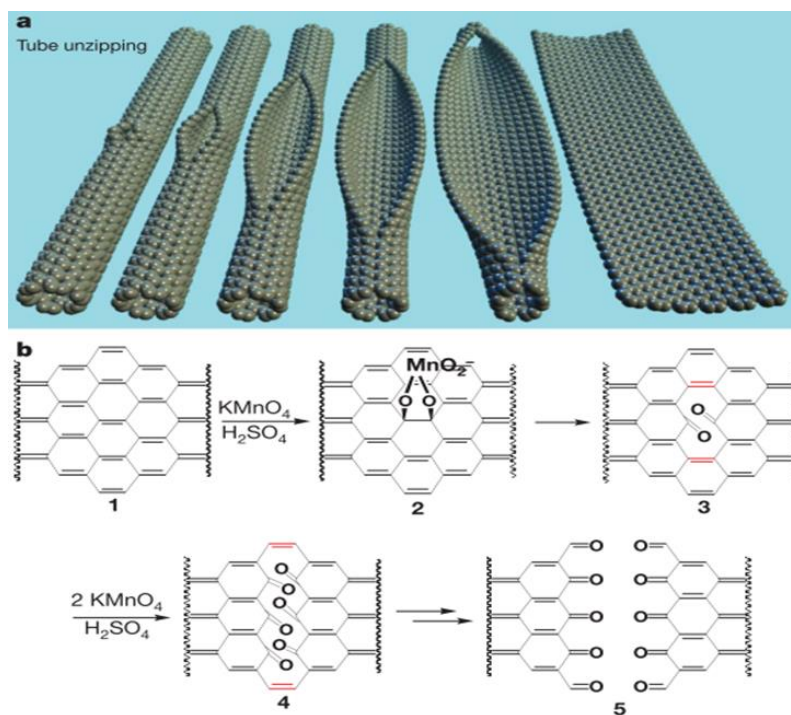
Figure 22. (a) Longitudinal opening of a carbon nanotube to form a nanoribbon; (b) Mechanism of CNT unzipping.[1]

As abundance of oxygen-containing functional groups are introduced, the nanoribbons produced are electrically insulating, which considerably limits its applications in the electrochemical devices. In order to compensate its poor electrical conductivity, CNTs, in this research, will be mixed with oxidised CNTs proportionally. The oxidised CNTs with different extents of the tube opening will be produced by using various proportions of $KMnO_4$ to CNTs. Furthermore, it is found that the abundant oxygen-containing functional groups occurring in the GO, theoretically, are advantageous for the supercapacitors, as they can provide a large additional pseudo-capacitance as well as improved wettability, giving a higher capacitance.[2] Therefore, the electrochemical performances of the as-prepared samples will be investigated in this research, which aims to determine their potential application in the supercapacitors.

3.2 Experimental Section

3.2.1 Oxidation of CNTs at different degrees of oxidation

The oxidation of CNTs was achieved by three steps as follows:

1) Purification of CNTs

20% hydrochloride acid solution was used to dissolve away the possible metal impurities in the CNTs. The mixture of CNTs and HCl solution were kept stirring for about 5 hours until all the metal impurities were dissolved. Herein the solution turned green, probably due to the existence of the iron and/or cobalt ions. Subsequently, the as-received solution was washed *via* a vacuum filtration with sufficient deionised water for the removal of the excess HCl solution. Finally, the purified CNTs were dried in an oven at 60^0C for overnight.

2) Oxidation of CNTs based on the improved Hummers method

98% concentrated sulphuric acid and potassium permanganate were involved to oxidise the CNTs. Firstly per 1.0g of purified CNTs was added with 120ml of 98% concentrated sulphuric acid and then added with the potassium permanganate. As different proportions of $KMnO_4$ to CNTs affected the degree of oxidation, in this

experiment, 10:1, 5:1, 3:1 and 1:1 were used to oxidise the CNTs. That is, 10g, 5g, 3g and 1g of $KMnO_4$ were added in per 1.0g of CNTs respectively. Secondly, the mixed solution containing CNTs, concentrated H_2SO_4 and $KMnO_4$ was kept stirring at 60^0C for 4 hours. Finally, after 4 hours, while the solution cooled down, 300ml water solution containing 10ml 30% H_2O_2 solution was added slowly and kept stirring for another 1 hour. Herein dark green or brown solution was observed. The H_2O_2 solution was used to remove the redundant $KMnO_4$. In order to describe clearly, each sample is abbreviated below:

Table 6. Abbreviations of the samples with different degrees of oxidation

CNTs	Carbon nanotubes without oxidation
1:1 oCNTs	Oxidised carbon nanotubes prepared by the $KMnO_4$-CNT proportion of **1:1**
3:1 oCNHs	Oxidised carbon nanohybrids prepared by the $KMnO_4$-CNT proportion of **3:1**
5:1 GONRs-1	Graphene oxide nanoribbons prepared by the $KMnO_4$-CNT proportion of **5:1**
10:1 GONRs-2	Graphene oxide nanoribbons prepared by the $KMnO_4$-CNT proportion of **10:1**

3)   Collection of as-prepared oxidised samples

After the oxidation, the solution was separated by a centrifuge at 8000 rpm for 30 mins so as to obtain the samples at the bottom of centrifuge tubes. The samples were dispersed in the deionised water using a bath sonication and then they were separated again by the centrifuge at 10000rpm for 30min. Both procedures were repeated until the samples turn to be neutral. Finally, the neutral samples were dried in the oven at 60^oC.

3.2.2 Sample characterisations

The Philips CM200 transmission electron microscopy (TEM) can produce the images with very high resolution and therefore it was employed to provide the structural information of the different samples. Furthermore, the Renishaw inVia Raman

Microscope using the 514nm laser was used to determine the structural differences in chemistry. The X-ray photoelectron spectroscopy, the Varian 640 FTIR Spectrometer and the PANalytical PW1830 X-ray Diffraction System were also utilised to study the CNT and oxidised CNT samples. The use of these instruments aimed to uncover the structural differences of the samples at various oxidation levels.

3.2.3 Preparation of the CNT-mixed samples in the Nafion solution

In order to increase the electrical conductivity, the CNTs were mixed with the oxidised samples in the different percentages and then the mixtures were dispersed in the 0.5 wt% Nafion solution with the concentration of 5mg/mL using a probe sonication. More details are shown in Table 7.

Table 7. Proportions of CNTs and oxidised samples in the Nafion solution

	CNTs	GONRs	Nafion solution
1:1 oCNTs	10 mg	40 mg	10 mL
	30 mg	20 mg	10 mL
3:1 oCNHs	10 mg	40 mg	10 mL
	30 mg	20 mg	10 mL
5:1 GONTs-1	10 mg	40 mg	10 mL
	30 mg	20 mg	10 mL
10:1 GONRs-2	10 mg	40 mg	10 mL
	30 mg	20 mg	10 mL

3.2.4 Cyclic voltammograms using a three-electrode potentiostat

In terms of the capacitive performances, the samples in the Nafion solutions were investigated by a three-electrode potentiostat using 1M H_2SO_4 aqueous electrolyte solution at different scan rates, which aimed to determine the optimal sample for the later use in a supercapacitor. The 3-electrode potentiostat was composed of a Hg/HgSO$_4$ reference electrode and a Pt counter electrode.

3.3 Results and Discussion

3.3.1 Instrumental analysis

The SEM provides the nanostructural information of the oxidised samples, which are presented in Figure 23. 1:1 oCNTs retain a tube structure similar with the CNTs, yet 3:1 oCNHs start to unzip on the mid-section of the nanotube rather than at one end. In the 5:1 GONRs-1 sample, the nanoribbons have been formed with some parts of inner tubes remaining. As for the 10:1 GONRs-2, the nanotubes are completely unravelled to form the nanoribbon structures. The SEM analysis reveals that as the amount of $KMnO_4$ is increased, the walls of the CNTs open to a higher degree. That is, the degree of oxidation effectively determines the extent of the CNT opening. A higher oxidation level can result in the complete unzipping of the CNT walls to yield the nanoribbons. Hence, the degree of consecutive tube opening in the CNTs can be controlled by adjusting the amount of oxidizing agent introduced into the system.
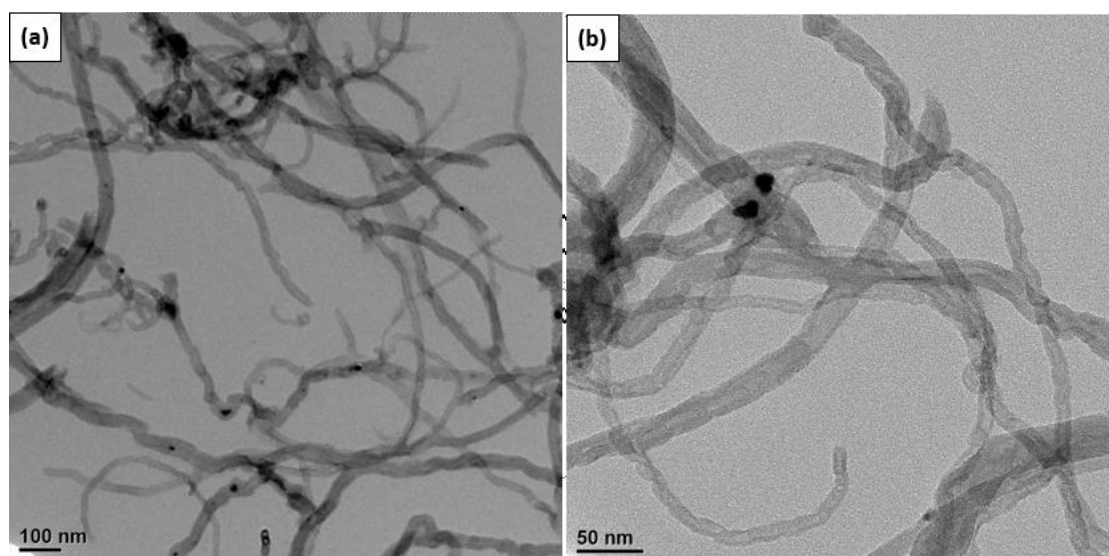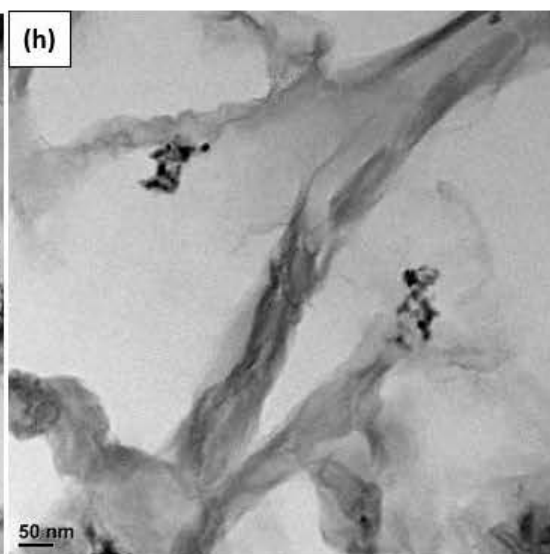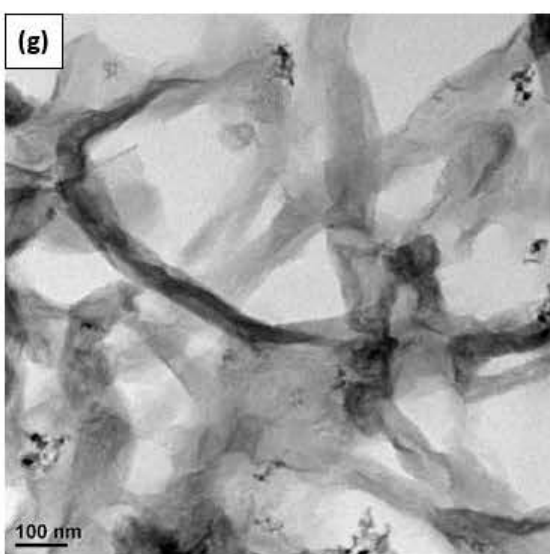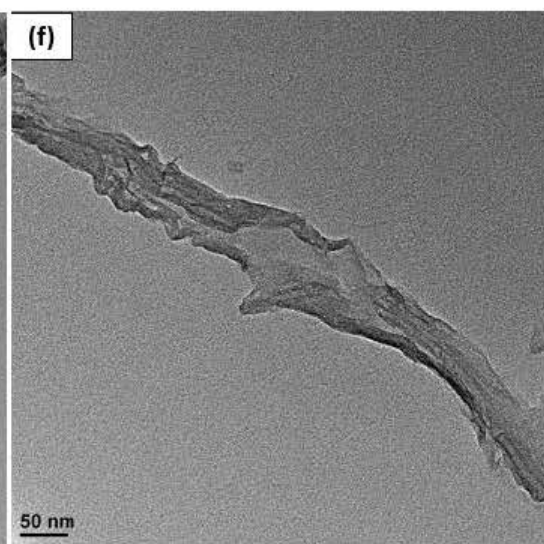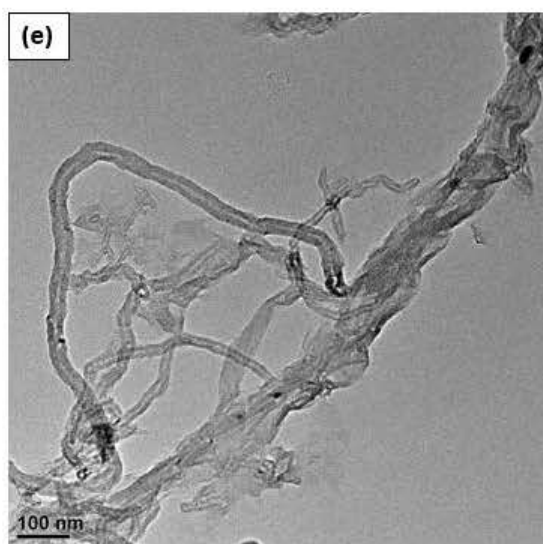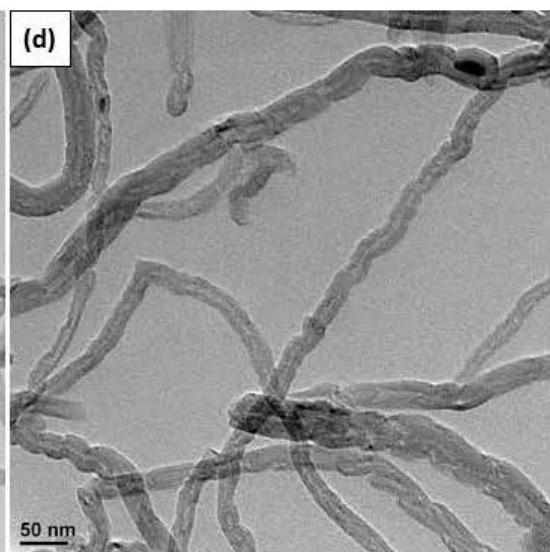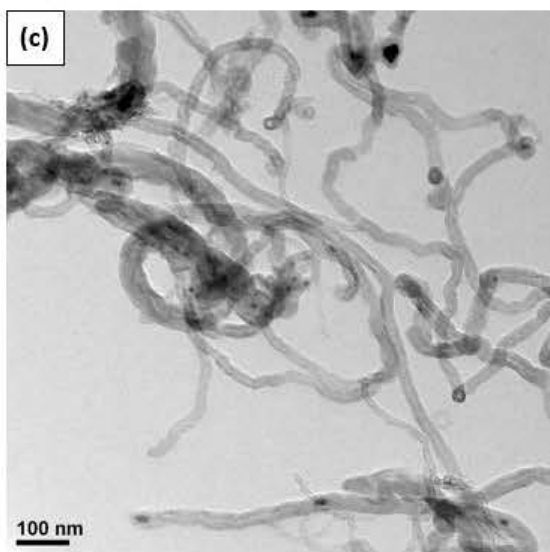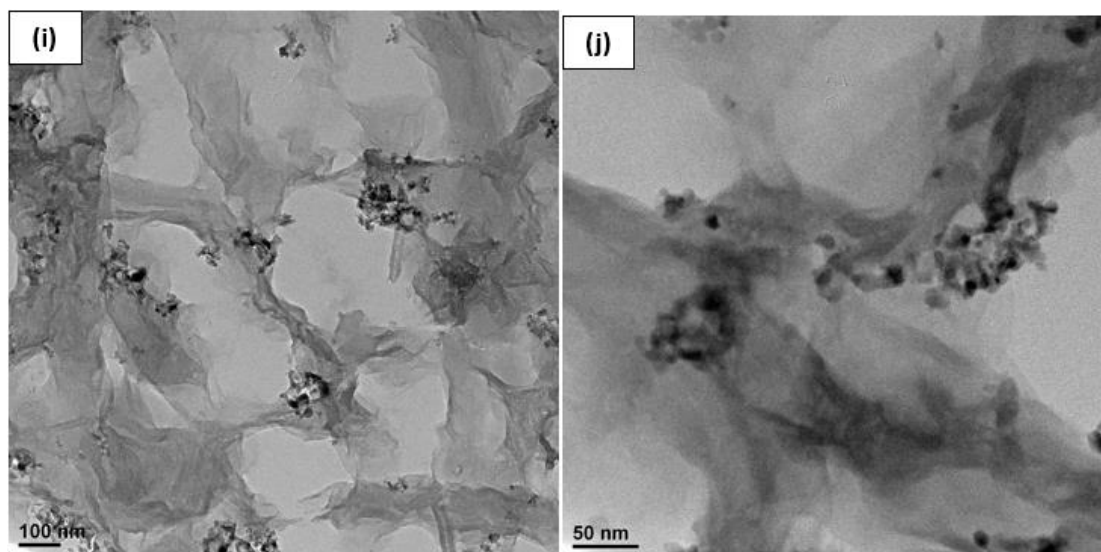
Figure 23. TEM images of all as-prepared samples: (a) and (b) CNTs; (c) and (d) 1:1 oCNTs; (e) and (f) 3:1 oCNHs; (g) and (h) 5:1 CONRs-1; (i) and (j) 10:1 GONTs-2.

Raman spectroscopy is a non-destructive technique that is widely used to obtain structural information about carbon-based materials. The main features in the Raman spectra of graphitic carbon-based materials are the G and D peaks and their overtones. Figure 24 shows the Raman analysis results of CNTs and different oxidised samples. The spectrum peak at ~1580 cm^{-1} is the G band, which represents the ideal crystal graphite structure and is caused by the stretching vibration of sp^2 type C-C bonds in the condensed ring structure of the crystal lattice graphite surface, i.e., by the doubly degenerated planar optical vibration. The spectrum peak near 1360 cm^{-1} is the D band caused by crystal grain size, as well as the disorderly structure and defects of carbon materials, i.e., by double-resonance Raman scattering. The spectrum peak at ~2700 cm^{-1} is the second-order double-frequency peak of the D peak (2D region), which also originates from the double-resonance Raman scattering with the added involvement of double phonons. A CNT can be thought of as a hexagonal network of carbon atoms that has been rolled up to make a seamless cylinder. In the Raman spectrum of CNTs, a sharp G peak can be observed, which derived from the graphite-like in-plane mode and its D peak is weaker, which can be connected with intrinsic impurities (defects) of nanotubes. As the oxidation of CNTs is increased, the bonding mode of the surface carbon-carbon bonds is changed, and the oxidation destroys the symmetry of C-C structure, causing the enhanced D and G bands. This can be explained in three aspects. First, some carbon atoms of the condensed-ring graphite are oxidised into

carbon atoms in sp^3 configuration. Second, the stretching vibration frequency of the C-C bonds in sp^2 configuration, which connect with the carbon atoms in sp^3 configuration, differs from that of the original condensed-ring structure. Third, the introduced oxygen-containing functional groups break up the ordered C-C structure of CNT. Also, 2D band, which is the overtone of D band, is seen to be broadened with increase in oxidation, indicating the presence of defects in graphitic materials. The difference of 2D-band between these samples is attributed to their difference in structures, which supports TEM measurements. A defect-activated peak called D+G is also readily visible near 2950 cm^{-1} in the spectra of 3:1, 5:1 and 10:1 oxidised samples and there is no obvious D+G peak in the 1:1 oCNTs. This is because oCNTs still retain the tube structure, which did not experience the opening of the nanotubes. The ever-increasing defect signals indicate that as the degree of oxidation increases, the oxygen functional groups are introduced gradually.
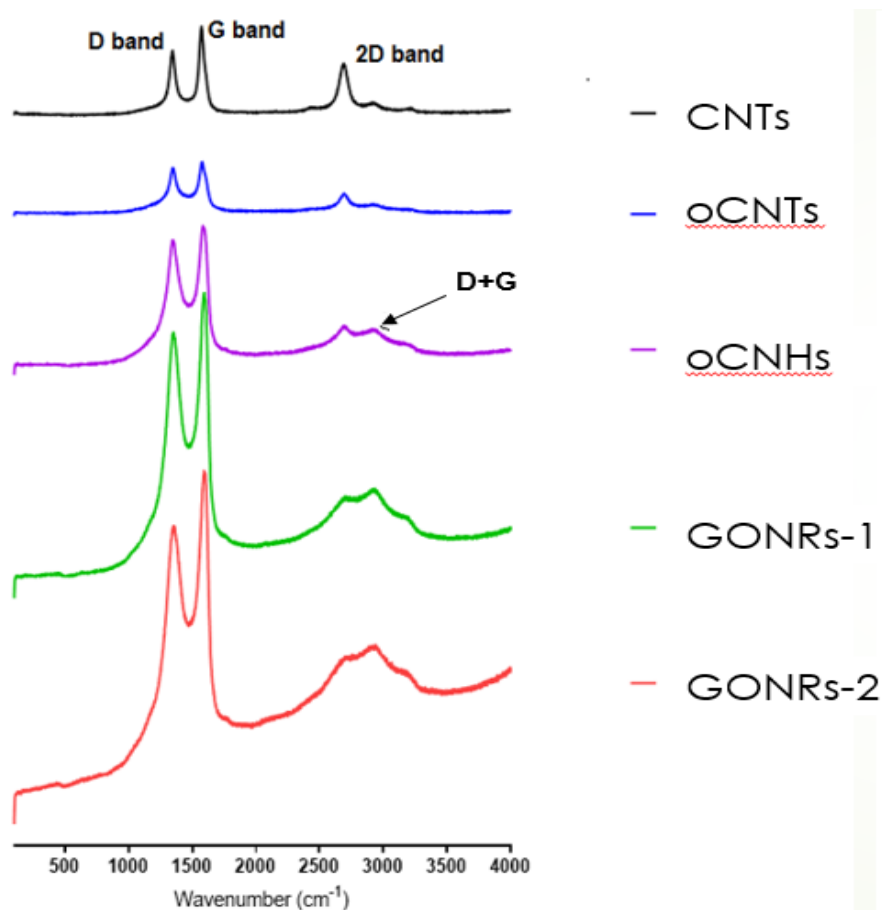
Figure 24. Raman spectra of CNTs, oCNTs, oCNHs, GONRs-1 and GONRs-2.

X-ray diffraction (XRD) analysis (Figure 25) was also performed to investigate further the structure of the partly and completely unzipped CNT–nanoribbon structures. CNTs and 1:1 oCNTs have 2θ values of ~26.8^o, which indicate that they have the same interlayered spacing. But the peak intensity of 1:1 oCNTs is weaker than that of CNTs, probably suggesting that at such oxidation level (KMnO$_4$:CNTs=1:1), the outermost layers of the nanotubes start to unzip with the intact inner structure remaining. As for 3:1 oCNHs, the peak intensity at ~26.8^o is much weaker, but a new peak emerges at 2θ value of ~10.8^o. This can be an evidence that the nanotubes of 3:1 samples are partly opened (as seen in 3:1 oCNHs TEM images in Figure 23). In terms of 5:1 and 10:1 GONR samples, the peak at ~26.8^o disappears and the peak at ~10.8^o can be explicitly observed, indicative of the complete opening of the nanotubes. Besides, the decreased 2θ values mean the increased d-spacing so that the interlayered distance increases with the level of oxidation. This is attributed to the introduction of oxygen-containing functional groups as well as water molecules. The XRD results are consistent with the TEM and Raman measurements.
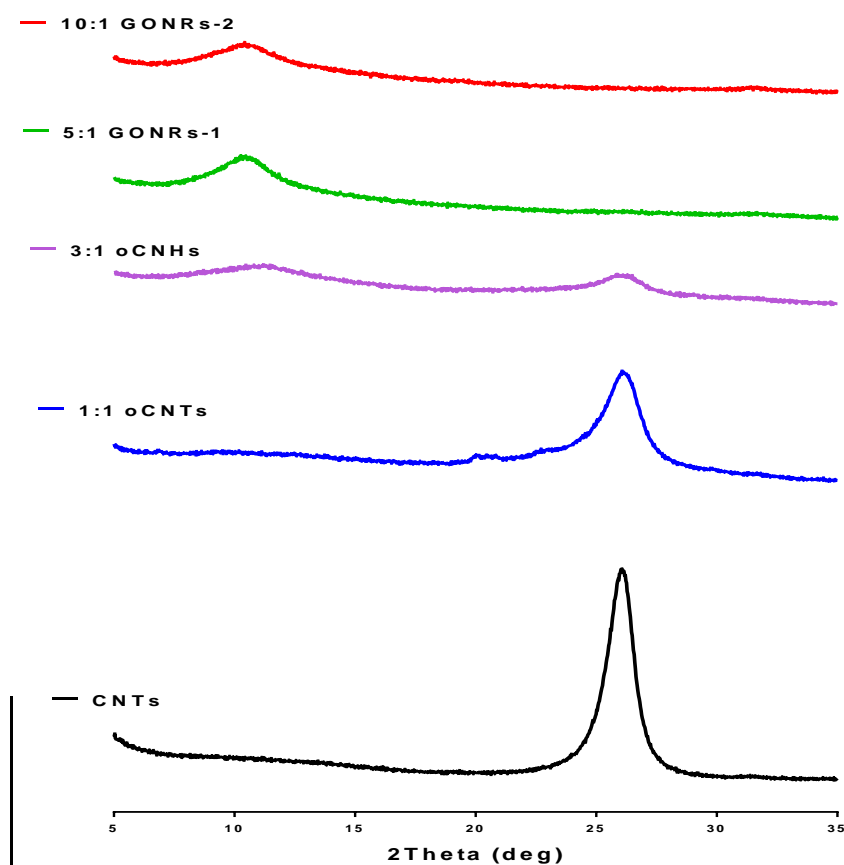

Figure 25. XRD analysis of CNTs, oCNTs, oCNHs, GONRs-1 and GONRs-2.

Figure 26 shows the FTIR spectra of CNTs and different oxidised samples, which confirm the introduction of oxygen-based functional groups on the CNTs. As the oxidation level increases, near 3430 cm^{-1} in the high frequency area, there is an ever-increasing broader spectrum peak occurring within 3000–3700 cm^{-1} caused by the stretching vibration of OH of adsorbed water molecules. Correspondingly, the absorption peak based on the bending vibration of OH in water molecules at 1630 cm^{-1} also becomes stronger. These are because of the larger quantity of surface functional groups to be introduced, which lead to the formation of hydrogen bonds. Therefore, it can be concluded that the sample with a higher degree of oxidation has strong hydrophilicity. The absorption peaks at 2930 cm^{-1} and 2850 cm^{-1} represent the symmetric and anti-symmetric stretching vibrations of CH_2, while the absorption peak occurring near 1720 cm^{-1} in the medium frequency area results from the stretching vibration of C=O of carboxylic acid and carbonyl groups occurring at the samples. Finally, the absorption peaks at 1384 cm^{-1} and 1118 cm^{-1} are caused by the vibration of C-O of carboxylic acid and the stretching vibration of C-OH of alcohol, respectively. The existence and ever-increasing signals of these oxygen-containing groups reveal that the CNT has been oxidised gradually with the increase of the oxidation level.
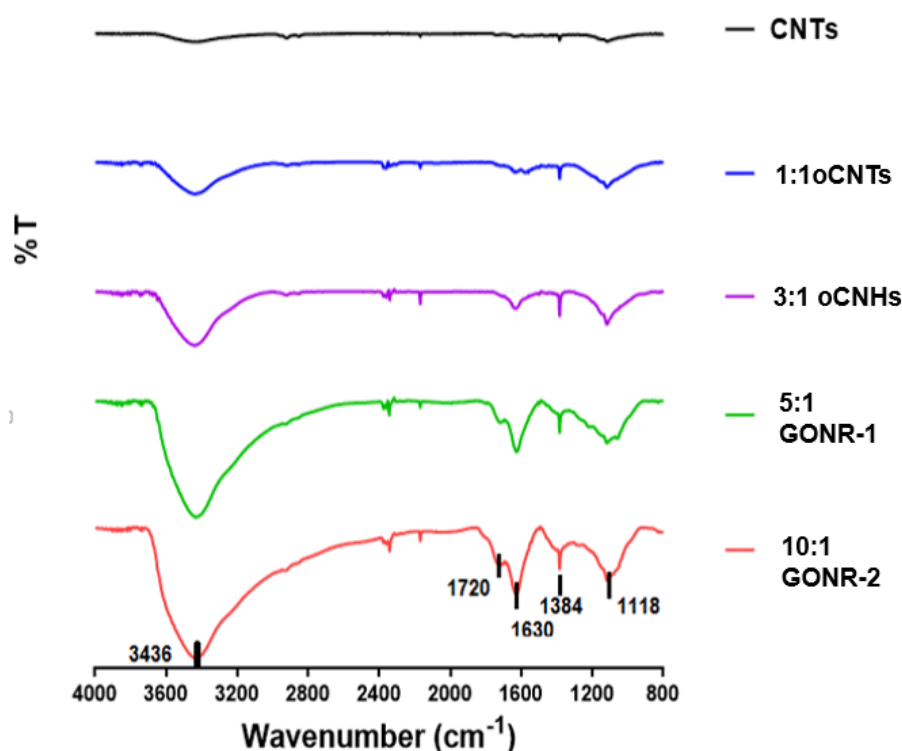

Figure 26. FTIR spectra of CNTs, oCNTs, oCNHs, GONRs-1 and GONRs-2.

3.3.2 Investigation of electrochemical performances of all samples in 1M H$_2$SO$_4$ electrolyte solution
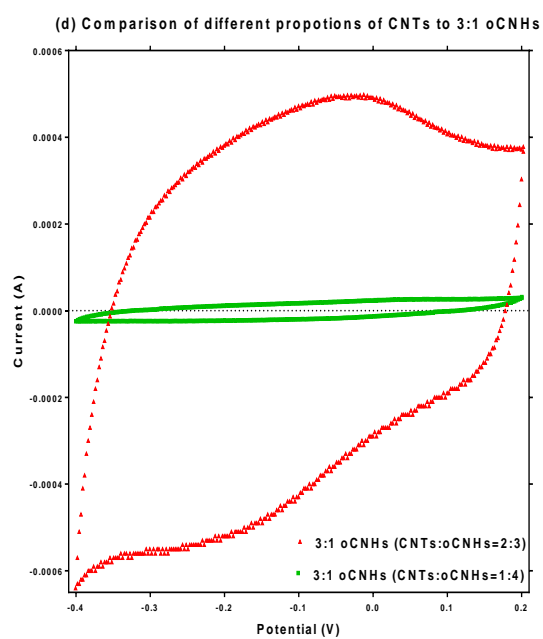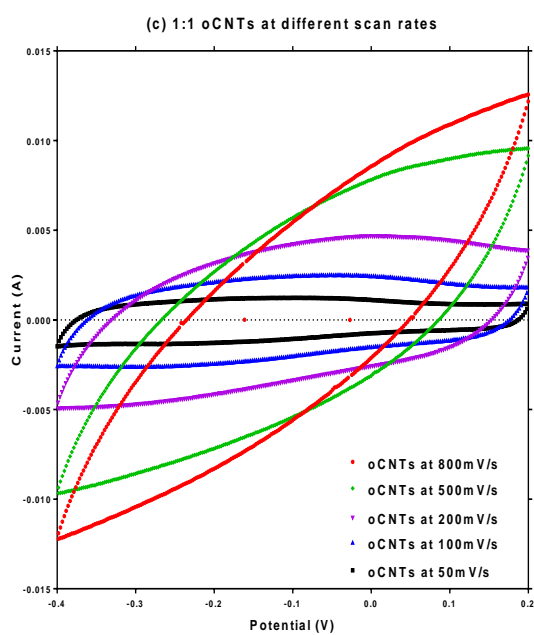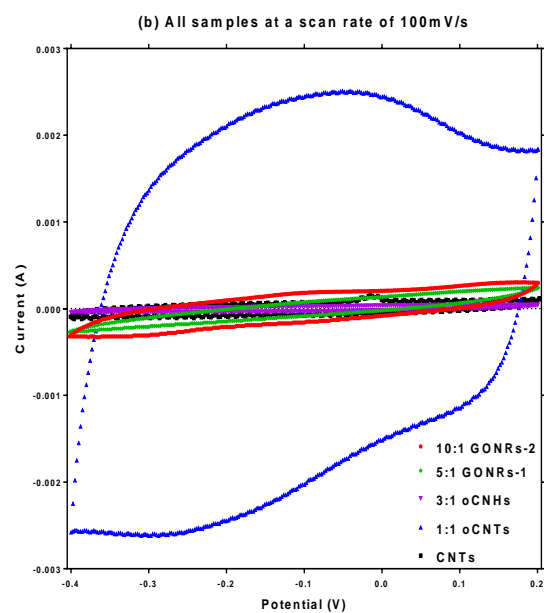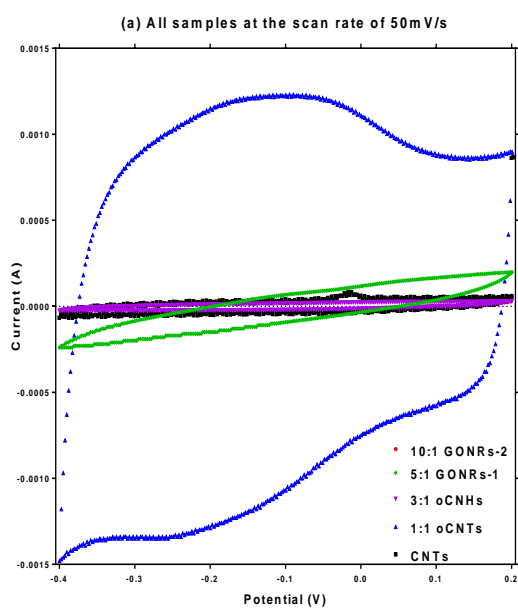
GO is an electrically insulating material due to its disrupted sp^2 bonding network. In order to enhance the electrical conductivity, CNTs were mixed with 1:1 oCNTs, 3:1 oCNHs, 5:1 and 10:1 GONRs proportionally (CNTs: GONRs=1: 4) in this research. The electrochemical performances of CNTs and CNT-mixed oxidised samples were measured in a three-electrode cell. Figure 27a exhibits the cyclic voltammograms of all these samples in 1M H$_2$SO$_4$ aqueous electrolyte solution between -0.4 and 0.2 V at a scan rate of 50 mV/s. The CV curve of 1:1 oCNTs shows a rectangle-like shape with a well-broadened peak at around -0.35-0.03 V, indicating the presence of pseudo-capacitance. However, the CV curves of other samples (CNTs and 3:1, 5:1, 10:1 samples) present much smaller current ranges than that of 1:1 oCNTs. . The cyclic voltammograms of all samples at a scan rate of 100 mV/s further demonstrate that the 1:1 oCNT sample exhibits the best capacitive behaviour with the largest current range, as illustrated in Figure 27b.

The above results can be explained as follows. On one hand, CNT, although it possesses a superior electrical conductivity, does not contain the functional groups, implying that its capacitive behaviour merely refers to the electrical double layer capacitance from pure electrostatic charge accumulation at the electrode-electrolyte interface. The poor wettability of CNTs in aqueous electrolyte, on the other hand, can decelerate the ion transport at the electrode-electrolyte interfaces, thereby negatively affecting the electrochemical performance. In terms of 3:1 oCNHs, 5:1 and 10:1 GONRs, they have the larger amount of sp^3 C-O bonding so that the higher degrees of structural disorder make them to be more insulating. Interestingly, increasing the amount of CNTs mixing with oxidised samples can enhance the electrochemical performance. Figure 27d shows the CV curves of 3:1 oCNHs mixing with different amounts of CNTs. When the mixing ratio of CNTs to oCNHs is increased to 2:3, such CNT-mixed 3:1 sample exhibits a much larger current range than that with the CNTs to oCNHs of 1:4, suggesting that the capacitive behaviour of the oCNHs is limited by its electrical conductivity. Compared to 3:1 oCNHs, 5:1 and 10:1 GONRs, 1:1 oCNTs retain a similar structure with CNTs (as seen in the TEM images), i.e., a less sp^3

carbon fraction is present in the oCNTs, which can allow it, to some extent, to maintain the electrical conductivity. Besides, the oxygen-containing functional groups occurring in the 1:1 oCNTs are advantageous, as they can provide a large additional pseudo-capacitance as well as improved wettability. Although the contribution of these oxygen-containing functional groups to the pseudo-capacitance has been previously observed, the mechanism still remains somewhat uncertain. The pseudo-capacitance of oCNTs probably comes from electrochemical reactions, for example $>C-OH \leftrightarrow C=O+H^{+}+e^{-}$, etc., at the electrode interfaces.

1:1 oCNTs were also measured at the different scan rates during the potential range of -0.4-0.2 V in the H_2SO_4 electrolyte. In Figure 27c, each curve has the same form but it is apparent that the total current increases with increasing scan rate. This can be rationalised by considering the size of the diffusion layer and the time taken to record the scan. Clearly the voltammogram will take longer to record as the scan rate is decreased. Therefore the size of the diffusion layer above the electrode surface will be different depending upon the voltage scan rate used. In a slow voltage scan the diffusion layer will grow much further from the electrode in comparison to a fast scan. Consequently the flux to the electrode surface is considerably smaller at slow scan rates than it is at faster rates. As the current is proportional to the flux towards the electrode, the magnitude of the current will be lower at slow scan rates and higher at high rates.

The rate performances of CNTs and CNT-mixed oxidised samples are presented in Figure 27e. It is clear that the specific capacitance of 1:1 oCNTs is much larger than other samples at the same scan rate. With an increase of the scan rate, the capacitance of 1:1 oCNTs decreases slowly from 24.3 F/g at 50mV/s to 14.2 F/g at 800mV/s, indicating that the 1:1 oCNT sample has a good rate capability.
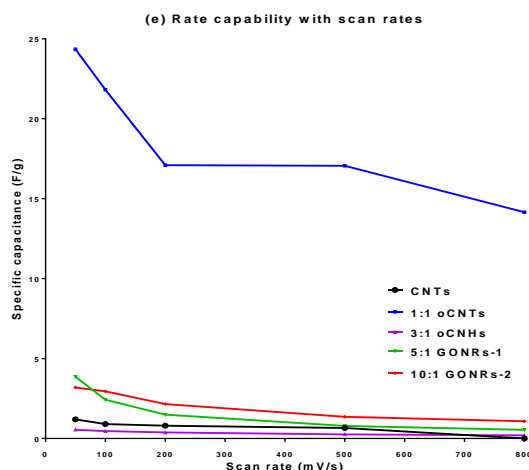
(a) All samples at the scan rate of 50mV/s

(b) All samples at a scan rate of 100mV/s

(c) 1:1 oCNTs at different scan rates

(d) Comparison of different propotions of CNTs to 3:1 oCNHs

94

Figure 27. Cyclic voltammograms of CNTs and oxidised samples using 1M H_2SO_4 electrolyte in the 3-electrode cell.

3.4 Summary

To summarise, CNTs were treated at different degrees of oxidation using the improved Hummers method and the as-produced samples were characterised by a series of instrumental analysis. It was demonstrated that the degree of consecutive tube opening in the CNTs can be controlled by adjusting the amount of oxidizing agent introduced into the system. As the oxidation process introduces carboxyl and hydroxyl functional groups, the nanoribbons show high solubility in water, ethanol and other polar organic media. Furthermore, the oxidised samples possess the high specific surface area and abundant oxygen-containing functional groups, which meet the requirements of a favourable supercapacitor electrode. However, the nanoribbons are electrically insulating due to the disrupted sp^2 bonding network, the CNTs, as a superior conductive material, were mixed with the oxidised samples proportionally, which improved the electrical conductivity of the material. It was found that the oCNTs at the oxidation level of 1:1 ($KMnO_4$: CNTs=1:1) exhibited the best capacitive performance. This research presented in this Chapter provides the structural information of all the synthesised samples and their specific electrochemical performances. The synthesised oCNTs will be used as a cathode to construct a zinc ion capacitor, which is presented in details in Chapter 4.Moreover, the 3:1 oCNHs, which possess a hybrid structure of the CNTs and the carbon nanoribbons, will be used as the electrodes to fabricate a symmetric capacitor, as described in Chapter 5.

3.5 References

[1]   Kosynkin D V, Higginbotham AL, Sinitskii A, Lomeda JR, Dimiev A, Price BK, et al. Longitudinal unzipping of carbon nanotubes to form graphene nanoribbons. Nature 2009;458:872–6.

[2]   Xu B, Yue S, Sui Z, Zhang X, Hou S, Cao G, et al. What is the choice for supercapacitors: graphene or graphene oxide? Energy Environ Sci 2011;4:2826.

Chapter 4 A Metal-ion Capacitor with Oxidised Carbon Nanotubes and Metallic Zinc Electrodes

4.1 Introduction

Climate change and depletion of fossil fuel have forced human beings to explore sustainable and regenerative energy resources and their conversion and storage. Since the stable production of renewable electricity remains a large obstacle from intermittent wind and solar sources, various electrical energy storage technologies have attracted significant research interest so far. Supercapacitors, also called electrochemical capacitors (ECs), are such high-performance energy storage devices with excellent power capability, short charge-discharge time, long cyclic life and outstanding reversibility.[1] Charge storage in supercapacitors is principally based on either the pure electrostatic charge accumulation at the electrode-electrolyte interface, i.e. electrical double layer capacitance, or the fast and reversible Faradaic processes on the electrode surface, i.e. pseudo-capacitance. However, ECs store electrical charge only at the electrode surface rather than within the entire electrode so that they deliver lower energy densities compared with batteries.[2]

In conventional symmetric ECs, carbonaceous materials, such as activated carbon, carbon nanotubes (CNTs), graphene materials and carbon aerogels, are normally used as the electrodes because of the large specific surface area, good conductivity, high chemical stability and low cost.[3-7] However, they exhibit a lower capacitance, as only electrical double layer behaviour occurs in the system. In asymmetric ECs, one or two pseudo-capacitive electrodes are incorporated to give a higher capacitance. Electroactive polymers can provide the large pseudo-capacitance.[8, 9] But their swelling behaviour degrade the cycling stability. Due to their higher pseudo-capacitance than carbon electrodes, transition metal oxide electrodes have also been used as an alternative, although their stability and conductivity are inferior to those of carbons.[10]

Driven by the need to maintain the power capability as well as enhance the capacitance and energy density performance, hybrid electrochemical capacitors (HECs)

with a different asymmetric configuration have been developed in recent years.[11] HECs are generally composed of a battery-type Faradaic anode as an energy source and a capacitor-type cathode as a power source, which can enhance the energy and power capabilities. A particular sample is lithium-ion capacitors (LICs), which combine Li-alloying anodes with supercapacitor cathodes.[12, 13] However, LICs suffer from high cost of lithium because of the scarcity in earth crust. Thereafter sodium-ion capacitors (SICs) emerge as an attractive alternative of Li-ion capacitors for the sake of the relative abundance of sodium.[14] Nevertheless, safety issue is a critical concern for either LICs or SICs because the metal anodes are extremely reactive and the organic solvents are flammable. Consequently, there is an urgent need to search for environmental friendly alternative aqueous metal-ion capacitors.

Zinc as a safe, cost-effective and eco-friendly metal is widely used in zinc-air and zinc-alkaline batteries.[15, 16] A new type of zinc-ion batteries that are based on the shuttling of Zn^{2+} ions between the zinc anode and MnO_2 cathode was reported recently.[17, 18] Herein, we report a zinc ion capacitor (ZIC) using a CNT-based pseudo-capacitive cathode and a zinc anode. Both liquid electrolyte and gel electrolyte containing $ZnSO_4$ were developed for this ZIC. Because of their high electrical conductivity, good mechanical strength and large surface area,[19, 20] CNTs are selected as the base cathodic materials. We found that the oxidised CNTs (oCNTs) can increase the pseudocapacitance due to the interaction between the oxygen-containing functional groups and the Zn^{2+}, thereby enhancing the capacitance of the ZIC.

4.2 Experimental Section

4.2.1 Materials

Carbon nanotubes were commercially purchased. All other chemicals, including 32% hydrochloric acid, 98% sulphuric acid, potassium permanganate, 30% hydrogen peroxide solution, 5 wt.% Nafion solution, zinc sulfate and polyvinyl alcohol (PVA), were purchased from Sigma–Aldrich.

4.2.2 Synthesis of oxidised carbon nanotubes

The CNTs were treated with 20% HCl solution to dissolve metal impurities. The purified CNTs were washed with sufficient deionised (DI) water and dried in an oven at 60℃. Subsequently, the oCNTs were prepared by using an improved Hummer's oxidation as follows.[21] Firstly, 1.0 g of purified CNTs was added into 120 mL of 98% concentrated H_2SO_4 and 1.0 g of $KMnO_4$ was then added slowly put into the suspension at room temperature upon magnetic stirring. The solution was maintained at room temperature for 15 min and then transferred to a 60℃ bath for a continuous stirring of 4 hours. After cooling to room temperature, 300 mL aqueous solution containing 10 mL 30% H_2O_2 solution was slowly poured into the mixture and stirred for 1 hour. The reacted solution was centrifuged (8000 rpm for 30 min), and the supernatant was decanted away. The recovered sample was re-dispersed in the DI water using bath sonication and then collected by centrifugation at 10000 rpm for 30 min. This process (the re-dispersion in the DI water and collection by centrifugation) was repeated until the pH turned to be neutral. Finally, the resultant sample was dried in the oven at 60℃, which was noted as oCNTs.

4.2.3 Characterisations

Transmission electron microscopy (TEM) images of CNTs and oCNTs were collected from the Tecnai F20 field emission transmission electron microscope. X-ray photoelectron spectroscopy (XPS) was performed using a Thermo Scientific K-Alpha spectrometer with Al Kα radiation. Raman spectra were obtained on a Renishaw inVia Raman Microscope from 800 to 3600 cm^{-1} using a green excitation laser (Ar, 514 nm). X-ray diffraction (XRD) was carried out on a PANalytical Xpert Multipurpose diffraction System with a Cu Kα source. Fourier transform infrared (FTIR) spectroscopy was performed on the Varian 640 FTIR Spectrometer with a sensitive liquid nitrogen-cooled MCT detector. Scanning electron microscopy (SEM) was performed on the NanoSEM 230 field-emission scanning electron microscope.

4.2.4 Electrochemical measurements

50 mg of CNTs and oCNTs were separately dispersed in a 10 mL of 0.5 wt.% Nafion solution using a probe sonication. Then 200 μL of CNTs or oCNTs dispersion was drop-cast onto a titanium foil separately as a working electrode. The electrochemical

properties of CNTs and oCNTs were evaluated by using a three-electrode cell: a Pt counter electrode, a Hg/HgSO$_4$ reference electrode in saturated K$_2$SO$_4$ solution, and a CNT or oCNT working electrode stabilised in 1M ZnSO$_4$ aqueous electrolyte (pH=4.16) or in pH=4.16 H$_2$SO$_4$ electrolyte at the scan rates of 10, 50, 100, 200, 500 and 800 mV s^{-1} within −1.4-0.2 V. Subsequently, a ZIC was constructed by using a zinc foil as the anode and the oCNTs as the cathode. The electrochemical performance of the ZIC was measured in 1M ZnSO$_4$ liquid electrolyte and in ZnSO$_4$-PVA gel electrolyte at the scan rates of 5, 10, 20, 50, 100, 150, 200 and 500 mV s^{-1} within 0 − 1 V or 0 − 1.8 V. The gel electrolyte was prepared by soaking a filter paper into the 0.05 g mL^{-1} PVA solution overnight and then soaking the gel-treated filter paper into the 1M ZnSO$_4$ solution overnight. In order to highlight the superiority of the ZIC, a symmetric capacitor with oCNTs as both electrodes was constructed using 1M ZnSO$_4$ aqueous electrolyte and measured at 50 mV s^{-1} within 0 − 1.8 V. Moreover, the cycling stability of the liquid- and gel-electrolyte ZICs was tested individually within 0 − 1.8 V by cycling 5 times at 5 mV s^{-1} and then 1000 times at 500 mV s^{-1}. This unit process of cycling test was continuously repeated for 5 times. The electrochemical impedance spectroscopy (10 mHz – 10 kHz, 5 mV) was used to study the ZICs at the open circuit voltage (OCV).

4.3 Results and Discussion

4.3.1 Surface-enabled Zn ion storage

Since cyclic voltammetry is a suitable technique to characterise the capacitive behaviour of electrode materials, the electrochemical performances of oCNTs and CNTs were studied in a three-electrode cell by using cyclic voltammetry. Figure 28 exhibits the cyclic voltammograms (CV) of the oCNTs (green line) and the CNTs (black line) in 1M ZnSO$_4$ aqueous solution between − 1.4 and 0.2 V (vs. Hg/HgSO$_4$ in concentrated K$_2$SO$_4$ electrolyte) at the scan rates of 10 and 200 mV s^{-1}. The −1.4 V (vs. Hg/HgSO$_4$) was the equilibrium potential of Zn^0/Zn^{2+} (Supporting information, Figure S1). The CV curves of CNTs show a typical rectangular shape, indicating pure electric double layer capacitive behaviour. However, the CV curves of oCNTs show a quasi-rectangular shape with a broad anodic hump at 0.2 V and a cathodic hump at −0.25 V, implying the presence of pseudocapacitance. The capacitive performance of oCNTs is far superior to that of CNTs which shows typical electric double layer capacitance. Moreover, the oCNTs exhibited distinct pseudo-capacitive response at higher scan rates (Supporting information, Figure S2). Additionally, as the pH of the 1M ZnSO$_4$

solution is 4.16, the pseudo-capacitance could partially include the protonation capacitance. The oCNT sample was then tested in pH=4.16 H_2SO_4 solution in order to determine the contribution of protonation to the capacitance. At the same concentration of H^+, the oCNTs in a pH=4.16 H_2SO_4 solution (Figure 28, red line) present an inferior capacitive behaviour than that in $ZnSO_4$ solution, suggesting that the presence of Zn^{2+} ions could contribute to higher capacitance.
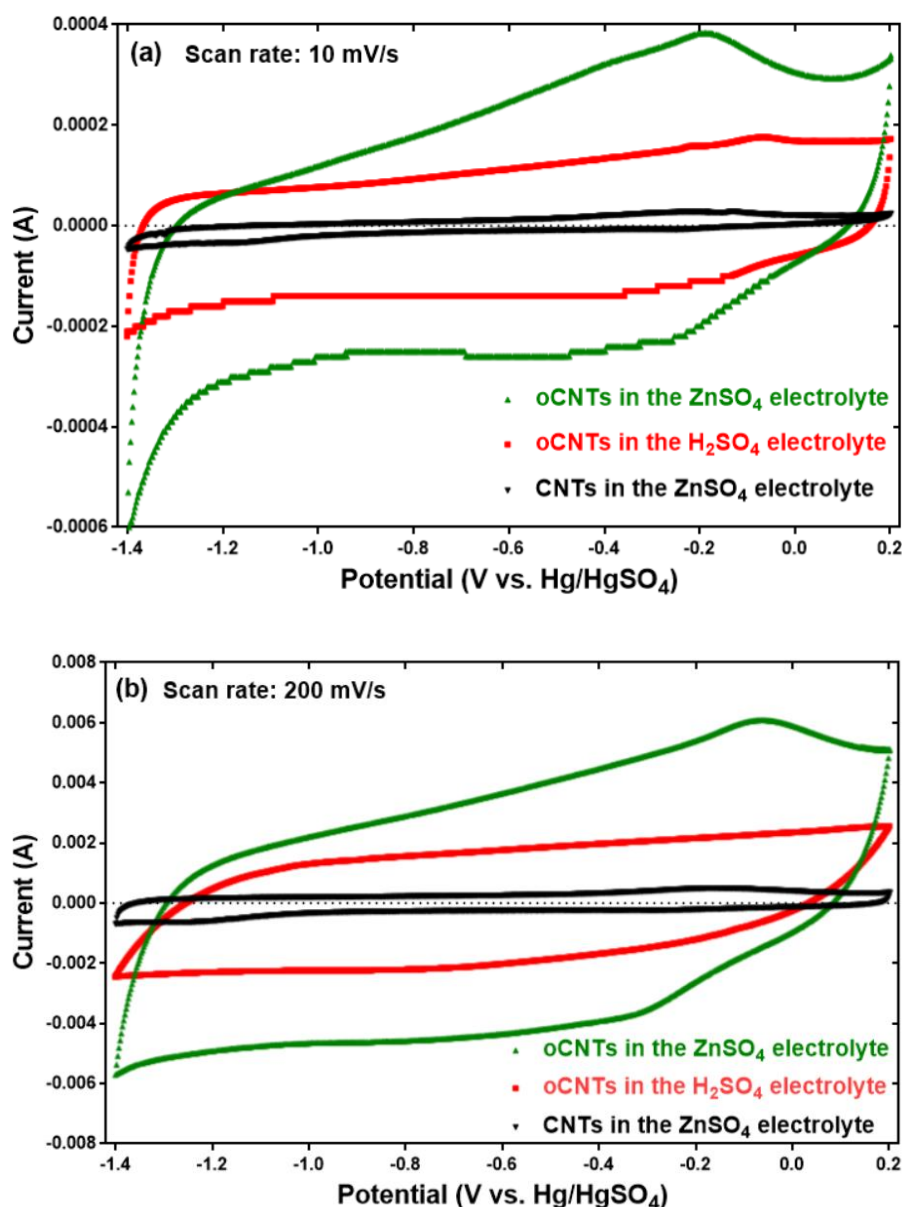

Figure 28. The CV profiles of oCNTs and CNTs recorded in 1M $ZnSO_4$ and pH=4.16 H_2SO_4 electrolytes at (a) 10 mV s^{-1} and (b) 200 mV s^{-1}.

It is worth noting that the atomic percentage of the Zn^{2+} ions on the oCNTs during discharge (Zn^{2+} adsorption) is higher than that during charge (Zn^{2+} desorption), as shown in the Table S1 in Supporting Information. In the process of discharge, certain Faradaic reaction or electrochemical adsorption of the Zn^{2+} ions on oCNTs could take place, increasing the amount of Zn^{2+} ions on the oCNTs. The charge process could involve reversible electrochemical desorption of Zn^{2+} ions that decrease the atomic percentage of Zn^{2+} ions on the oCNTs.

4.3.2 Charge storage mechanism of oCNTs

In order to understand the relationship between Zn^{2+} ion storage and physicochemical properties of the oCNTs, various instrumental analyses were conducted to reveal the structural differences of oCNTs from CNTs. XPS, as one of the surface analytical techniques, provides useful information on the nature of the functional groups and also on the presence of structural defects on the nanotube surfaces. Figure 29a displays the XPS survey spectra of CNTs and oCNTs. Merely C1s and O1s peaks, without any signals of elemental impurities, are observed. The ratios of the peak intensity indicate the change in the oxygen content of the samples. Obviously, the O-to-C ratio of the oCNTs is enhanced, which suggests an increase in the oxygen amount. The high resolution C1s core-level spectra of both samples are presented in Figure 29b. The pristine CNT sample exhibits an asymmetric peak centered at 284.5 eV with a long tail extended to the higher energy region, representing the graphitic structure. It has been demonstrated that this peak feature is ascribed to many-electron interactions of the metallic conduction electrons, which are induced by low energy electron-hole excitations through absorbing X-rays.[22] Deconvolution of the C1s peak of the oCNTs also shows a main peak at 284.5 eV, attributed to the non-oxygenated sp^2 carbon.[23, 24] Moreover, a peak at 285.1 eV is caused by sp^3-hybridised carbon. The peaks at 286.7, 288.1 and 289.3 eV correspond to carbon atoms attached to different oxygen-containing moieties, which are assigned to C-O, C=O, and O-C=O bonds, respectively. Additionally, because the O1s photoelectron kinetic energies are lower than those of the C1s, the O1s sampling depth is smaller so that the O1s spectra are slightly more surface specific. Therefore, the information of the O1s spectra can complement the analysis information of C1s spectra. Deconvolution of the XPS O1s of both samples are shown in Figure 29c. The O1s spectra are deconvoluted into two peaks and these

two peaks at 531.6 and 533.4 eV are assigned to C=O and C-O respectively, which confirm the presence of some carboxylic and hydroxyl functionalities on the nanotube surface.[23]

Additionally, Figure 29d shows the FTIR spectra of CNTs and oCNTs, which further confirm the introduction of oxygen functionalities onto the CNTs. The characteristic peaks at 2934 cm^{-1} and 2850 cm^{-1} are normally recognised as the asymmetric stretching and the symmetric stretching of C−H, respectively. The vibration of C−H stretch is still visible in the oCNT spectrum, suggesting that ordered graphitic domains remain in the structure.[25] The major contribution of oCNTs to the FTIR spectra is the oxygen-containing functional groups. Near 3430 cm^{-1} in the high frequency area, there is a broad peak for the oCNTs at 3000–3700 cm^{-1} as compared with that of the CNTs, which is caused by the stretching vibration of hydroxyl groups.[26] Correspondingly, the absorption peak based on the bending vibration of -OH at 1584 cm^{-1} becomes stronger. Besides, the absorption peak occurring near 1650 cm^{-1} in the medium frequency area is caused by the stretching vibration of C=O of carboxylic acid and carbonyl groups. Finally, the absorption peaks at 1384 cm^{-1} and 1118 cm^{-1} arise from the vibration of C-O of carboxylic acid and the stretching vibration of C-OH, respectively.
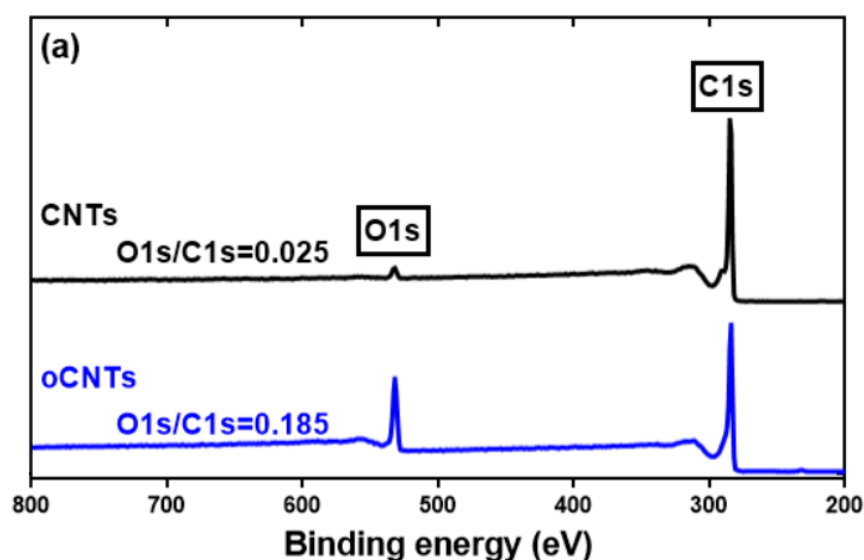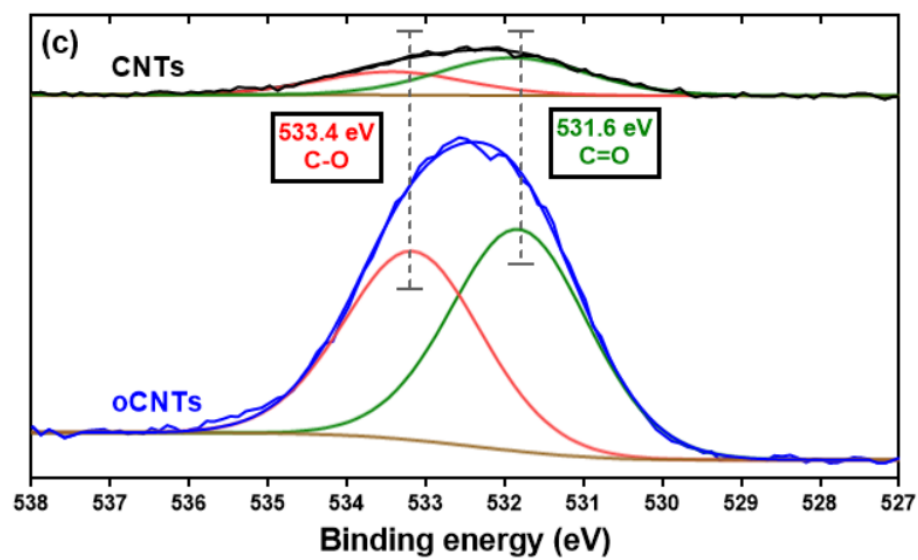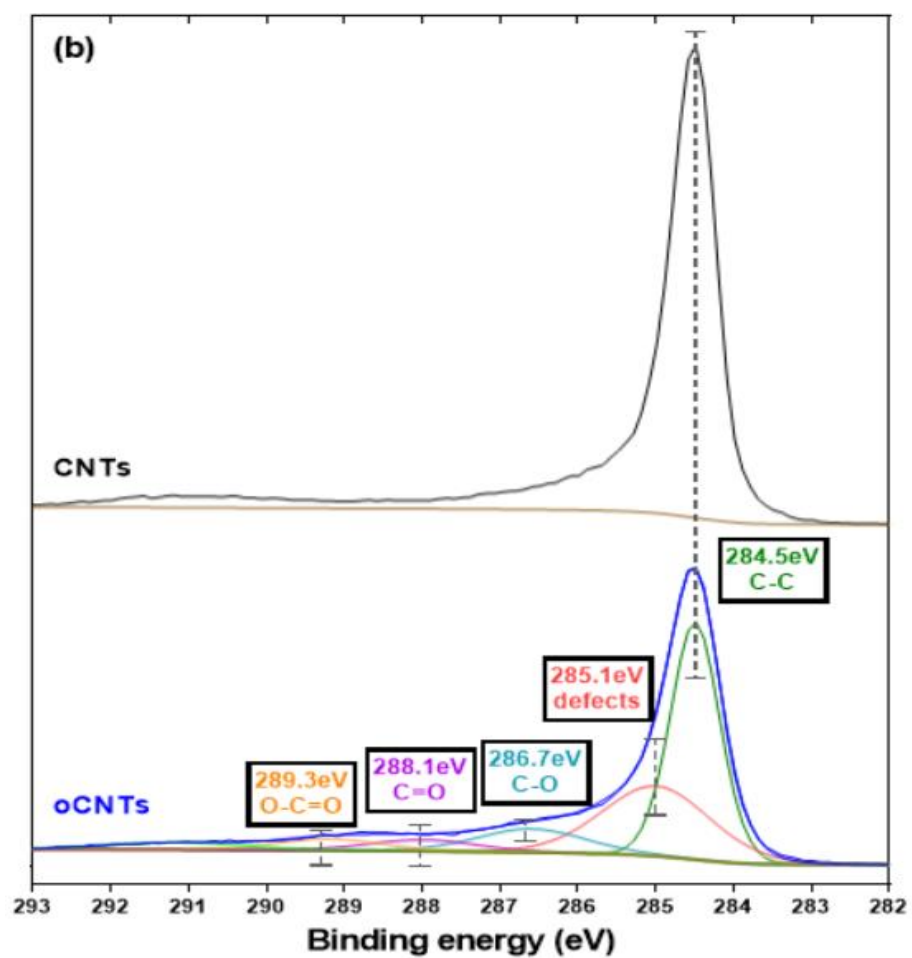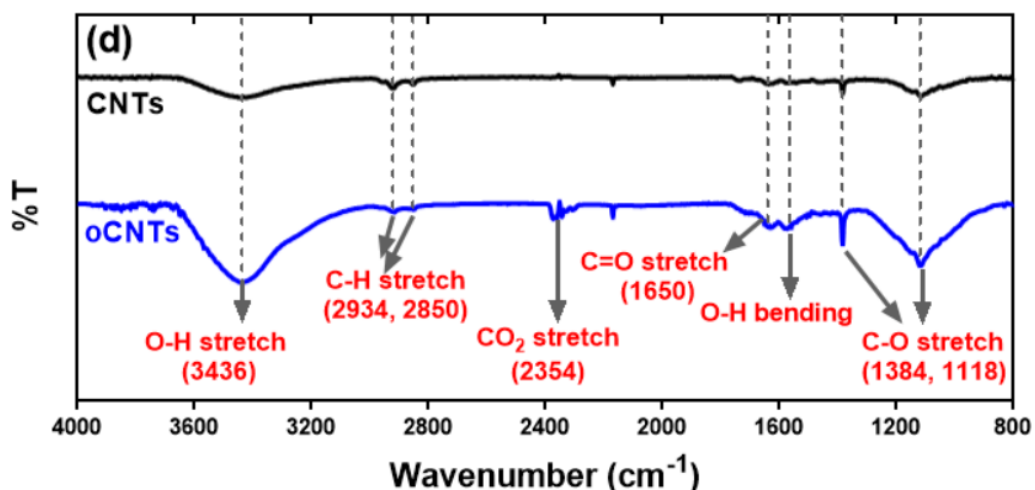
Figure 29. (a) XPS survey spectra; (b) XPS C1s spectra; (c) XPS O1s spectra; and (d) FTIR spectra of CNTs and oCNTs.

The TEM images provide the microstructural information of CNTs and oCNTs, as presented in Figure 30 a-d. The morphology of the oCNTs did not change significantly after low-level oxidation (Figure 30c, d). But it is noticeable that, as seen in the areas pointed by the arrows in Figure 30b, the oCNTs were not as graphitic as the CNTs, evidenced by the amorphous fragments attached on the surfaces. Since the degree of oxidation effectively determines the extent of the CNT unzipping[21], at the low oxidation level, the amorphous carbon was formed on the surface of the oCNTs with intact graphitic inner tube remaining. The TEM images are further supported by Raman and XRD results.

Raman spectroscopy is a non-destructive technique that is widely used to study the structure of carbon-based materials. Figure 30e displays the Raman spectra for CNTs and oCNTs. Basically, the main features in the Raman spectra of graphitic carbon materials are the D (1354 cm^{-1}), G (1584 cm^{-1}) and 2D (2707 cm^{-1}) bands.[27] To be specific, G band represents the ideal crystal graphite structure and is caused by the stretching vibration of sp^2 type C-C bonds in the condensed ring structure of the crystal lattice graphite surface. D band signifies crystal grain size, as well as the disorderly structure and defects of carbon materials. Generally, the I_D/I_G value is used to represent the graphitic degree of the carbon materials. As shown in Figure 30e, the

I_D/I_G values of the oCNTs and the CNTs are not obviously changed, indicating that after oxidation the ordering of the graphitic structure almost remained. 2D band, which is the overtone of D band, originates from the double-resonance Raman scattering with the added involvement of double phonons. The relative intensity of 2D band to G band is inversely associated with the doping level of oxygen functional groups on the graphene basal planes.[27, 28] Figure 30e shows the I_{2D}/I_G value of the oCNTs reduces significantly as compared to that of the CNTs, which suggests a reduced sp^2 domain size due to the occupation of introduced oxygen functional groups. Thus, the Raman spectra demonstrate that the majority of the graphitic structure in the oCNTs remained intact but with the oxygen doped to the outermost layers.

Figure 30f compares XRD patterns of both samples. It can be found that the CNTs have a 2θ value of ~26.8^0 and the position of the peak of the oCNTs does not shift after oxidation treatment, which demonstrates that they have almost the same interlayered spacing. However, the peak intensity of the oCNTs is weaker than that of the CNTs, probably indicating that at such oxidation level, the outermost layers of the nanotubes have been damaged but still with the intact inner structure remaining.
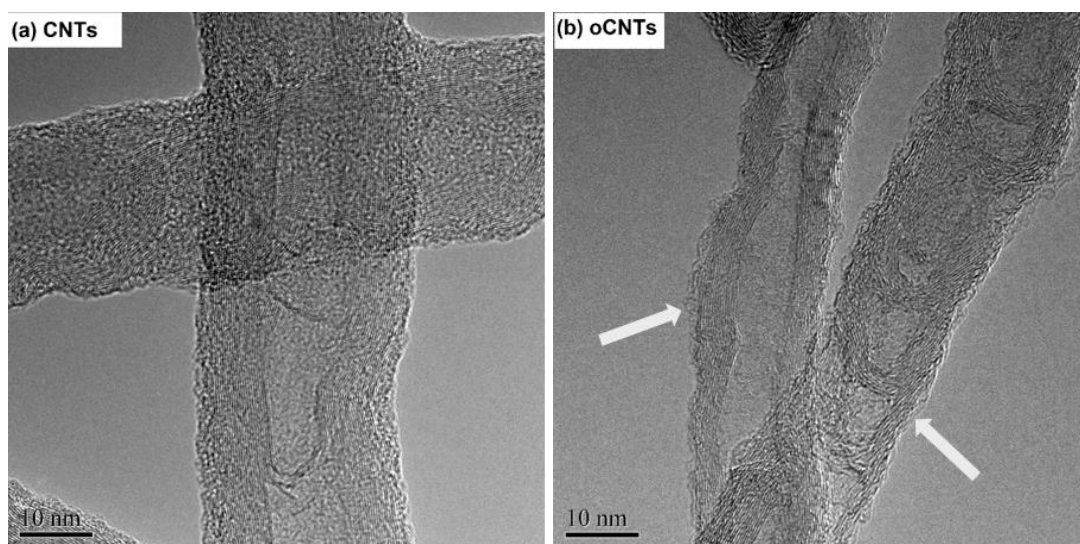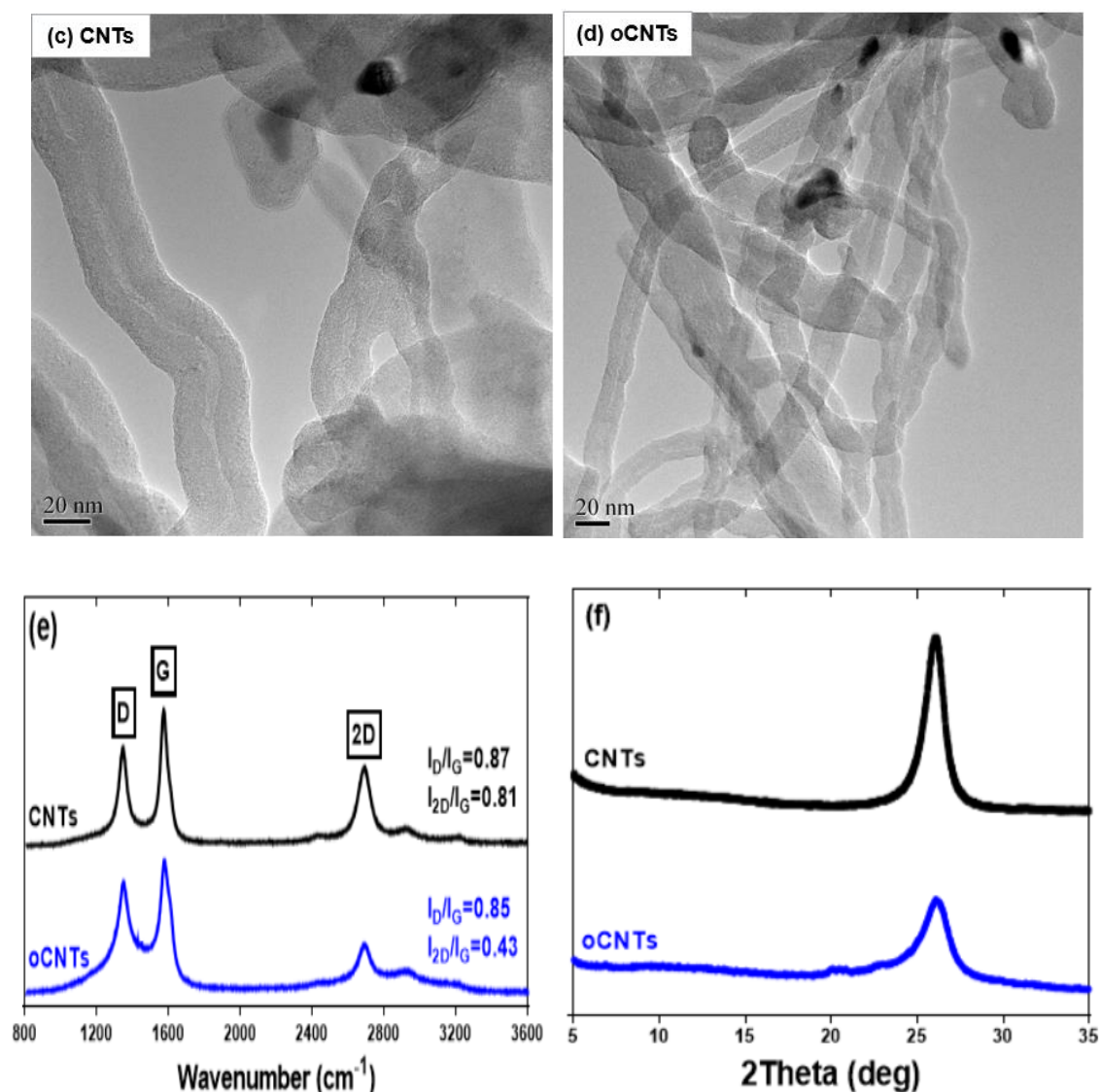
Figure 30. (a), (b), (c), (d) TEM images (the arrows point at the amorphous surface of the oCNTs), (e) Raman spectra, and (f) XRD patterns of CNTs and oCNTs.

Based on the structural analyses, the better capacitive performance of the oCNTs can be explained as follows. On one hand, despite the superior electrical conductivity, CNTs do not contain abundant oxygen functional groups, implying that its capacitive behaviour merely relies on the electric double layer capacitance. On the other hand, the poor wettability of CNTs in aqueous electrolyte, resulting from the hydrophobic surfaces, can decelerate the ion transport toward the electrode-electrolyte interfaces, thereby negatively affecting the electrochemical performance. However, the oCNTs are characterised by the abundant oxygen-containing groups at the surface and the intact

graphitic inner tubes that maintain the electrical conductivity. The oxygen functional groups occurring in the oCNTs are advantageous, as they can provide a large additional pseudo-capacitance as well as improved wettability, giving the oCNTs a higher capacitance than that of the CNTs. According to the previous report that the oxygen functional groups of graphene oxide sheets can chemically interact with divalent metal ions[29], the pseudocapacitance of oCNTs, in this case, probably comes from the electrochemical reactions, e.g. $>2C–O-Zn \leftrightarrow 2C=O+Zn^{2+}+2e^-$ and $>C–OH \leftrightarrow C=O+H^++e^-$, and partially from the electrostatic adsorption/desorption of ions, as illustrated in Figure 31. As the presence of Zn^{2+} ions provides higher capacitance, the electrochemical reaction/adsorption based on the Zn^{2+} ions and oxygen-containing groups of the oCNTs should play a dominant role in the ZIC system.
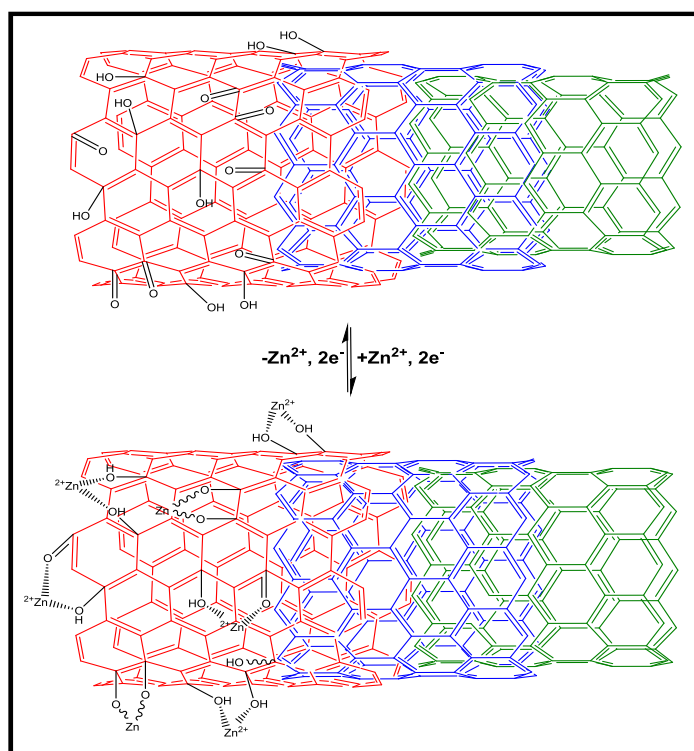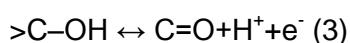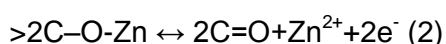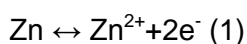

Figure 31. A schematic representing the chemistry of the oCNTs upon discharge/adsorption and charge/desorption in the Zn^{2+} electrolyte.

4.3.3 Assembly of ZIC

A safe and eco-friendly energy-storage device, which consists of an oCNT cathode, a zinc anode and a $ZnSO_4$ liquid electrolyte or a $ZnSO_4$-PVA gel electrolyte, is assembled. The $ZnSO_4$ solution is a nontoxic, noncorrosive and cost-effective mild

aqueous electrolyte and therefore the ZIC is more environmental friendly compared to other rechargeable power sources that use either alkaline (such as Zn/MnO_2, Ni–Cd, or Ni–metal hydrated batteries), or acidic (lead–acid) electrolytes.[18] The construction of this new device is probably based on the following electrochemical processes. In equation 1, zinc anode is electrochemically dissolved in the form of Zn^{2+} ions during discharging and deposited reversibly during charging. In terms of the oCNT cathode, the Zn^{2+} ions diffuse to the cathode and reversibly react with the oxygen functional groups of the oCNTs. The cathodic reactions include the electrochemical reactions between the Zn^{2+} ions and ketone groups, as depicted in the equation 2, and also include the electrostatic adsorption/desorption of Zn^{2+} ions. There could be some other ions participating in the cathode process, e.g. the contribution of protonation, as shown in equation 3.

$$Zn \leftrightarrow Zn^{2+}+2e^- \quad (1)$$

$$>2C-O-Zn \leftrightarrow 2C=O+Zn^{2+}+2e^- \quad (2)$$

$$>C-OH \leftrightarrow C=O+H^++e^- \quad (3)$$

The Zn^{2+} ions in the electrolyte participate in these processes. During discharge, Zn dissolves at the anode and meanwhile, the Zn^{2+} ions are electrochemically adsorbed/reacted with the oxygen-containing groups on the oCNT cathode. Reversely in the charge process, the electrochemical desorption of Zn^{2+} ions occurs on the oCNT cathode and the Zn^{2+} ions are reduced to Zn metal at the anode. Therefore, the Zn^{2+} ions are shuttling between the oCNT cathode and the Zn anode to transport the charges. As the charge storage mechanism relates to the migration of Zn^{2+} ions between anode and cathode, mimicking that of LICs and SICs, this device is termed as a zinc ion capacitor (ZIC).


Cyclic voltammograms of the ZICs with the $ZnSO_4$ liquid electrolyte and the $ZnSO_4$-PVA gel electrolyte at a scan rate of 50 mV s^{-1} are exhibited in Figure 32a, b with the voltage ranges of 0-1 V and 0-1.8 V. Obviously, the gel-electrolyte ZIC presents a better capacitive performance than the liquid-electrolyte one, which is also demonstrated at other scan rates as shown in the Supporting Information. The better performance of the gel-electrolyte ZIC can probably be explained in this way. As the ionic conductivity of an electrolyte affects the supercapacitor performance[30], the

PVA-based gel electrolyte principally provides a liquid-like medium for ion transport and therefore have the capability to enhance the ionic conductivity[31]. Actually, folding and unfolding the polymeric chain of the PVA cause ion dissociation that enhances the charge carrier concentration, thus a rise in ionic conductivity of the gel electrolyte can be obtained. This postulation is later verified by rate capability determination and electrochemical impedance. Moreover, the appearance of the redox peaks in Figure 32b at 1.0-1.6 V indicates that the existence of Zn^{2+} ions in the electrolyte causes a Faradaic process at the electrolyte-cathode interface. Although the mechanism of the ZIC is still uncertain, its pseudo-capacitance is probably attributed to the electrochemical reaction/adsorption and desorption of Zn^{2+} ions on the oCNT cathode.

The influence of the scan rate on the capacitive behaviour of the gel-electrolyte ZIC swept at 5-200 mV s^{-1} with the voltage range of 0-1.8 V is shown in Figure 32c. It is apparent that each CV curve has the same quasi-rectangular pattern with a broadened peak at around 1.0-1.6 V, suggesting that the oxygen-containing groups of the oCNT cathode are able to facilitate the pseudocapacitance. Also the current response is dependent on the scan rate. With an increase of the scan rate, the current is proportional to the scan rate without serious distortion in the shape of the CV curves even at the high scan rates, which demonstrates a good charge propagation behaviour and ion response of the sample [32]. Furthermore, a symmetric oCNT-based capacitor using the 1M $ZnSO_4$ aqueous electrolyte was constructed. The capacitive behaviours of the symmetric capacitor as well as the liquid-electrolyte ZIC at a scan rate of 50mV s^{-1} within 0-1.8 V are presented in Figure 32d. It is observed that the capacitive current of the ZIC is nearly two times higher than that of the symmetric capacitor. The symmetric capacitor exhibits a CV curve approximated to the ideal situation of electrical double layer capacitor, that is, there is no visible peak from a redox current over the voltage region[30]. This result indicates that the battery-supercapacitor combination configuration of the ZIC can accumulate charge through Faradaic electrochemical process so as to enhance the capacitance of the capacitor.

Additionally, rate capability is an important feature for supercapacitors. In Figure 32e and f, the specific capacitance variation with the scan rate in the range of 10-500 mV s^{-1} is illustrated (the calculation of the specific capacitance is described in Supporting

Information). It is obvious that the specific capacitance of the gel-electrolyte ZIC outperforms that with the liquid electrolyte at all scan rates, e.g. the gel-electrolyte ZIC exhibited a higher capacitance value of around 20 mF cm^{-2} than the liquid-electrolyte one (15 mF cm^{-2}) at a scan rate of 10 mV s^{-1} (Figure 5f). Also, when the scan rate was increased by 50 times, the gel-electrolyte ZIC presented a capacitance retention ratio of 42.6 %, which is higher than the retention ratio obtained from the liquid-electrolyte (the retention ratio of 25.0 %).
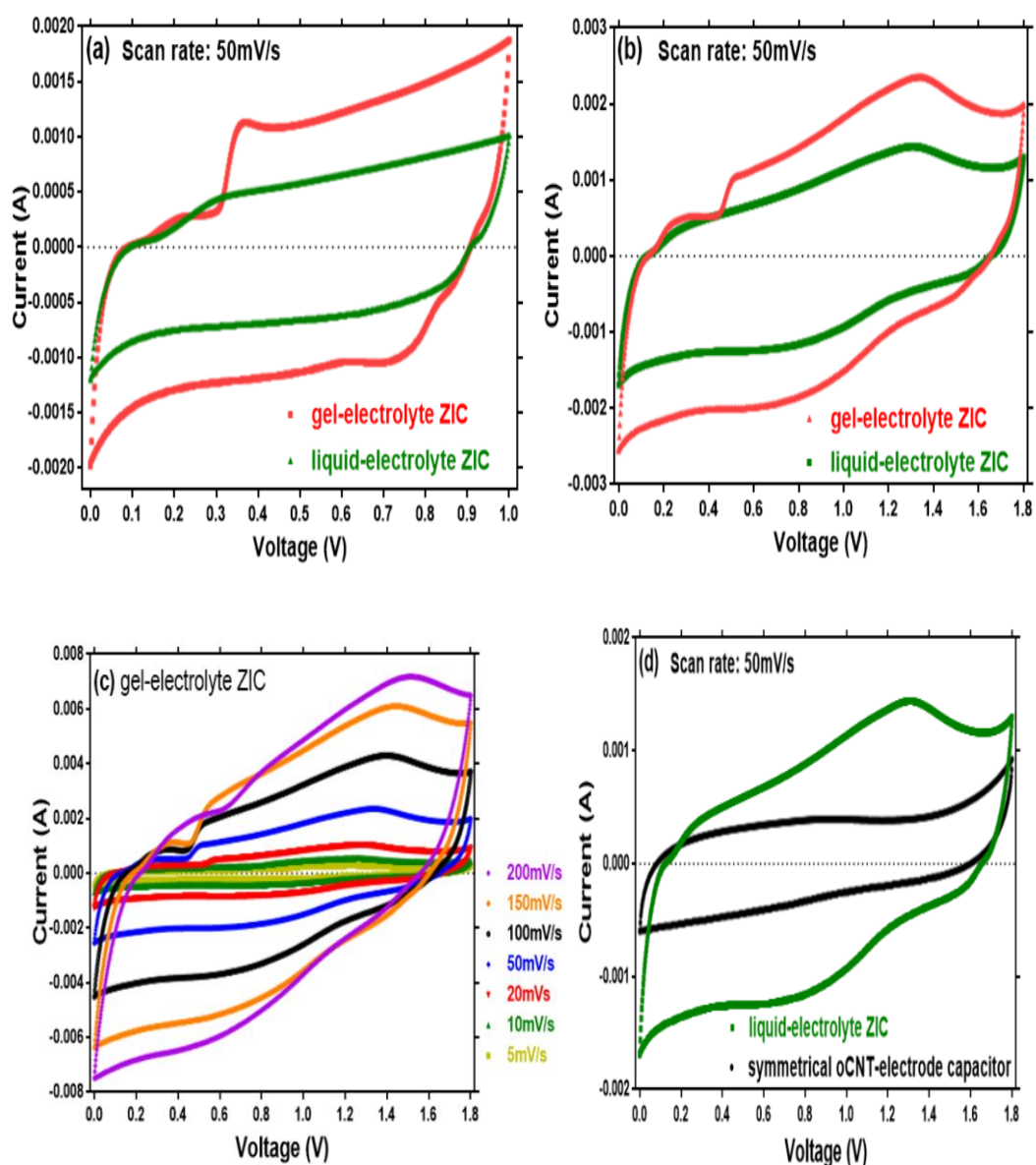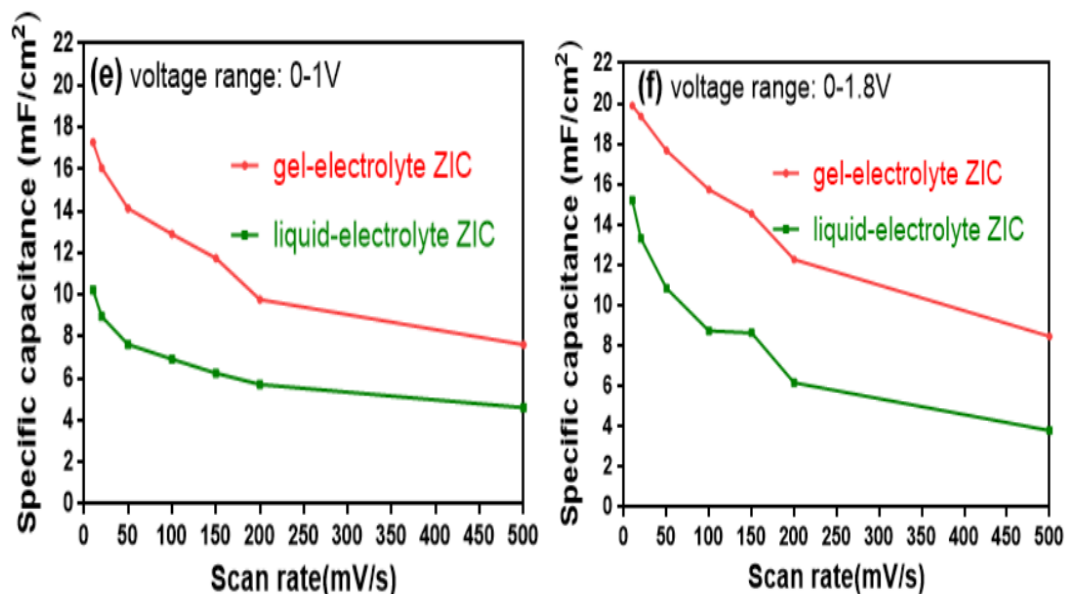
Figure 32. (a), (b) The electrochemical capacitive behaviours of gel- and liquid-electrolyte zinc ion capacitors at 50mV/s within 0-1V and 0-1.8V; (c) Cyclic voltammetry of gel-electrolyte zinc ion capacitor at different scan rates within 0-1.8V;(d) The capacitive performances of liquid-electrolyte ZIC and symmetric oCNT-based capacitor at 50mV/s within 0-1.8V; (e), (f) Rate capability of gel- and liquid-electrolyte zinc ion capacitors within 0-1V and 0-1.8V.

Electrochemical impedance spectroscopy (EIS) is an important technique to characterise the electrochemical frequency behaviour of a device and the obtained data are generally plotted in a Nyquist diagram that represents the imaginary part of the impedance versus the real part.[33] Figure 33 exhibits the Nyquist plot for two ZIC cells assembled with liquid- and gel-electrolyte. It is worth noting that at the highest frequency, the value at the real axis, called the equivalent series resistance (ESR), represents the sum of the resistance of the electrolyte and the intrinsic resistance of the electrode material. As both ZIC cells have the same electrode material, the ESR, in this case, reflects the difference of the electrolyte resistance. By comparison, the gel electrolyte exhibited a lower ESR value of 3.93 Ω than the liquid one (8.51 Ω), which should be one reason for the better capacitive behaviour of the gel-electrolyte ZIC. Furthermore, it is observed that for both ZICs, the imaginary parts of impedance at the low frequency region are nearly perpendicular to the real parts, which indicate that both electrolytes have satisfactory electrochemical capacitive behaviour[30]. The charge

transfer resistance of the gel-electrolyte ZIC is similar to that of the liquid-electrolyte one, which is deduced from the span of the single semi-circle along the real axis from high to medium frequency as shown in the close-up view of Figure 33. However, an apparent difference of both ZIC cells is found at medium frequency in the close-up, where the 45° sloped region of the Nyquist plots, the so-called Warburg resistance, can be seen. The Warburg resistant results from the frequency dependence of ion transport in the electrolyte.[32] Since the low-frequency capacitive behaviour of the liquid-electrolyte ZIC is largely shifted along the *x*-axis towards more resistive value[33], the smaller Warburg region of the gel-electrolyte ZIC indicates a lower ion diffusion resistance and less obstruction of the ion movement[32]. Thus a better charge propagation and ion response of the gel-based electrolyte are demonstrated, which can explain the better electrochemical performance of the gel-electrolyte ZIC observed in the previous results.
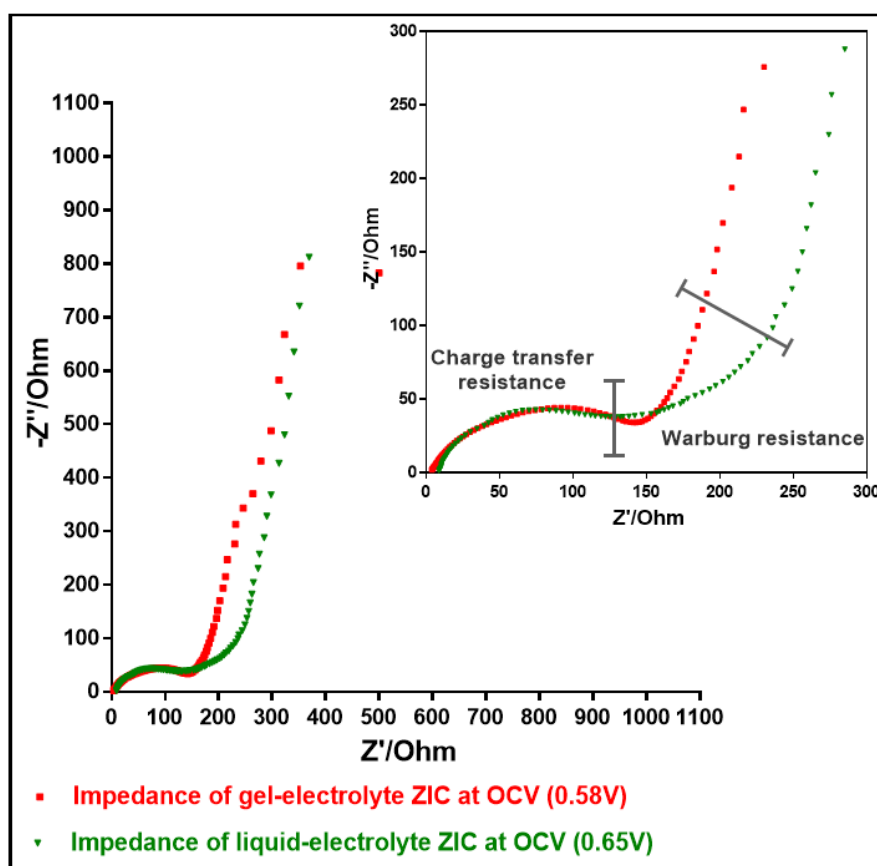

Figure 33. Electrochemical impedance spectroscopy plots of gel- and liquid-electrolyte ZIC at the Open Circuit Voltage (OCV).

The cycling stability is also a crucial concern for supercapacitor. To investigate the electrochemical stability of the ZIC, the charge-discharge cycling was performed at the alternating scan rates of 5 and 500 mV s^{-1} (Figure 34). After 5000 cycles at 500 mV s^{-1}, both liquid- and gel-electrolyte ZICs show the benign cycling stabilities, i.e., their current responses decrease slowly with the cycling numbers. This demonstrates that the pseudo-capacitance effect introduced by the electrochemical reaction/adsorption and desorption between the Zn^{2+} ions and the oxygen functional groups of the oCNT cathode is stable with cycling. However, by comparing the current responses of both ZICs, the gel-electrolyte ZIC presents higher current values than the liquid-electrolyte one, which suggests the better electrochemical capacitance behaviour of the gel-electrolyte ZIC. The inherent change of the gel-electrolyte ZIC before and after cycling was further characterised using the EIS technique with a frequency range of 0.01 Hz to 10 kHz (Figure S4, Supporting Information). The much smaller span of the single semi-circle at the high frequency for the ZIC after cycling indicates a smaller charge transfer resistance. At the low frequency region, the Nyquist plot curve of the ZIC after cycling inclines to the real axis, implying a higher ion diffusion resistance. The reduction of the ionic conductivity upon cycling might be responsible for the deterioration of the gel-electrolyte ZIC, which further explains the decrease of the current responses with the cycling numbers. Moreover, the morphology and structure of the zinc anode at different conditions were observed by SEM as shown in Figure S5. Before cycling, the original zinc foil was flat, but its surface became rougher after cycling. The uniform ripple-like zinc morphology without the formation of dendrites contributes to the favourable cycling stability of the ZIC, since the formation of dendritic zinc is accompanied with hydrogen evolution that is negative for cyclic stability[15].

(a) gel-electrolyte ZIC
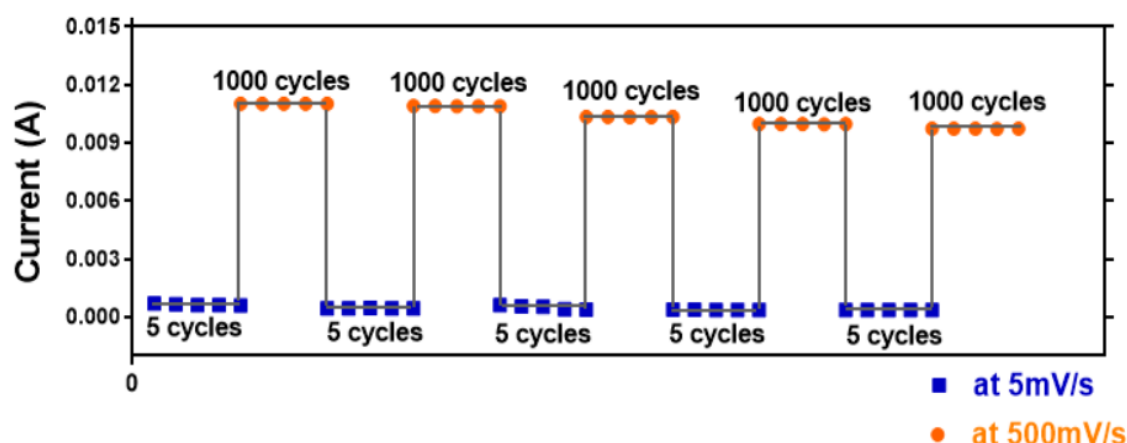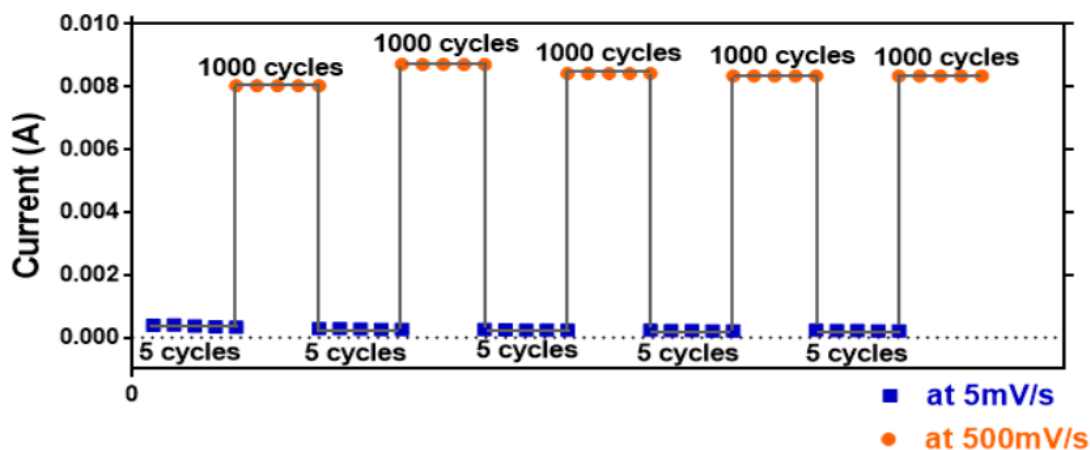

(b) liquid-electrolyte ZIC

Figure 34. (a), (b) Cycle performances of gel- and liquid-electrolyte zinc ion capacitors.

4.4 Summary

A ZIC was assembled by using a zinc anode, an oCNT cathode and a $ZnSO_4$-based electrolyte. The low cost zinc metal and the nontoxic, noncorrosive $ZnSO_4$ solution (pH = 4.5) make the ZIC to be a cost-effective and environmentally friendly device. Due to the electrochemical adsorption/desorption of Zn^{2+} ions on the oxygen-containing groups of the oCNT cathode, the pseudocapacitive behaviour observed in this ZIC delivered a specific capacitance of 20 mF cm^{-2} at a scan rate of 10 mV s^{-1}. Additionally, this ZIC was stable during a long cycling test (up to 5000 cycles). This work demonstrated a proof-of-concept ZIC and showed that the oxygen functionalities of the oCNTs contributed to the pseudo-capacitance.

4.5 Supporting Information

The equilibrium potential of Zn^0/Zn^{2+} is presented in Figure S1. The oCNTs exhibited the best pseudo-capacitive response at various scan rates, as shown in Figure S2.
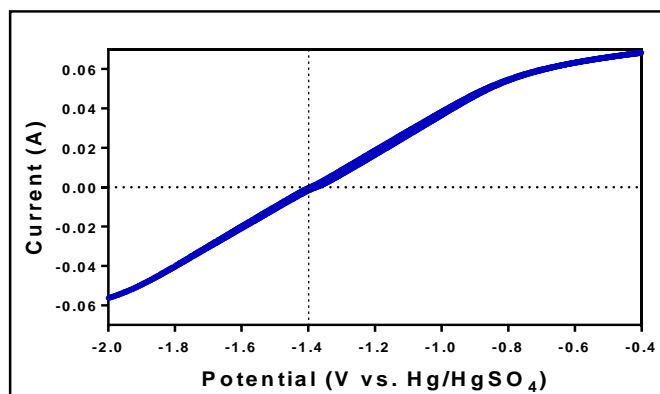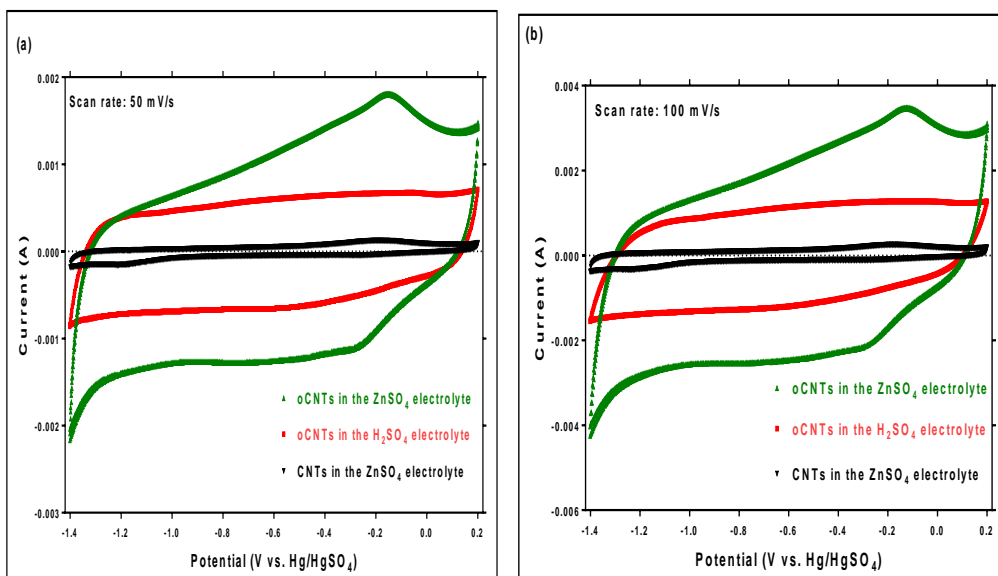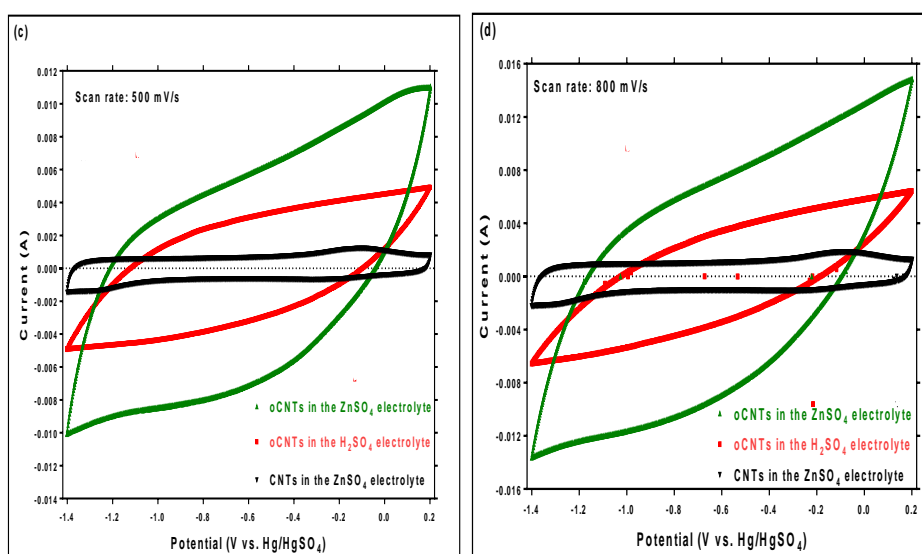

**Figure S1.** Equilibrium potential of Zn^0/Zn^{2+}.

Figure S2. The electrochemical capacitive behaviour of the oCNT and the CNTs in 1M ZnSO$_4$ aqueous electrolyte and the oCNT in the H$_2$SO$_4$ electrolyte at the scan rates of (a) 10mV/s, (b) 100mV/s, (c) 500mV/s, and (d) 800mV/s.

XPS was used to determine the atomic percentage of Zn^{2+} ions on the oCNTs during charge and discharge, as shown in the below tables. As the ZnSO$_4$ electrolyte can affect the amount of Zn^{2+} ions, the samples in Table 1b were rinsed by deionised water to remove the ZnSO$_4$ solution, but the samples in Table 1a were without rinsing.

Table a	Atomic percentage (%) of Zn^{2+} ions on the oCNTs	
Element name	**During discharge** (Zn^{2+} adsorption)	**During charge** (Zn^{2+} desorption)
C	23.50	52.70
O	51.68	33.35
S	7.61	3.31
Zn	17.22	8.74

Table b	Atomic percentage (%) of Zn^{2+} ions on the oCNTs	
Element name	During discharge (Zn^{2+} adsorption)	During charge (Zn^{2+} desorption)
C	48.86	57.68
O	37.96	31.03
S	2.52	1.65
Zn	10.67	8.29

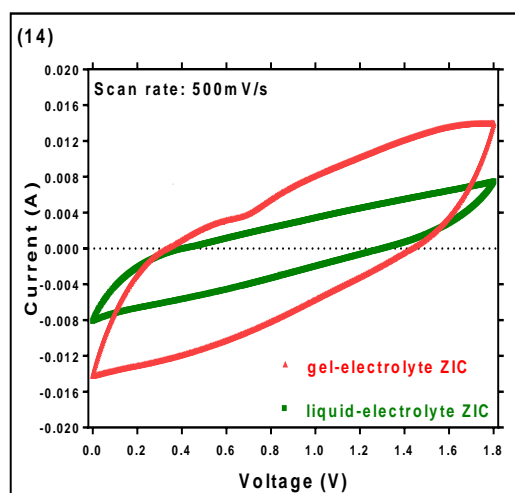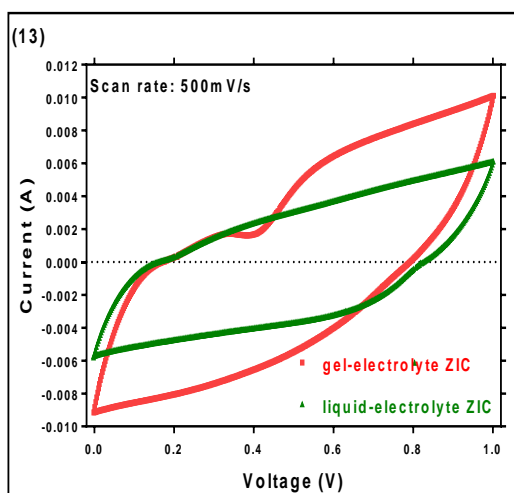Table S1. Atomic percentage of Zn^{2+} ions on the oCNTs (a) without rinsing and (b) rinsing with deionised water.
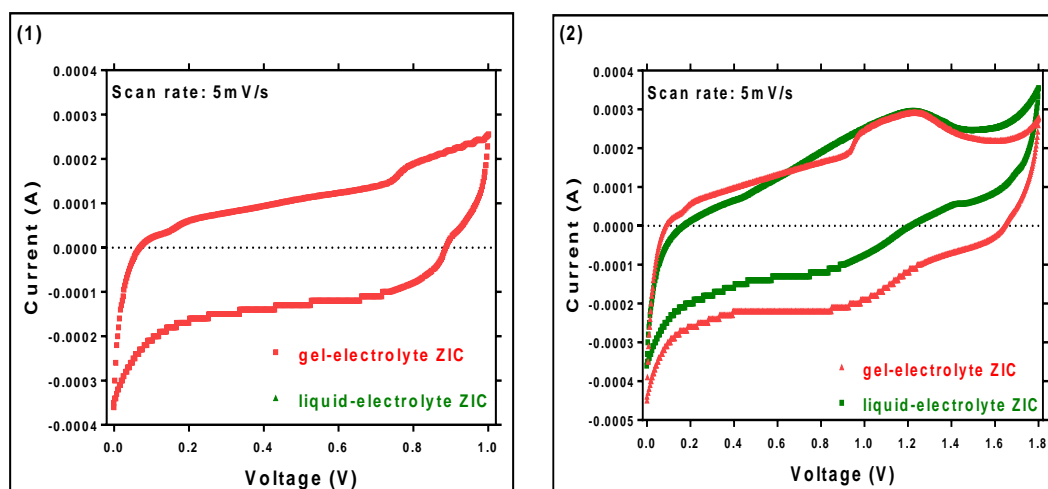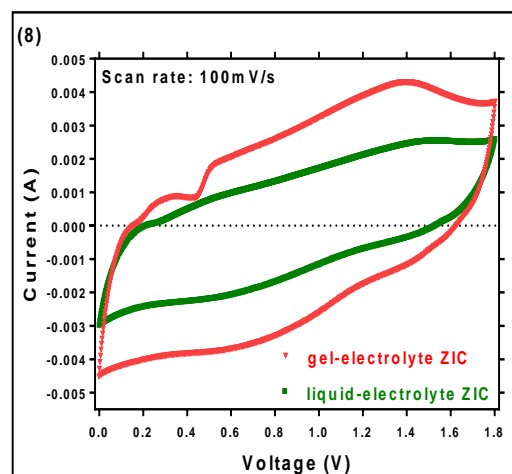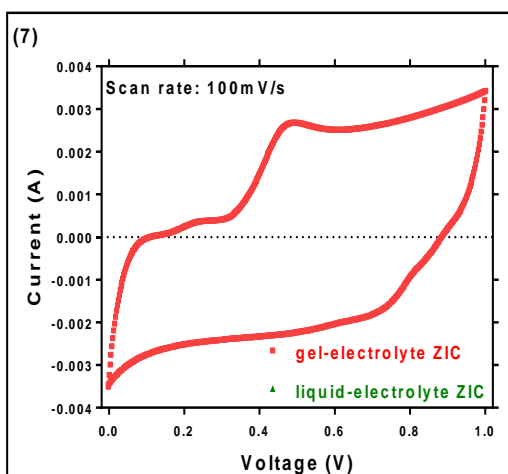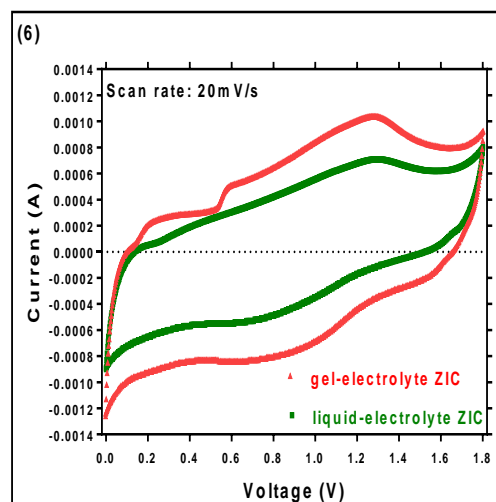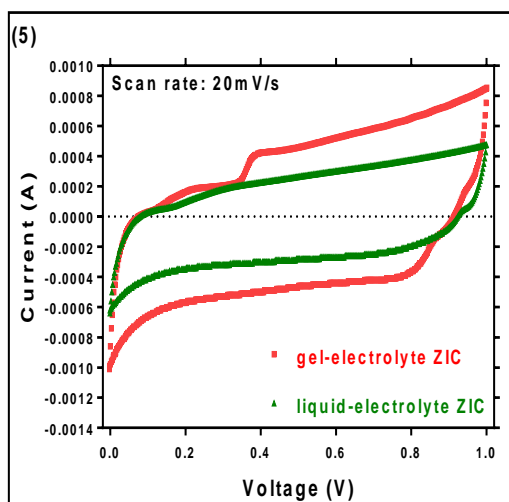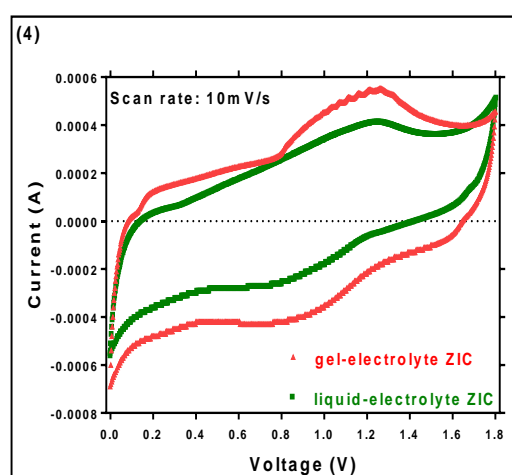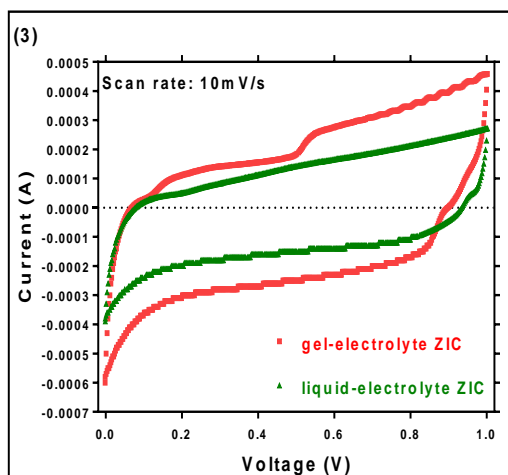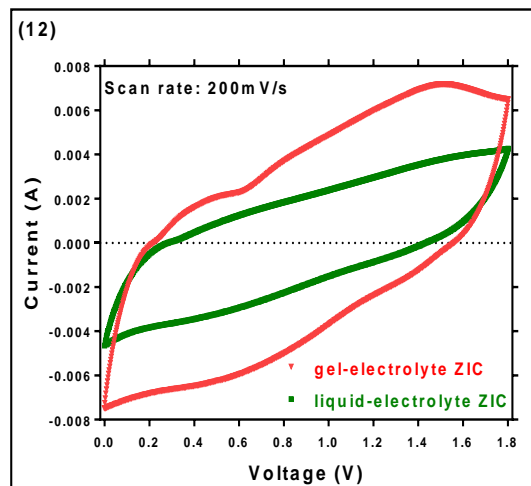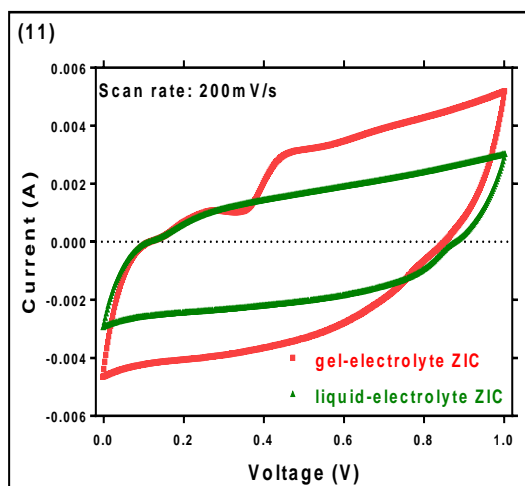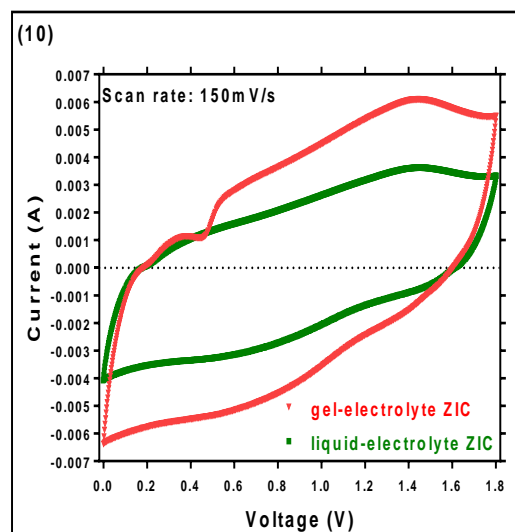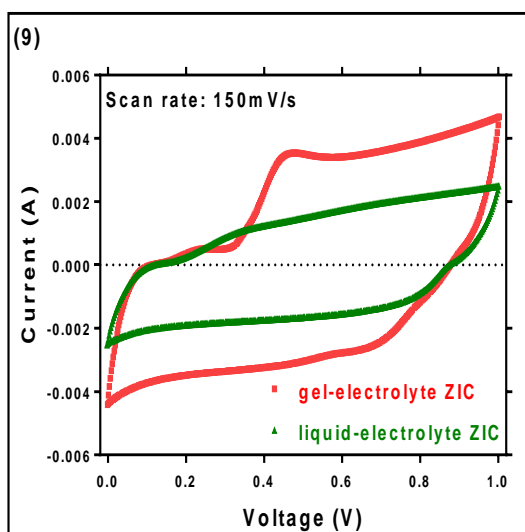
Figure S3. The capacitive performances of gel- and liquid-electrolyte zinc ion capacitor at different scan rates within 0-1V and 0-1.8V.

The specific capacitance was calculated according to the following equations:

$$C = \frac{Q}{V} = \frac{It}{V} = \frac{I}{V/t} = \frac{I}{scan\ rate}$$

$$SC = \frac{C}{A}$$

C=capacitance (F);

I=current (A);

V=voltage (V);

t=time (s);

SC=specific capacitance (mF/cm^2);

A=area of the electrode (diameter is 0.92 cm).

The capacitance, in the thesis, was simply obtained from dividing the current by scan rate. The maximum current at each scan rate is selected. To be specific, the current values at 1V with the voltage range of 0-1V and those at 1.3V within 0-1.8V were used to calculate the corresponding specific capacitance.

The inherent change of the gel-electrolyte ZIC before and after cycling was characterised by using the EIS technique with a frequency range of 0.01 Hz to 10 kHz, as shown in Figure S4. The much smaller span of the single semi-circle at the high frequency for the ZIC after cycling indicates a smaller charge transfer resistance. At the low frequency region, the Nyquist plot curve of the ZIC after cycling inclines to the real axis, implying a higher ion diffusion resistance.

Figure S4. The Nyquist plot curves of gel-electrolyte ZIC at the Open Circuit Voltage (OCV) before and after cycling.

Figure S5. SEM images of zinc anode at different conditions: pristine (a and b), after cycling in the gel-electrolyte ZIC (c and d), and after cycling in the liquid-electrolyte ZIC (e and f).

4.6 References
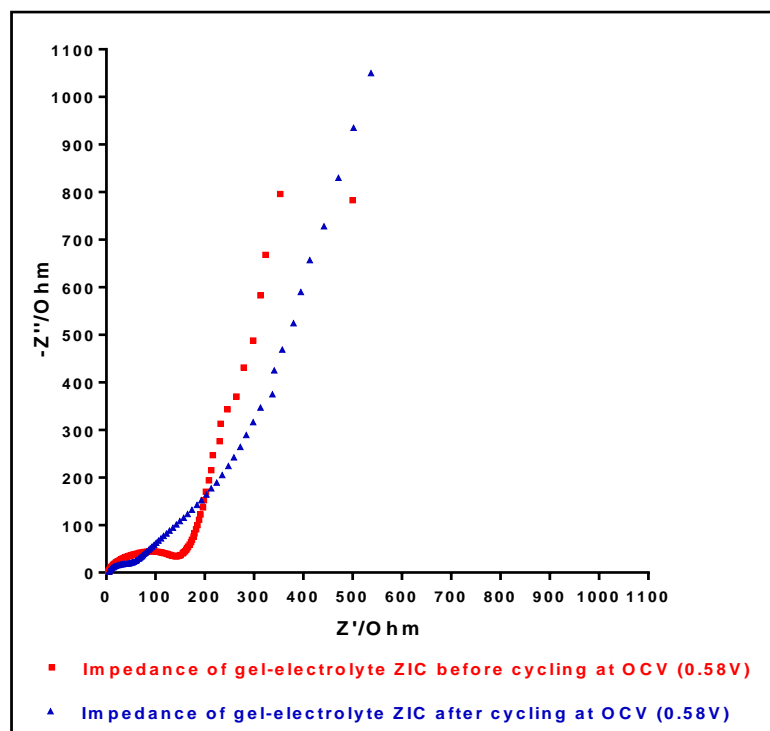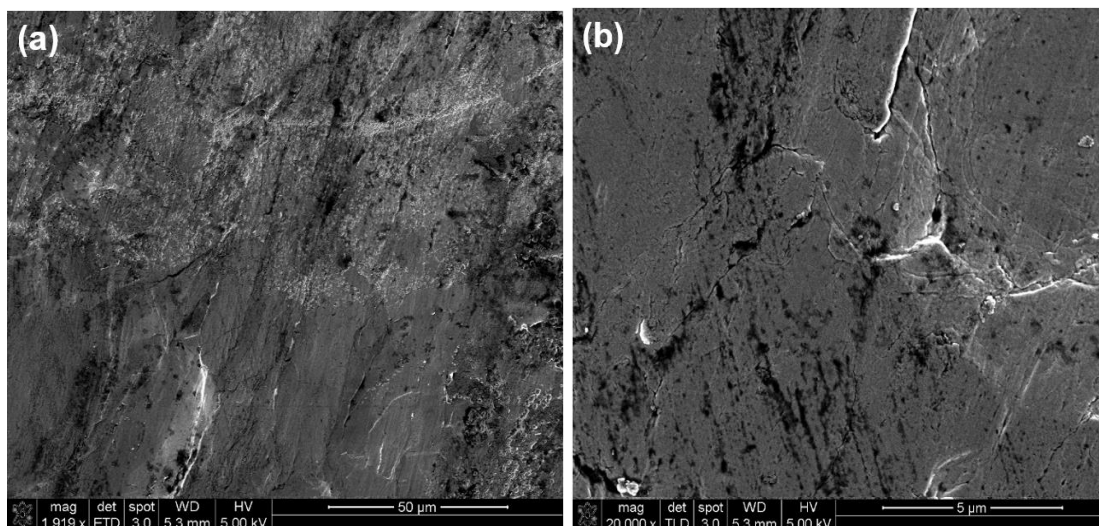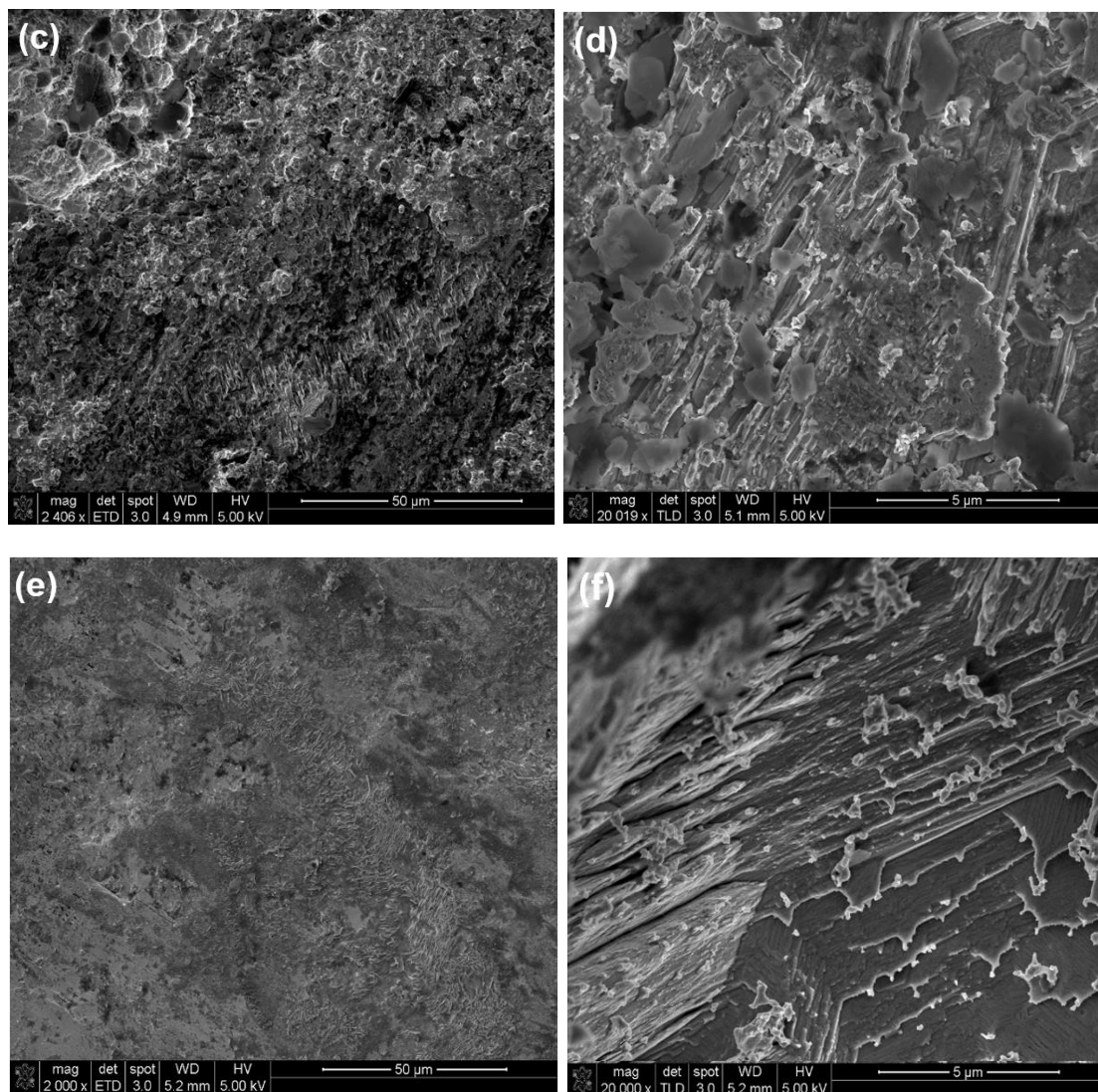
[1]   Yan J, Wang Q, Wei T, Fan Z. Recent Advances in Design and Fabrication of Electrochemical Supercapacitors with High Energy Densities. Adv Energy Mater. 2014;4(4):1-43.

[2]   Dubal DP, Ayyad O, Ruiz V, Gomez-Romero P. Hybrid energy storage: the merging of battery and supercapacitor chemistries. Chem Soc Rev. 2015;44(7):1777-90.

[3]   Frackowiak E. Carbon materials for supercapacitor application. Phys Chem Chem Phys. 2007;9(15):1774-85.

[4]   Pandolfo AG, Hollenkamp AF. Carbon properties and their role in supercapacitors. J Power Sources. 2006;157(1):11-27.

[5]   Elzbieta Frackowiak FB. Electrochemical storage of energy in carbon nanotubes and nanostructured carbons. Carbon. 2002;40(10):1775–87.

[6]   Vix-Guterl C, Frackowiak E, Jurewicz K, Friebe M, Parmentier J, Béguin F. Electrochemical energy storage in ordered porous carbon materials. Carbon. 2005;43(6):1293-302.

[7]   Zhang LL, Zhou R, Zhao XS. Graphene-based materials as supercapacitor electrodes. J Mater Chem. 2010;20(29):5983.

[8]   Kurra N, Wang R, Alshareef HN. All conducting polymer electrodes for asymmetric solid-state supercapacitors. J Mater Chem A. 2015;3(14):7368-74.

[9]   Snook GA, Kao P, Best AS. Conducting-polymer-based supercapacitor devices and electrodes. J Power Sources. 2011;196(1):1-12.

[10]   Lokhande CD, Dubal DP, Joo O-S. Metal oxide thin film based supercapacitors. Curr Appl Phys. 2011;11(3):255-70.

[11]   Simon P, Gogotsi Y. Materials for electrochemical capacitors. Nat Mater. 2008;7(11):845-54.

[12]   Cao WJ, Shih J, Zheng JP, Doung T. Development and characterization of Li-ion capacitor pouch cells. J Power Sources. 2014;257:388-93.

[13]   Cao WJ, Greenleaf M, Li YX, Adams D, Hagen M, Doung T, et al. The effect of lithium loadings on anode to the voltage drop during charge and discharge of Li-ion capacitors. J Power Sources. 2015;280:600-5.

[14]   Zheng Chen VA, Xilai Jia, Qiangfeng Xiao, Bruce Dunn, Yunfeng Lu. High-Performance Sodium-Ion Pseudocapacitors Based on Hierarchically Porous Nanowire Composites. ACS nano. 2012;6(5):4319-27.

[15]   Trocoli R, La Mantia F. An aqueous zinc-ion battery based on copper hexacyanoferrate. ChemSusChem. 2015;8(3):481-5.

[16]   Jia Z, Wang B, Wang Y. Copper hexacyanoferrate with a well-defined open framework as a positive electrode for aqueous zinc ion batteries. Mater Chem Phys. 2015;149-150:601-6.

[17]   Ghaemi M, Amrollahi R, Ataherian F, Kassaee MZ. New advances on bipolar rechargeable alkaline manganese dioxide–zinc batteries. J Power Sources. 2003;117(1-2):233-41.

[18]   Xu C, Li B, Du H, Kang F. Energetic zinc ion chemistry: the rechargeable zinc ion battery. Angew Chem Int Ed Engl. 2012;51(4):933-5.

[19]   Kay Hyeok An WSK, Young Soo Park,, Young Chul Choi SML, Dong Chul Chung,, Dong Jae Bae SCL, and Young Hee Lee. Supercapacitors Using Single-Walled Carbon Nanotube Electrodes. Adv Mater 2001;13(7):497–500.

[20]   Zhai Y, Dou Y, Zhao D, Fulvio PF, Mayes RT, Dai S. Carbon materials for chemical capacitive energy storage. Adv Mater. 2011;23(42):4828-50.

[21]   Kosynkin DV, Higginbotham AL, Sinitskii A, Lomeda JR, Dimiev A, Price BK, et al. Longitudinal unzipping of carbon nanotubes to form graphene nanoribbons. Nature. 2009;458(7240):872-6.

[22]   Datsyuk V, Kalyva M, Papagelis K, Parthenios J, Tasis D, Siokou A, et al. Chemical oxidation of multiwalled carbon nanotubes. Carbon. 2008;46(6):833-40.

[23]   Stankovich S, Dikin DA, Piner RD, Kohlhaas KA, Kleinhammes A, Jia Y, et al. Synthesis of graphene-based nanosheets via chemical reduction of exfoliated graphite oxide. Carbon. 2007;45(7):1558-65.

[24]   Yang D, Velamakanni A, Bozoklu G, Park S, Stoller M, Piner RD, et al. Chemical analysis of graphene oxide films after heat and chemical treatments by X-ray photoelectron and Micro-Raman spectroscopy. Carbon. 2009;47(1):145-52.

[25]   Pham VH, Cuong TV, Hur SH, Oh E, Kim EJ, Shin EW, et al. Chemical functionalization of graphene sheets by solvothermal reduction of a graphene oxide suspension in N-methyl-2-pyrrolidone. J Mater Chem. 2011;21(10):3371-7.

[26]   Wang D-W, Wu K-H, Gentle IR, Lu GQ. Anodic chlorine/nitrogen co-doping of reduced graphene oxide films at room temperature. Carbon. 2012;50(9):3333-41.

[27]   Wu K-H, Wang D-W, Gentle IR. Revisiting oxygen reduction reaction on oxidized and unzipped carbon nanotubes. Carbon. 2015;81:295-304.

[28]   Ferrari AC. Raman spectroscopy of graphene and graphite: Disorder, electron–phonon coupling, doping and nonadiabatic effects. Solid State Commun. 2007;143(1-2):47-57.

[29]   Park S, Lee K-S, Bozoklu G, Cai W, Nguyen ST, Ruoff RS. Graphene oxide papers modified by divalent ions - Enhancing mechanical properties via chemical cross-linking. ACS nano. 2008;2(3):572-8.

[30]   Yu H, Wu J, Fan L, Xu K, Zhong X, Lin Y, et al. Improvement of the performance for quasi-solid-state supercapacitor by using PVA–KOH–KI polymer gel electrolyte. Electrochim Acta. 2011;56(20):6881-6.

[31]   Agrawal SL, Awadhia A. DSC and conductivity studies on PVA based proton conducting gel electrolyte. Bulletin of Materials Science. 2004;27(6):523-7.

[32]   Zhang LL, Zhao S, Tian XN, Zhao XS. Layered graphene oxide nanostructures with sandwiched conducting polymers as supercapacitor electrodes. Langmuir. 2010;26(22):17624-8.

[33]   Taberna PL, Portet C, Simon P. Electrode surface treatment and electrochemical impedance spectroscopy study on carbon/carbon supercapacitors. Appl Phys A. 2005;82(4):639-46.

Chapter 5 A Symmetric Solid-State Supercapacitors based on Oxidised CNT Electrodes

5.1 Introduction

Supercapacitors have high power density, good cycling stability, long cell and shelf lives [1-4], and are promising power systems to meet the future needs. Under the quick development of lightweight, large-area and portable electronics, supercapacitors with high flexibility have attracted much attention. Solid-state supercapacitors have presented high potential for their use as flexible power counterparts for wearable and portable electronics, such as rollup displays, electronic papers and wearable systems for personal multi-media [5-8].

A variety of nanostructured materials have been explored for the development of solid-state supercapacitors, including carbon nanotubes (CNTs) [9-13], graphene [14-21], carbon nanofibres (CNFs) [22, 23], conductive polymers [24-28] and some metal oxides [29-31]. Among these materials, carbon-based nanomaterials, especially CNTs and graphene, have been found to be promising materials for solid state supercapacitors, owing to their large surface area, excellent optical, mechanical and electrochemical properties [4, 32, 33].

Some high-performance solid state supercapacitors based on CNTs and graphene have been reported [9-21]. However, studies also show that the electrochemical performance of solid-state supercapacitors based on CNTs and graphene are not always satisfactory. One of the main reasons for this limitation is attributed to the lack of active sites for charge storage. To address this issue, recent effort has led to the development of functionalised graphene sheets with various functional groups, such as -H, -N, -Br, -Cl, -I, -COOH and $-SO_3H$, attached to the edge and basal plane through various solution processing or self-assembly methods [34-37]. These functional groups are electrochemical active sites and give rise to high capacitance with high rate capability.

In this work, we employed an improved Hummer's oxidation method to oxidise the multi-walled CNTs to obtain oxidised carbon nanohybrids (oCNHs) and graphene oxide nanoribbons (GONRs) [38]. We demonstrated the assembly of oCNHs with cellulose membranes as free-standing electrodes for high-performance solid-state supercapacitors, in which the cellulose membrane was soaked with a H_2SO_4/polyvinyl alcohol (PVA) gel electrolyte. The optimum electrochemical performance was acquired at an areal capacitance (i.e. capacitance per unit of area) of ~75 mF/cm^2 at 5 mV/s with an excellent charge-discharge cycling stability.

5.2 Experimental Section

5.2.1 Materials

Multi-walled carbon nanotubes (CNTs) were provided by Chengdu Organic Chemicals Co. Ltd., China. 30% hydrogen peroxide (H_2O_2) and 20% hydrogen chloride (HCl) were purchased from Chem-supply. Poly(vinyl alcohol) (PVA) was sourced from Aldrich. Potassium permanganate ($KMnO_4$) was obtained from Poison. 98% concentrated sulphuric acid (H_2SO_4) was acquired from RCL Labscan. Except for CNTs which were purified to remove the metal impurities, all other chemicals were used without any further purification. Milli-Q water produced from Millipore's Milli-Q Integral Water Purification System was used for solution preparation.

5.2.2 Synthesis of Oxidised Carbon Nanohybrids (oCNHs) and Graphene Oxide Nanoribbons (GONRs)

After the purification of CNTs using HCl solution, an improved Hummer's oxidation method was used to prepare oxidised CNT samples with different degrees of oxidation [38]. The degree of oxidation was controlled by varying the $KMnO_4$:CNTs mass ratios. A mass ratio of 3:1 gave a hybrid material consisting of both tubular (unopened CNTs) and exfoliated (unzipped CNTs or ribbon-like graphene oxides) structures. For this reason, the oxidised CNT sample with a 3:1 degree of oxidation was named as oxidised carbon nanohybrids (oCNHs). A mass ratio of 10:1 delivered fully unzipping of the tubes, resulting in ribbon-like graphene oxides. Owing to this reason, the oxidised CNT sample with a 10:1 degree of oxidation was named as graphene oxide

nanoribbons (GONRs). The experimental procedures for the synthesis of oCNHs and GONRs were exactly the same, except for the mass ratios of $KMnO_4$:CNTs used.

5.2.3 Assembly of oCNHs-cellulose membranes

The electrodes based on oCNHs and cellulose membrane were prepared by using a vacuum filtration technique. In this work, different mass ratios of CNTs (purified) were added to oCNHs in order to determine the optimum mass ratio for the best electrochemical performance of the solid-state supercapacitors. For all mass ratios, a total mass of 50 mg for CNTs and oCNHs was dispersed in water to produce a 1 mg/ml solution. Electrode films with five different mass ratios of CNTs to oCNHs were prepared, including 50CNTs, 40CNTs-10oCNHs, 25CNTs-25oCNHs, 10CNTs-40oCNHs and 50oCNHs.

5.2.4 Preparation of Gel Electrolytes

The gel (H_2SO_4/PVA) electrolyte was prepared by mixing 0.1 g of PVA with 1 ml of 1 M H_2SO_4 solution.

5.2.5 Fabrication of Flexible Supercapacitors

Solid-state supercapacitors were fabricated by using two as-prepared oCNHs-cellulose membranes serving as both electrodes and separators. The H_2SO_4/PVA polymer gel electrolyte was absorbed into the cellulose membrane.

5.2.6 Electrochemical Performance Analysis

The electrochemical performance of the supercapacitors was tested by using a two-electrode system with the electrode diameter of 8mm. Cyclic voltammograms (CV) were obtained at different scan rates, ranging from 5 mV/s to 200 mV/s, in the voltage range of 0 V to 0.8 V.

5.2.7 Characterisations

The structural properties of CNTs, oCNHs and GONRs were studied by transmission electron microscopy (TEM), X-ray diffraction spectroscopy (XRD), Raman

spectroscopy (Raman), fourier transform infrared spectroscopy (FTIR) and X-ray photoelectron spectroscopy (XPS). The structural properties of the electrode films were studied by scanning electron microscopy (SEM). TEM images were obtained from the Tecnai F20 field emission transmission electron microscope. XRD spectra were collected from a PANalytical Xpert Multipurpose diffraction System with a Cu Kα source. Raman spectra were obtained from a Renishaw inVia Raman Microscope from 800 to 3600 cm^{-1} using a green excitation laser (Ar, 514 nm) with 10% of the maximum power. FTIR spectra were determined on a Varian 640 FTIR Spectrometer with a sensitive liquid nitrogen-cooled MCT detector. XPS was performed on a Thermo Scientific K-Alpha spectrometer with an Al Kα radiation. SEM images were collected from a NanoSEM 230 field-emission scanning electron microscope.

5.3 Results and Discussion

5.3.1 Structural Analysis

Figure 35 a-d display the TEM images of the pristine CNTs and the oxidised CNT samples with different degrees of oxidation. As shown in Figure 35a, the pristine CNTs have a hollow structure with both inner and exterior surfaces remaining intact. Figure 35b shows a TEM image of GONRs. Under a 10:1 oxidative condition, CNTs were fully unzipped to form graphene oxide with a ribbon-like structure. Figure 35 c and d are TEM images of oCNHs. Clearly, oCNHs show both tubular and exfoliated structures. The tubular structure is attributed to the unopened or intact CNTs, while the exfoliated structure results from unzipped or scissored CNTs. The chemical nature of the exfoliated structure is the same as graphene oxide. It is evident that the structure of the oxidised products can be tuned by varying the KMnO$_4$:CNTs mass ratios. Figure 35e provides a scheme that illustrates the formation of oCNHs and GONRs under a 3:1 and 10:1 mass ratios of KMnO$_4$:CNTs, respectively.
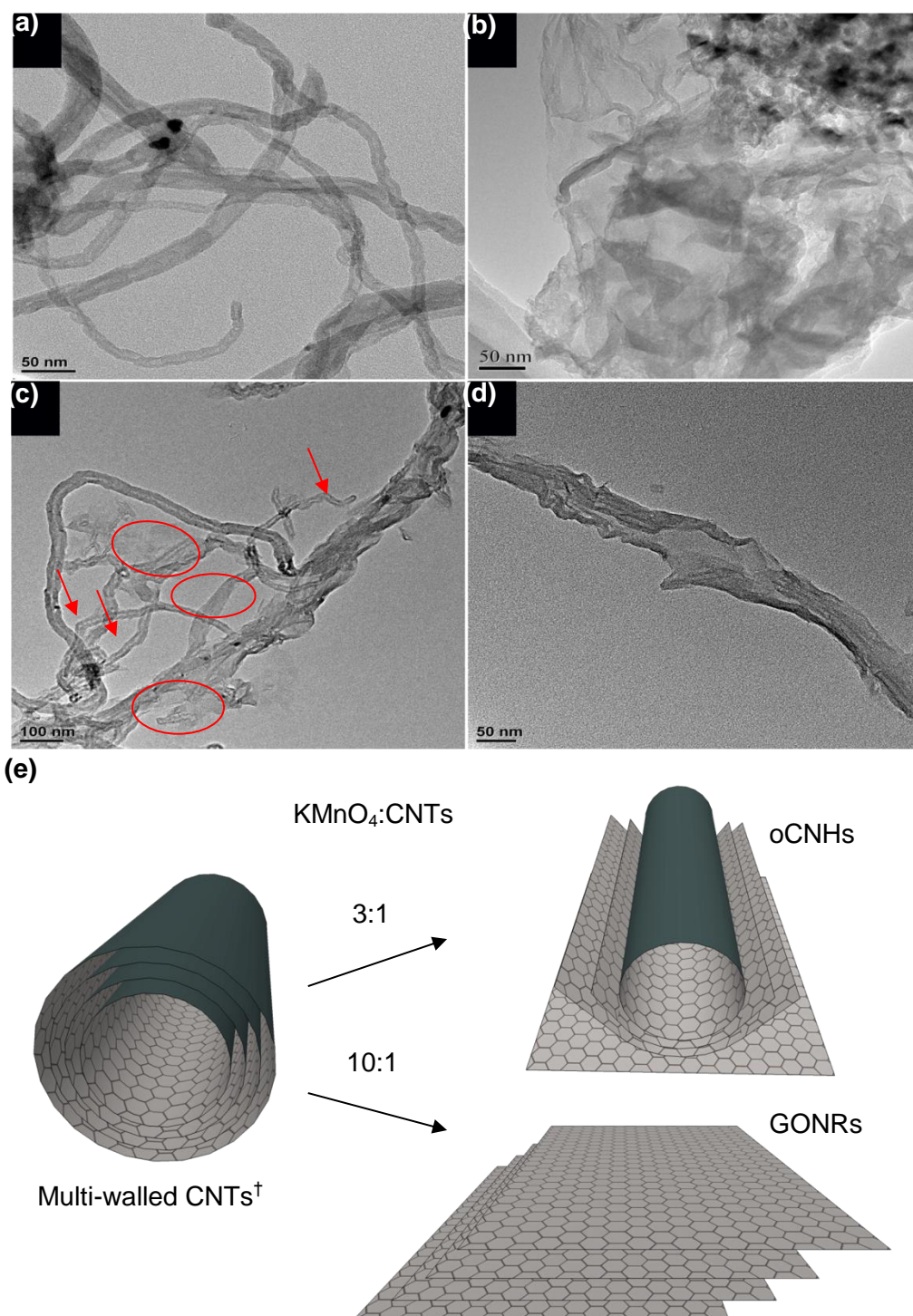
Figure 35. (a-d) TEM images of (a) CNTs, (b) GONRs and (c-d) oCNHs; (e) a scheme illustrating the formation of oCNHs and GONRs. [†]The model for multi-walled CNTs is adapted from [39].

XRD was employed to investigate the interlayer spacing of the multi-walled CNTs and the samples with different degrees of oxidation (i.e. oCNHs and GONRs). The XRD spectra of CNTs, oCNHs and GONRs are presented in Figure 36a. As shown from the XRD profile of CNTs, the raw CNTs exhibit a very strong characteristic (002) diffraction peak at 2θ value of ~26^0, reflecting that the pristine multi-walled CNTs have a layered graphitic structure [40]. After the oxidation with a $KMnO_4$:CNTs mass ratio of 3:1, the (002) peak experienced a dramatic decline for oCNHs; however, a new peak came up at 2θ value of ~11.2^0. The presence of two peaks implies that the oCNH is a hybrid material consisting of both tubular structure (partially unzipped CNTs) and exfoliated structure (fully unzipped CNTs). The decreased intensity of (002) peak was attributed to the partial oxidation of the multi-walled CNTs, meaning that the outermost layers started unzipping; while the inner structures remained intact. The appearance of a second peak at 2θ value of ~11.2^0 was due to the formation of ribbon-like graphene oxide, caused by the complete oxidation/unzipping of the multi-walled CNTs. The decrease in 2θ value also indicates an increase in interlayer spacing, suggesting that the ribbon-like graphene oxide has a larger interlayer spacing than that of the original CNTs, due to the intercalation of oxygen functional groups and water molecules into the graphite layers during the oxidation process [41].

By further increasing the degree of oxidation to 10:1, the (002) peak totally disappeared for GONRs; however, a new peak formed at 2θ value of ~10.3^0. This suggests that the multi-walled CNTs were fully unzipped under a 10:1 oxidation condition. However, the 2θ value for GONRs of the newly formed peak is slightly smaller than that of the corresponding peak for oCNHs (~11.2^0), meaning that GONRs have an even larger interlayer spacing than that of oCNHs. This is not surprising as the GONRs have undergone a more severe oxidation and more oxygen-containing functional groups should have penetrated into the graphite layers, which results in a larger expansion of graphite layers [38]. The results revealed by XRD analysis conform to the structural information shown by the TEM images.

Raman spectroscopy is a non-destructive technique that has been widely used to identify the defects in the sp^2-network of graphene [42]. Defect-free sp^2 graphene usually displays two modes of band, which are G band at ~1580 cm^{-1} and 2D band

(sometimes G') at ~2700 cm^{-1}, respectively. The G band originates from the tangential in-plane stretching vibrations of the sp^2 carbon atoms within the graphene sheets [43]; whereas, the 2D band is caused by double resonance transition that produces two phonons with opposite momentum [44]. The most significant Raman feature for sp^3 defects is the D band at ~1350 cm^{-1}. Therefore, the D band is often used as a measurement of structural disorder arising from any defects in the sp^2 carbon lattice [43]. The well-known Tuinstra-Koenig (T-K) relation $I_D/I_G = C(\lambda)/L_\alpha$ (L_α is the crystallite size of sp^2 clusters) utilises the intensity ratio of D and G bands as an indicator to determine the in-plane crystallite size [45]. The Raman spectra of CNTs and two other oxidised CNT samples, viz. oCNHs and GONRs, are presented in Figure 36b.
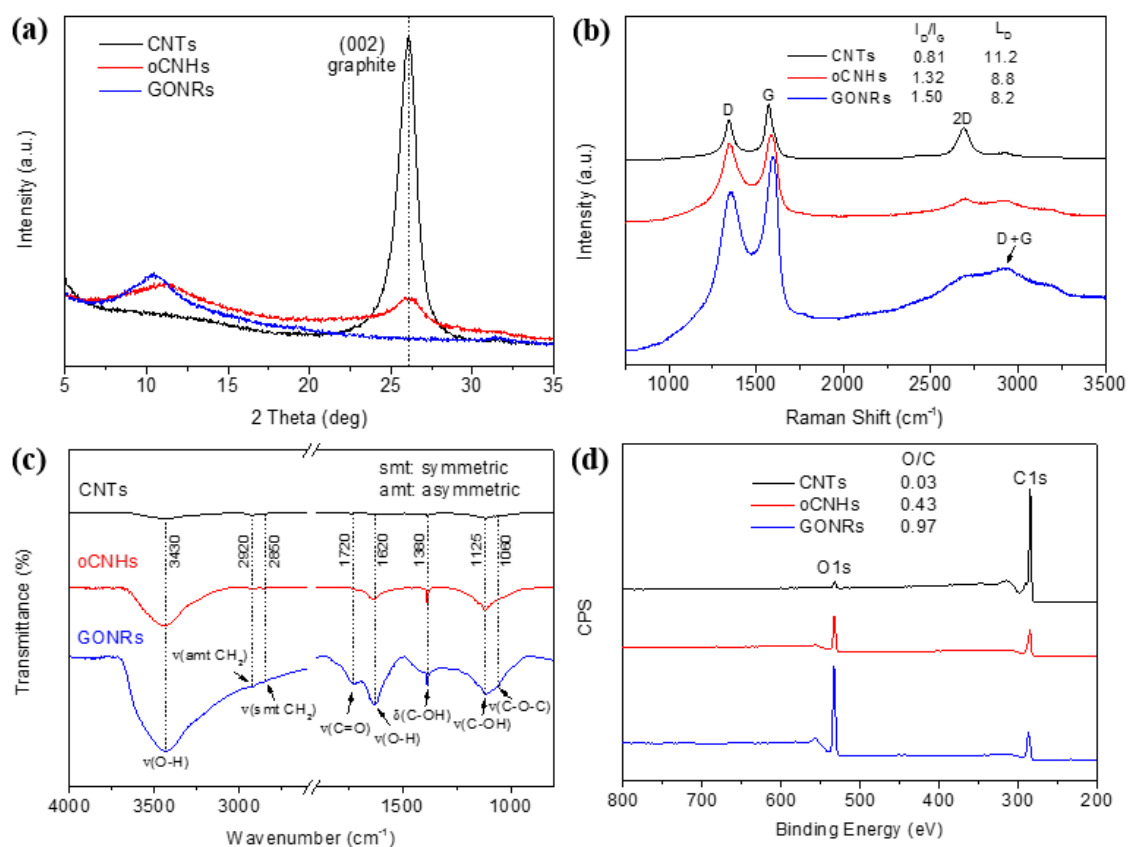

Figure 36. (a) XRD profiles of CNTs, oCNHs and GONRs; (b) Raman spectra of CNTs, oCNHs and GONRs; (c) FTIR spectra of CNTs, oCNHs and GONRs and (d) XPS survey spectra of CNTs, oCNHs and GONRs.

As shown in Figure 36b, both G band and D band are obvious for the raw CNT sample, although the G band is slightly sharper than the D band. The G band is derived from the graphite-like in-plane mode, while the D band is attributed to the intrinsic impurities (defects) of the nanotubes. The increase in oxidation of CNTs destroyed the symmetry of the C-C structure, which caused the change in the bonding mode of the carbon atoms. In addition to the change in D and G bands, the 2D band, also known as the second order overtone of the D band, is found becoming less visible with increasing $KMnO_4$:CNTs ratio. This suggests a reduced continuous sp^2 domain size due to the occupation of doped oxygen groups on the graphitic basal planes [46]. A defect-activated peak called D+G is also readily visible near 2950 cm^{-1} in the spectra of oCNH and GONR samples. This is a signal for the presence of unzipped/scissored nanotubes, attributed to the chemical doping of oxygen functional groups [46].

In order to determine the degree of disorder in the raw and oxidized samples, the integrative intensity ratio I_D/I_G were calculated. As presented in Figure 36b, the integrative I_D/I_G intensity ratio increases with increasing degree of oxidation, which is expected as oxidation would induce new sp^3 binding of C-O and C=O that could contribute to the D band intensity. Moreover, an established relation in the form $I_D/I_G = 102/L_D^2$ (L_D is the average distance between defects) was also adapted to show the evolution of defects in response to oxidation [47]. The decreased distance between defects after oxidation suggests increased defect density, which is reasonable and supports previous findings. From the increasing defect signals, it is believable that as the degree of oxidation increases, more oxygen functional groups are introduced on the graphitic basal planes.

The FTIR spectra of CNTs, oCNHs and GONRs are presented in Figure 36c. It is clear that the oxygen-containing functional groups contribute the most to the FTIR spectra. The characteristic peak near 3430 cm^{-1} is attributed to the stretching vibration of hydroxyl group of adsorbed water molecules [42, 48]. Comparison of the three spectra clearly shows that as the oxidation level increases, the peak near 3430 cm^{-1} becomes broader and stronger. The similar trend also applies to the peak at ~1620 cm^{-1}, which is assigned to the contributions from the vibrations of adsorbed water molecules [49]. The increase in intensity of these two peaks means the increased amount of water

molecules being adsorbed onto the nanosheets. This suggests a larger quantity of surface functional groups that are introduced, leading to the easy formation of hydrogen bonds between the nanotubes and the water molecules. As a result, the sample with a greater degree of oxidation should be more hydrophilic. The absorption peaks at ~2920 cm^{-1} and ~2850cm^{-1} represent the asymmetric and symmetric stretching vibrations of CH_2 [42]. These two peaks are normally used to determine the presence of reduced graphene oxides [42], and there is no obvious difference in the corresponding peaks of the two among the three samples. Other characteristic peaks that are observed from the spectra are related to the vibrations of oxygen-containing functional groups, including peaks at ~1720 (C=O carboxyl or carbonyl stretching vibration), ~1380 (O-H deformations in the C-OH groups), ~1125 (C-OH stretching vibration) and ~1060 cm^{-1} (C-O stretching vibrations in C-O-C in epoxide) [50, 51]. The existence and ever-increasing signals of these oxygen-containing groups reveal that the CNTs are oxidised gradually with the increasing level of oxidation.

Figure 36d illustrates the XPS survey spectra of CNTs, oCNHs and GONRs. The O/C atomic ratios were calculated and used to quantify the change in the oxygen content of the oxidised CNT samples. Obviously, the O/C atomic ratio shows a progressive increase as the degree of oxidation increases. This suggests that the oxygen content of the oxidised CNTs can be tuned by varying the $KMnO_4$:CNTs ratios. The changing chemical bonding of carbon with oxygen in the various samples were further confirmed by the XPS high-resolution C 1s and O 1s peaks. Figure 37a shows the high-resolution C 1s spectra of the three samples. The peak centred at 284.6 eV (C 1s A) is also known as the sp^2 peak, corresponding to the C=C bond within the graphene ring networks [42, 52]. The C 1s C peak at 286.8 eV arises from the epoxide group ($\overset{O}{\underset{C-C}{\triangle}}$) [42, 48, 52]. The C 1s D peak at ~288.2 eV (for GONRs) and ~288.9 eV (for oCNHs) correspond to the carbonyl group (C=O) and the carboxyl group (O=C-OH), respectively [42, 48, 52]. The most significant difference between the pristine CNT sample and the oxidised samples (oCNHs and GONRs) is that the C 1s spectrum of the pristine CNT only contains a single peak centred at 284.6 eV, while that of oCNHs and GONRs consist of well-defined triple peak formations. This is not surprising as the peak intensity of carbonyl and carboxyl groups are the signature of the extreme oxidation in the oxidised samples. Based on the results demonstrated by the XPS survey spectra, the pristine CNT contains a very low oxygen content, which hardly

contributes to significant C 1s C and C 1s D peaks. The comparison between oCNHs and GONRs shows that the sp^2 peak intensity becomes weaker accompanied with stronger peaks resulting from carbonyl and carboxyl groups after increasing the degree of oxidation. This is expected since the increasing degree of oxidation can further destroy the graphene sp^2 structure and lead to the formation of more oxygen-containing functional groups on the graphene basal plane or between the graphene layers. A slight shift between the C 1s D peak of oCNHs and the C 1s D peak of GONRs is observed probably due to the change of dominant oxygen-containing functional groups after the tubes were fully unzipped or opened.

The high-resolution O 1s spectra of all the three samples are collected in Figure 37b. The O 1s peaks for A, B and C correspond to carbonyl/carboxyl C=O group (at ~531.6±0.2 eV), hydroxyl O-H group (at ~533.5±0.2) in water molecules, and hydroxyl/carboxyl C-OH group (at ~532.5±0.2 eV), respectively [46, 53, 54]. These peaks suggest that there is a combination of hydroxyl, carbonyl and carboxyl oxygen-containing functional groups on the carbon surface.
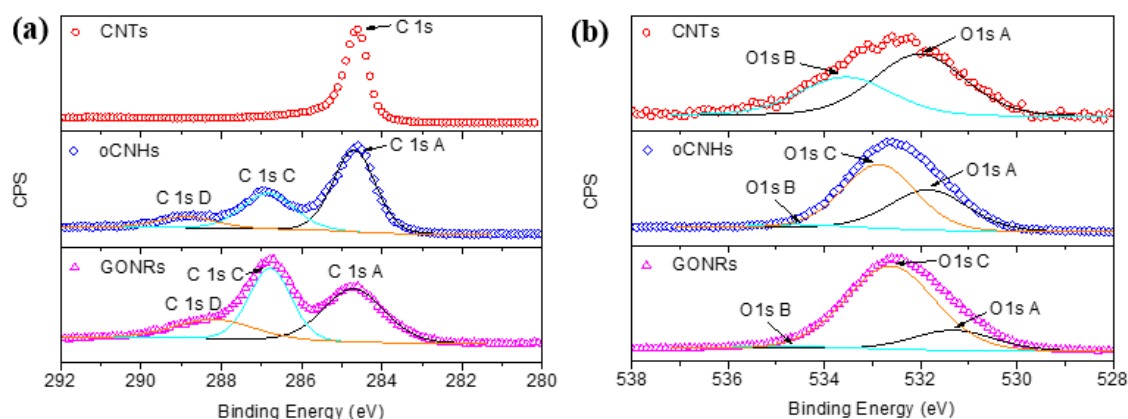
Figure 37. XPS high-resolution of (a) C 1s spectra of CNTs, oCNHs and GONRs and (b) O 1s spectra of CNTs, oCNHs and GONRs

The amount of oxidising agent (KMnO$_4$) used in the system can determine the degree of tube opening in the CNTs and the degree of tube opening with different amounts of oxygen functionalities affects the electrical conductivity. According to the various instrumental analyses, the GONRs under a strong oxidation condition were completely

unzipped to form a ribbon-like structure, which were decorated with a larger amount of oxygen functional groups on the surface. However, the abundant oxygen groups, though they can enhance the capacitance of the supercapacitor, disrupt the sp^2 bonding network of the CNTs, resulting in an inferior electrical conductivity, which negatively affects the performance of the electrodes. Interestingly, the oCNHs that were produced by a mild oxidation degree possessed a hybrid structure, i.e. both closed tubes and unzipped tubes. The unzipped tubes enriched with the abundant oxygen-containing groups can provide electrochemical active sites for improving the capacitance of the supercapacitor as well as the closed tubes that preserve mostly the sp^2 bonding network of the CNTs can endow the material with a satisfactory electrical conductivity. Given the balance between the capacitance and the conductivity, the oCNHs were used as the electrodes to construct a solid-state supercapacitor.

5.3.2 Structural properties of integrated membranes

Figure 38a shows the stepwise of fabrication of the paper-like supercapacitors. Figure 38b provides a digital photograph illustrating the physical appearance of the oCNHs-cellulose membrane. Figure 38c shows a digital photograph illustrating the flexibility of the solid-state device as-fabricated. The SEM images of different electrode films are collected in Figure 39, demonstrating the microscopic structural properties of various film-like electrodes.

As illustrated in Figure 39, the film-like electrodes prepared by vacuum filtration exhibited high flexibility and good mechanical strength and integrity, highlighting the potential for the development of high-performance flexible all-solid-state supercapacitors. From the SEM images collected in Figure 39, the electrode films share some common features. First, CNTs are observed in all the electrodes. This is understandable as the electrodes were prepared by either pure CNTs or pure oCNHs or both. As discussed earlier, oCNHs is a hybrid material that contains both unopened and unzipped CNTs. Second, all the electrode films are highly porous. The porous structure is an important property for the electrode materials, as it creates a large surface area which is necessary for high-performance supercapacitors [55, 56]. Third, the film-like electrodes present a multiple layered structure. This is due to the gelation behaviour of graphene sheets in vacuum filtration, which facilitated the formation of

oriented conductive hydrogel film [57]. This special structure enables the electrode films to have several advantages such as enhanced mechanical strength, better flexibility and greater conductivity [57].
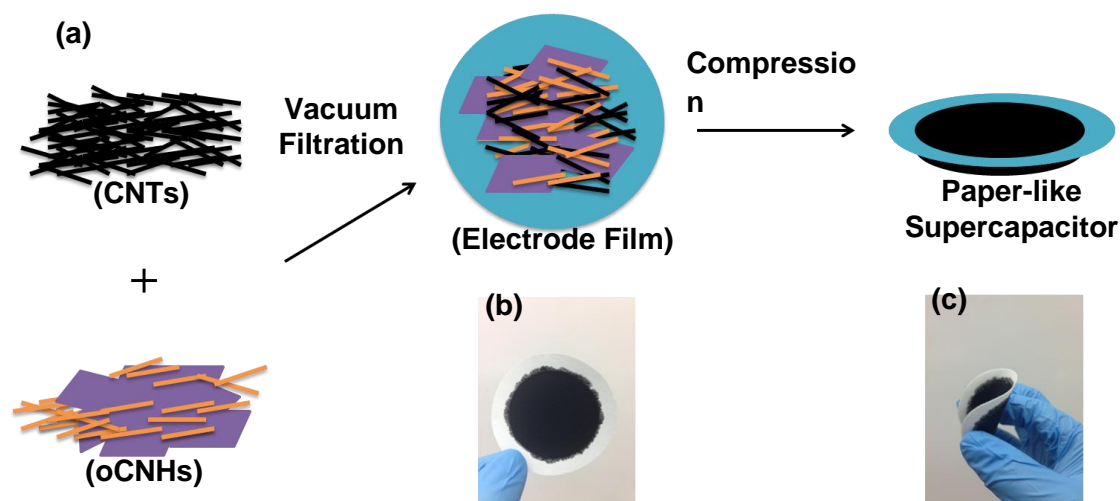
Figure 38. (a) Scheme for the fabrication of solid-state paper-like supercapacitors. The yellow rods show the oxidised CNTs and the purple sheets indicate the unzipped nanotubes. (b) A digital photograph of the oCNHs-cellulose membrane and (c) A digital photograph showing the flexibility of the solid-state supercapacitor.
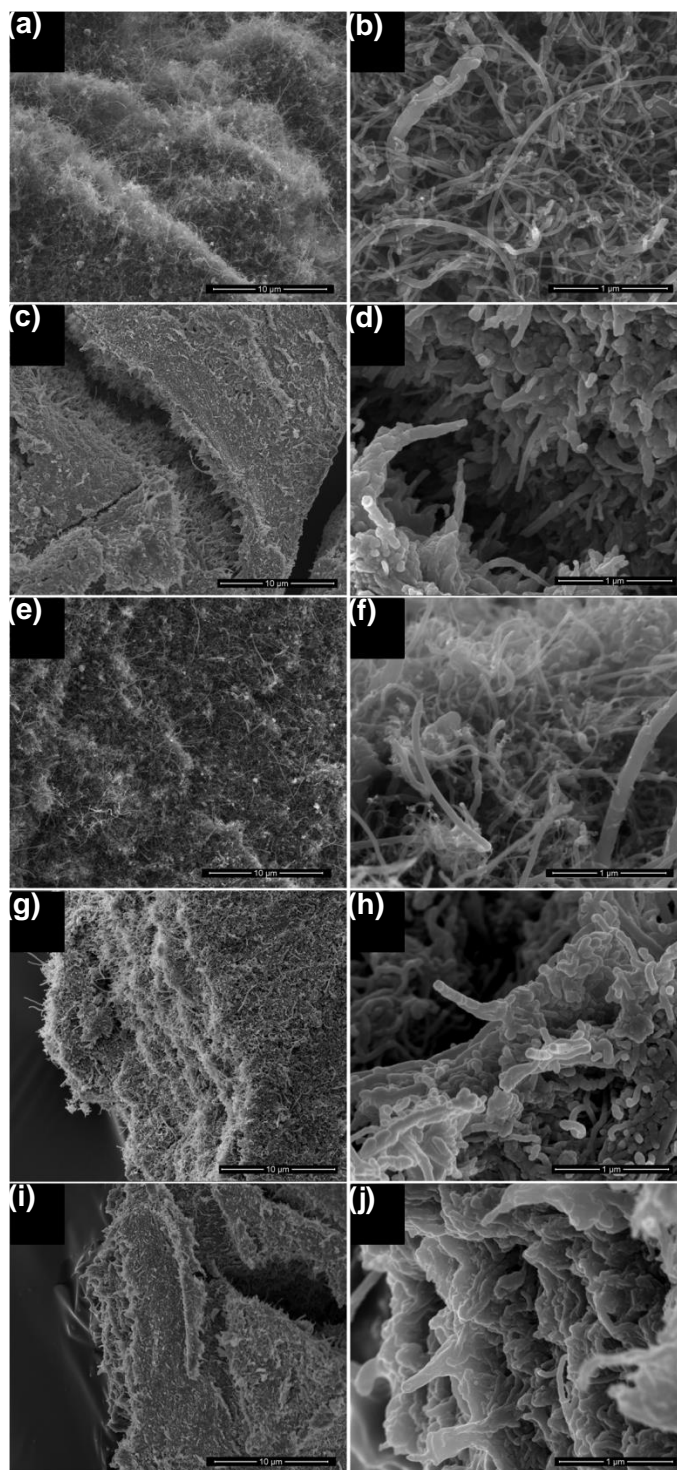
Figure 39. SEM images of (a-b) 50CNTs electrode film; (c-d) 40CNTs-10oCNHs electrode film; (e-f) 25CNTs-25oCNHs electrode film; (g-h) 10CNTs-40oCNHs electrode film and (i-j) 50CNHs electrode film.

5.3.3 Electrochemical Performance of Solid-state Supercapacitors

The CV curves of a variety of solid-state supercapacitors at a scan rate of 5 mV/s are displayed in Figure 40a. As shown in Figure 40a, all the solid-state supercapacitors present a typical capacitive behaviour with nearly rectangular CV curves at a scan rate of 5 mV/s. The areal capacitances versus scan rate of various solid-state supercapacitors are displayed in Figure 40b. Among these supercapacitors, supercapacitors based on 10CNTs-40oCNHs and 25CNTs-25oCNHs demonstrate better performance than others. From Figure 40b, it is also shown that 10CNTs-40oCNHs and 25CNTs-25oCNHs supercapacitors exhibit larger areal capacitances than other supercapacitors at all scan rates, ranging from 5 mV/s to 200 mV/s. Generally, the areal capacitances of all the supercapacitors present an inversely proportional relationship to the scan rate. Comparison of the two supercapacitors based on 10CNTs-40oCNHs and 25CNTs-25oCNHs shows that the former has a larger areal capacitance at low scan rates (<15 mV/s) yet a smaller areal capacitance at high scan rates (>15 mV/s). The mass ratio of 1:1 (25CNTs-25oCNHs) was selected as the optimum mass ratio, as the solid-state supercapacitor based on this ratio also presented excellent electrochemical performance at high scan rates. More detailed CV curves of the solid-state supercapacitor based on 25CNTs-25oCNHs at various scan rates are collected in Figure 40c. Clearly, CV curves with typical capacitive behaviour are observed.

Based on the optimum mass ratio determined, the stability of electrochemical performance of the solid-state supercapacitor based on 25CNTs-25oCNHs was studied. Figure 40d shows the CV curves of a solid-state supercapacitor based on 25CNTs-25oCNHs at 5 mV/s before and after 1000 charge-discharge cycles. It manifests that the solid-state supercapacitor based on the optimum mass ratio shows a good stability as the CV curves of the supercapacitor before and after 1000 charge-discharge cycles are almost identical.
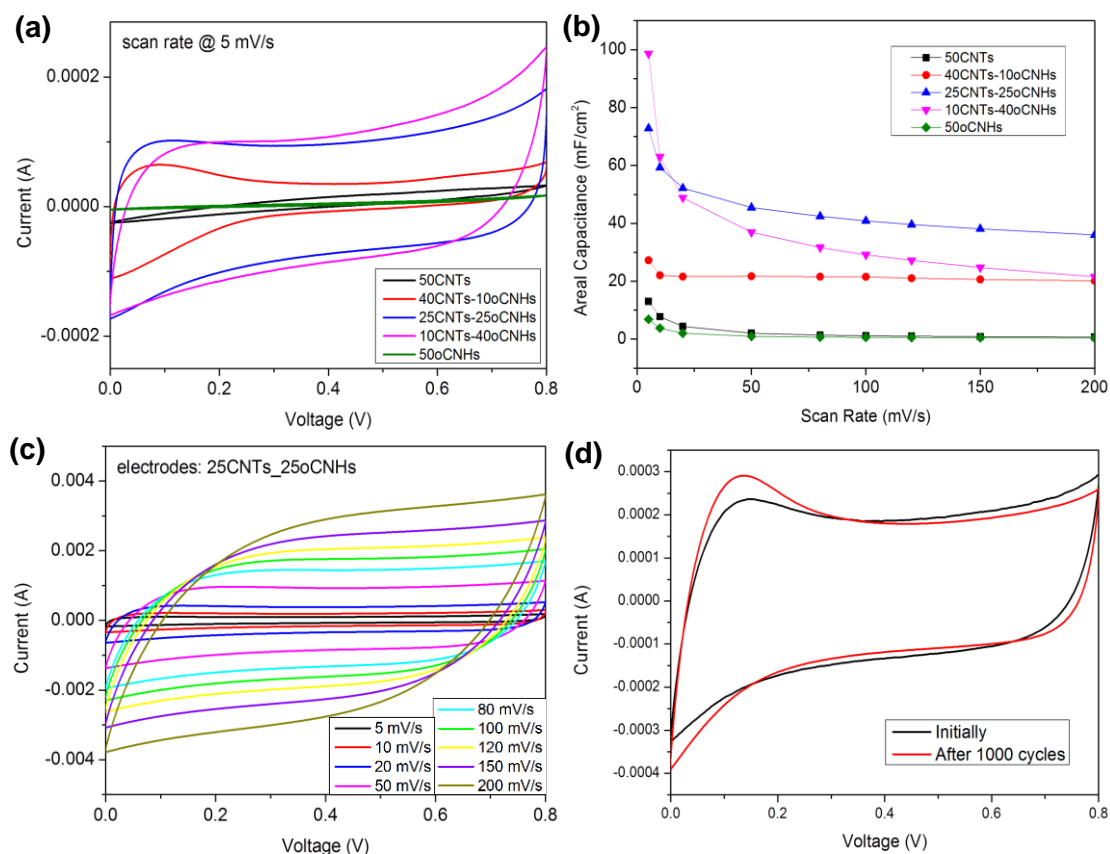
Figure 40. (a) Current versus Voltage (CV) curves of a range of solid-state supercapacitors at a scan rate of 5 mV/s; (b) Rate capabilities of a variety of solid-state supercapacitors; (c) Current versus voltage (CV) curves of a solid-state supercapacitor based on 25CNTs-25oCNHs at various scan rates, ranging from 5 mV/s to 200 mV/s; (d) Current versus voltage (CV) curves of a solid-state supercapacitor based on 25CNTs-25oCNHs at 5 mV/s before and after 1000 charge-discharge cycles

5.4 Summary

The structure of oxidised CNT products can be controlled by tuning the $KMnO_4$:CNTs mass ratios through an improved Hummer's oxidation method. A mass ratio of 3:1 derives oCNHs with both tubular and exfoliated structures. This special hybrid structure gives oCNHs a balanced property for electrochemical applications, which marks it as a promising material for high-performance flexible solid-state supercapacitor. The electrodes based on a 1:1 mass ratio of CNTs to oCNHs shows the best electrochemical performance, owing to its balanced conductivity and number of useful active sites. The solid-state supercapacitor based on optimum mass ratio shows a

high areal capacitance of ~75 mF/cm^2 at a low scan rate (5 mV/s) and an excellent stability by retaining its electrochemical performance after 1000 charge-discharge cycles.

5.5 References

[1]   Administration EI. International Energy Outlook 2013 With Projections to 2040: Government Printing Office; 2013.

[2]   Goodenough JB. Energy storage materials: A perspective. Energy Storage Materials. 2015;1:158-61.

[3]   Miller JR, Simon P. Electrochemical capacitors for energy management. Science Magazine. 2008;321(5889):651-2.

[4]   Burke A. Ultracapacitors: why, how, and where is the technology. Journal of power sources. 2000;91(1):37-50.

[5]   Pandolfo A, Hollenkamp A. Carbon properties and their role in supercapacitors. Journal of power sources. 2006;157(1):11-27.

[6]   Nathan A, Ahnood A, Cole MT, Lee S, Suzuki Y, Hiralal P, et al. Flexible electronics: The next ubiquitous platform. Proceedings of the IEEE. 2012;100(Special Centennial Issue):1486-517.

[7]   LeMieux MC, Bao Z. Flexible electronics: stretching our imagination. nature nanotechnology. 2008;3(10):585-6.

[8]   Lu X, Xia Y. Electronic materials: Buckling down for flexible electronics. Nature nanotechnology. 2006;1(3):163-4.

[9]   Park S, Wang G, Cho B, Kim Y, Song S, Ji Y, et al. Flexible molecular-scale electronic devices. Nature nanotechnology. 2012;7(7):438-42.

[10]   Kaempgen M, Chan CK, Ma J, Cui Y, Gruner G. Printable thin film supercapacitors using single-walled carbon nanotubes. Nano letters. 2009;9(5):1872-6.

[11]   Kang YJ, Chun S-J, Lee S-S, Kim B-Y, Kim JH, Chung H, et al. All-solid-state flexible supercapacitors fabricated with bacterial nanocellulose papers, carbon nanotubes, and triblock-copolymer ion gels. ACS nano. 2012;6(7):6400-6.

[12]   Niu Z, Dong H, Zhu B, Li J, Hng HH, Zhou W, et al. Highly Stretchable, Integrated Supercapacitors Based on Single‐Walled Carbon Nanotube Films with Continuous Reticulate Architecture. Advanced Materials. 2013;25(7):1058-64.

[13]   Yang Z, Deng J, Chen X, Ren J, Peng H. A Highly Stretchable, Fiber‐Shaped Supercapacitor. Angewandte Chemie International Edition. 2013;52(50):13453-7.

[14]   Chen T, Peng H, Durstock M, Dai L. High-performance transparent and stretchable all-solid supercapacitors based on highly aligned carbon nanotube sheets. Scientific reports. 2014;4.

[15]   El-Kady MF, Strong V, Dubin S, Kaner RB. Laser scribing of high-performance and flexible graphene-based electrochemical capacitors. Science. 2012;335(6074):1326-30.

[16]   Xu Y, Lin Z, Huang X, Liu Y, Huang Y, Duan X. Flexible solid-state supercapacitors based on three-dimensional graphene hydrogel films. ACS nano. 2013;7(5):4042-9.

[17]   Zhao Y, Liu J, Hu Y, Cheng H, Hu C, Jiang C, et al. Highly Compression‐Tolerant Supercapacitor Based on Polypyrrole‐mediated Graphene Foam Electrodes. Advanced Materials. 2013;25(4):591-5.

[18]   Yoo JJ, Balakrishnan K, Huang J, Meunier V, Sumpter BG, Srivastava A, et al. Ultrathin planar graphene supercapacitors. Nano letters. 2011;11(4):1423-7.

[19]   Wu ZS, Parvez K, Feng X, Müllen K. Graphene-based in-plane micro-supercapacitors with high power and energy densities. Nature communications. 2013;4.

[20]   El-Kady MF, Kaner RB. Scalable fabrication of high-power graphene micro-supercapacitors for flexible and on-chip energy storage. Nature communications. 2013;4:1475.

[21]   Chen T, Xue Y, Roy AK, Dai L. Transparent and Stretchable High-Performance Supercapacitors Based on Wrinkled Graphene Electrodes. ACS nano. 2013;8(1):1039-46.

[22]   Weng Z, Su Y, Wang DW, Li F, Du J, Cheng HM. Graphene–cellulose paper flexible supercapacitors. Advanced Energy Materials. 2011;1(5):917-22.

[23]   Ren W, Cheng HM. The global growth of graphene. Nature nanotechnology. 2014;9(10):726-30.

[24]   Chen Y-C, Hsu Y-K, Lin Y-G, Lin Y-K, Horng Y-Y, Chen L-C, et al. Highly flexible supercapacitors with manganese oxide nanosheet/carbon cloth electrode. Electrochimica Acta. 2011;56(20):7124-30.

[25]   Xu D, Xu Q, Wang K, Chen J, Chen Z. Fabrication of Free-Standing Hierarchical Carbon Nanofiber/Graphene Oxide/Polyaniline Films for Supercapacitors. ACS applied materials & interfaces. 2013;6(1):200-9.

[26]   Meng C, Liu C, Chen L, Hu C, Fan S. Highly flexible and all-solid-state paperlike polymer supercapacitors. Nano letters. 2010;10(10):4025-31.

[27]   Zhang N, Luan P, Zhou W, Zhang Q, Cai L, Zhang X, et al. Highly stretchable pseudocapacitors based on buckled reticulate hybrid electrodes. Nano Research. 2014:1-11.

[28]   Wang K, Zhang X, Li C, Zhang H, Sun X, Xu N, et al. Flexible Solid-State Supercapacitors Based on Conducting Polymer Hydrogel with Enhanced Electrochemical Performance. Journal of Materials Chemistry A. 2014.

[29]   Wang Z-L, He X-J, Ye S-H, Tong Y-X, Li G-R. Design of Polypyrrole/Polyaniline Double-Walled Nanotube Arrays for Electrochemical Energy Storage. ACS applied materials & interfaces. 2013;6(1):642-7.

[30]   Wang D-W, Li F, Zhao J, Ren W, Chen Z-G, Tan J, et al. Fabrication of graphene/polyaniline composite paper via in situ anodic electropolymerization for high-performance flexible electrode. Acs Nano. 2009;3(7):1745-52.

[31]   Dubal DP, Gund GS, Holze R, Jadhav HS, Lokhande CD, Park C-J. Solution-based binder-free synthetic approach of RuO_2 thin films for all solid state supercapacitors. Electrochimica Acta. 2013;103:103-9.

[32]   Yang P, Li Y, Lin Z, Ding Y, Yue S, Wong CP, et al. Worm-like amorphous MnO 2 nanowires grown on textiles for high-performance flexible supercapacitors. Journal of Materials Chemistry A. 2014;2(3):595-9.

[33]   Lee M, Wee BH, Hong JD. High Performance Flexible Supercapacitor Electrodes Composed of Ultralarge Graphene Sheets and Vanadium Dioxide. Advanced Energy Materials. 2015;5(7).

[34]   Dai L, Chang DW, Baek JB, Lu W. Carbon nanomaterials for advanced energy conversion and storage. Small. 2012;8(8):1130-66.

[35]   Inagaki M, Konno H, Tanaike O. Carbon materials for electrochemical capacitors. Journal of Power Sources. 2010;195(24):7880-903.

[36]   Wu Z-S, Yang S, Zhang L, Wagner JB, Feng X, Müllen K. Binder-free activated graphene compact films for all-solid-state micro-supercapacitors with high areal and volumetric capacitances. Energy Storage Materials. 2015;1:119-26.

[37]   Wu ZS, Feng X, Cheng HM. Recent advances in graphene-based planar micro-supercapacitors for on-chip energy storage. National Science Review. 2013;1(2):277-92.

[38]   Candelaria SL, Cao G. Increased working voltage of hexamine-coated porous carbon for supercapacitors. Science Bulletin. 2015;60(18):1587-97.

[39]   Xiao X, Zhang C, Lin S, Huang L, Hu Z, Cheng Y, et al. Intercalation of cations into partially reduced molybdenum oxide for high-rate pseudocapacitors. Energy Storage Materials. 2015;1:1-8.

[40]   Jeon I-Y, Shin Y-R, Sohn G-J, Choi H-J, Bae S-Y, Mahmood J, et al. Edge-carboxylated graphene nanosheets via ball milling. Proceedings of the National Academy of Sciences. 2012;109(15):5588-93.

[41]   Jeon I-Y, Choi H-J, Jung S-M, Seo J-M, Kim M-J, Dai L, et al. Large-scale production of edge-selectively functionalized graphene nanoplatelets via ball milling and their use as metal-free electrocatalysts for oxygen reduction reaction. Journal of the American Chemical Society. 2012;135(4):1386-93.

[42]   Jeon I-Y, Choi H-J, Ju MJ, Choi IT, Lim K, Ko J, et al. Direct nitrogen fixation at the edges of graphene nanoplatelets as efficient electrocatalysts for energy conversion. Scientific reports. 2013;3.

[43]   Jeon IY, Zhang S, Zhang L, Choi HJ, Seo JM, Xia Z, et al. Edge‐Selectively Sulfurized Graphene Nanoplatelets as Efficient Metal‐Free Electrocatalysts for Oxygen Reduction Reaction: The Electron Spin Effect. Advanced Materials. 2013;25(42):6138-45.

[44]   Kosynkin DV, Higginbotham AL, Sinitskii A, Lomeda JR, Dimiev A, Price BK, et al. Longitudinal unzipping of carbon nanotubes to form graphene nanoribbons. Nature. 2009;458(7240):872-6.

[45]   Alejandro. Multiwall Carbon Nanotube. 2014 [cited; Available from: https://3dwarehouse.sketchup.com/model.html?id=51e7ec1b4277a53f2f5821b388a2ed 60

[46]   Li H, Yang C, Liu F. Novel method for determining stacking disorder degree in hexagonal graphite by X-ray diffraction. Science in China Series B: Chemistry. 2009;52(2):174-80.

[47]   Acik M, Mattevi C, Gong C, Lee G, Cho K, Chhowalla M, et al. The role of intercalated water in multilayered graphene oxide. ACS nano. 2010;4(10):5861-8.

[48]   Wang D-W, Wu K-H, Gentle IR, Lu GQM. Anodic chlorine/nitrogen co-doping of reduced graphene oxide films at room temperature. Carbon. 2012;50(9):3333-41.

[49]   Osswald S, Havel M, Gogotsi Y. Monitoring oxidation of multiwalled carbon nanotubes by Raman spectroscopy. Journal of Raman Spectroscopy. 2007;38(6):728-36.

[50]   Shahriary L, Athawale AA. Graphene oxide synthesized by using modified hummers approach. Int J Renew Energy and Env Engg. 2014;2(1):58-63.

[51]   Tuinstra F, Koenig JL. Raman spectrum of graphite. The Journal of Chemical Physics. 1970;53(3):1126-30.

[52]   Wu K-H, Wang D-W, Gentle IR. Revisiting oxygen reduction reaction on oxidized and unzipped carbon nanotubes. Carbon. 2015;81:295-304.

[53]   Lucchese MM, Stavale F, Ferreira EM, Vilani C, Moutinho M, Capaz RB, et al. Quantifying ion-induced defects and Raman relaxation length in graphene. Carbon. 2010;48(5):1592-7.

[54]   Wang D-W, Du A, Taran E, Lu GQM, Gentle IR. A water-dielectric capacitor using hydrated graphene oxide film. Journal of Materials Chemistry. 2012;22(39):21085-91.

[55]   Xu Y, Bai H, Lu G, Li C, Shi G. Flexible graphene films via the filtration of water-soluble noncovalent functionalized graphene sheets. Journal of the American Chemical Society. 2008;130(18):5856-7.

[56]   Wu N, She X, Yang D, Wu X, Su F, Chen Y. Synthesis of network reduced graphene oxide in polystyrene matrix by a two-step reduction method for superior conductivity of the composite. Journal of Materials Chemistry. 2012;22(33):17254-61.

[57]   Yang T, Liu L-h, Liu J-w, Chen M-L, Wang J-H. Cyanobacterium metallothionein decorated graphene oxide nanosheets for highly selective adsorption of ultra-trace cadmium. Journal of Materials Chemistry. 2012;22(41):21909-16.

[58]   Wang D-W, Sun C, Zhou G, Li F, Wen L, Donose BC, et al. The examination of graphene oxide for rechargeable lithium storage as a novel cathode material. Journal of Materials Chemistry A. 2013;1(11):3607-12.

[59]   Akhavan O. The effect of heat treatment on formation of graphene thin films from graphene oxide nanosheets. Carbon. 2010;48(2):509-19.

[60]   Yang D, Velamakanni A, Bozoklu G, Park S, Stoller M, Piner RD, et al. Chemical analysis of graphene oxide films after heat and chemical treatments by X-ray photoelectron and Micro-Raman spectroscopy. Carbon. 2009;47(1):145-52.

[61]   Chen T, Dai L. Carbon nanomaterials for high-performance supercapacitors. Materials Today. 2013;16(7):272-80.

[62]   Frackowiak E, Beguin F. Carbon materials for the electrochemical storage of energy in capacitors. Carbon. 2001;39(6):937-50.

[63]   Yang X, Qiu L, Cheng C, Wu Y, Ma ZF, Li D. Ordered Gelation of Chemically Converted Graphene for Next‐Generation Electroconductive Hydrogel Films. Angewandte Chemie International Edition. 2011;50(32):7325-8.

Chapter 6 Conclusion and Recommendations

6.1 Conclusion

Graphene oxide (GO), a monolayer of graphite oxide, is an intermediate during the synthesis of graphene by a solution chemistry method starting from graphite. The graphene-based lattice and existence of abundant oxygen-containing functional groups (mainly epoxy and hydroxyl groups) enable GO various fascinating properties. Furthermore, it has been widely demonstrated that surface functional groups containing oxygen, nitrogen or phosphorus can considerably enhance the total capacitance of supercapacitors through additional faradaic reactions called pseudo-capacitance effects, as well as improving the wettability of porous carbon with electrolytes. Thus GO should be a good choice for the electrode material for supercapacitors, due to its high surface area and enriched oxygen-containing functional groups.

GO has been successfully used as an electrode material to construct two types of supercapacitors in this project. As the degree of tube opening in the CNTs can be controlled by adjusting the amount of oxidizing agent introduced into the system, GO with different amounts of oxygen functionalities (accompanying with different extents of the nanotube opening) are obtained from oxidation of CNTs at different degrees of oxidation ($KMnO_4$:CNTs mass ratio=1:1, 3:1, 5:1 and 10:1). According to the three-electrode potentiostat tests, the optimal oCNT sample was obtained with $KMnO_4$:CNTs ratio of 1:1, which are characterised by the abundant oxygen-containing groups at the surface and the intact graphitic inner tubes that can maintain the electrical conductivity. The oxygen functional groups present on the oCNTs are advantageous, as they provide a large additional pseudo-capacitance as well as improved wettability, giving the oCNTs a higher capacitance. Moreover, 3:1 oCNHs (oxidised carbon nanohybrids), which possessed both tubular (unopened CNTs) and exfoliated (unzipped or scissored) structures, can be used to develop a high-performance flexible all-solid-state supercapacitor.

An metal ion capacitor comprising of a zinc anode, a 1:1 oCNTs cathode and a zinc sulphate electrolyte has been successfully assembled. Since the shuttling cation is Zn^{2+},

this typical metal ion capacitor is named as zinc-ion capacitor (ZIC). The low cost zinc metal and the nontoxic, noncorrosive $ZnSO_4$ solution enable the ZIC to be a cost-effective and environmentally friendly energy storage system. The ZIC integrates the divalent zinc stripping/plating chemistry with the surface-enabled pseudo-capacitive cation adsorption/desorption on oCNTs. The surface chemistry and crystallographic structure of oCNTs were extensively characterized by combining XPS, FTIR, Raman and XRD measurements. The function of the surface oxygen groups for surface cation storage was elucidated by a series of electrochemical measurements and the ZIC showed a better performance than the ZIC with an un-oxidized CNT cathode. Due to the electrochemical adsorption/desorption of Zn^{2+} ions on the oxygen-containing groups of the oCNT cathode, the pseudocapacitive behaviour observed in this ZIC delivered a specific capacitance of 20 mF/cm^2 at a scan rate of 10 mV/s[1].

Additionally, the potential of an innovative material called oCNHs for its application in high-performance flexible supercapacitors are demonstrated in this work. oCNHs are prepared by an improved Hummer's oxidation method with a 3:1 $KMnO_4$:CNTs mass ratio. The prepared oCNHs show both tubular and exfoliated structures. This special dual structure gives oCNHs a balance property of high conductivity with large number of useful active sites, which are necessary for high-performance supercapacitors. The solid-state supercapacitor based on its electrodes with a 1:1 mass ratio of CNTs to oCNHs shows a high areal capacitance of ~75 mF/cm^2 at a low scan rate (5 mV/s) and excellent stability by retaining its electrochemical performance after 1000 charge-discharge cycles.

6.2 Recommendations

Driven by the need to maintain the power capability as well as enhance the capacitance and energy density performance,[1] hybrid electrochemical capacitors with a different asymmetric configuration have been developed in recent years [2]. The hybrid electrochemical capcitors are generally composed of a battery-type Faradaic anode as energy source and a capacitor-type cathode as power source.[3] The particular example is the metal-ion capacitor. However, the lithium-ion or sodium-ion capacitors suffer from the high cost or/and the safety issue. Consequently, there is an urgent need to search for more favourable alternative metal-ion capacitor. In this project, a safe, cost-effective and eco-friendly zinc ion capacitor was constructed by using a CNT-based pseudo-capacitive cathode and a zinc anode. In fact, there are still many other metals that can probably be used in the metal-ion capacitors. For example, aluminium as the most abundant metal and the third most abundant element in the earth's crust has been used to construct a novel Al-ion battery.[4] The battery used V_2O_5 as the cathode against an aluminium metal anode in an ionic liquid-based electrolyte, which displayed promising electrochemical features with stable cycling behaviour. Magnesium, being divalent and denser, is theoretically capable of delivering a high volumetric energy-density (3833 mAh/cm^3) and therefore Mg-ion batteries are garnering research interests as an alternative to lithium based battery systems.[5] Interestingly, a potassium-ion battery using a low-strain nickel hexacyanoferrate (NiHCF) electrode material, which showed stable cycling over many thousands of cycles with a high rate capability, has been recently reported.[6] These different metals as the anodes exhibit the superior performances in batteries. Therefore, they have a great potential to be applied as the anode materials for fabrication of the metal-ion capacitors potentially, provided that an appropriate cathode material is used.

As intercalation capacitance is emerging as a promising approach to increasing energy density of electrochemical capacitor, it has been found that in addition to GO-based nanocomposites, layered transition metal dichalcogenides (TMDs), such as MoS_2 and WS_2, exhibit excellent supercapacitor properties and the interlayer spacing of TMDs provides a convenient environment for the accommodation of a variety of guest species, for example Li$^+$ ions. Thus, the suitable TMD-based composite materials can be developed to construct the electrochemical capacitors and their electrochemistry of the intercalation charge storage can be studied.

6.3 References

[1]   S.-K. Chang, Z. Zainal, K.-B. Tan, N. A. Yusof, W. M. D. Wan Yusoff, and S. R. S. Prabaharan, "Recent development in spinel cobaltites for supercapacitor application," *Ceram. Int.*, vol. 41, no. 1, pp. 1–14, 2015.

[2]   S. Faraji and F. Nasir, "The development supercapacitor from activated carbon by electroless plating — A review," *Renew. Sustain. Energy Rev.*, vol. 42, pp. 823–834, 2015.

[3]   S. Faraji and F. N. Ani, "Microwave-assisted synthesis of metal oxide/hydroxide composite electrodes for high power supercapacitors - A review," *J. Power Sources*, vol. 263, pp. 338–360, 2014.

[4]   N. Jayaprakash, S. K. Das, and L. a. Archer, "The rechargeable aluminum-ion battery," *Chem. Commun.*, vol. 47, no. 47, p. 12610, 2011.

[5]   N. Singh, T. S. Arthur, C. Ling, M. Matsui, and F. Mizuno, "A high energy-density tin anode for rechargeable magnesium-ion batteries.," *Chem. Commun. (Camb).*, vol. 49, no. 2, pp. 149–51, 2013.

[6]   C. D. Wessells, S. V. Peddada, R. a. Huggins, and Y. Cui, "Nickel hexacyanoferrate nanoparticle electrodes for aqueous sodium and potassium ion batteries," *Nano Lett.*, vol. 11, no. 12, pp. 5421–5425, 2011.